Fabrication and Characterization of Carbon Based Nanostructures

PhD Thesis

By

Aqsa Arshad

(Registration Number: 19-FBAS/PhDPhy/F-12)

Supervisor: Dr. Javed Iqbal Saggu (QAU, PK)

Department of Physics

Faculty of Basic and Applied Sciences

International Islamic University, Islamabad, Pakistan

2018

Fabrication and Characterization of Carbon Based Nanostructures

PhD Thesis

By

Aqsa Arshad

(Registration Number: 19-FBAS/PhDPhy/F-12)

INTERNATIONAL ISLAMIC UNIVERSITY
ISLAMABAD

Supervisor: **Dr. Javed Iqbal Saggu** (QAU, PK)

HEC sponsored IRSIP visit was supervised by

Dr. Ian Terry (Durham University, UK)

2018

Certificate

This is to certify that the work contained in this thesis entitled: **“Fabrication and Characterization of Carbon Based Nanostructures”** was carried out by **Aqsa Arshad** under my supervision. Most of the lab work was completed in Laboratory of Nanoscience and Technology (LNT), IIU; unless mentioned otherwise. The scholar also worked for six months in Department of Physics, Durham University, UK. **It is also certified that Abstract and Chapter 4 – 7 of this thesis are based on publications of Aqsa Arshad**. Her contribution was major in these experiments and articles. In my opinion, this is fully adequate in scope and quality for the thesis of PhD Physics.

Supervisor

Dr. Javed Iqbal Saggu

Associate Professor (Tenured)

Department of Physics

Quaid I Azam University, Islamabad, Pakistan

Fabrication and Characterization of Carbon Based Nanostructures

By

Aqsa Arshad

(Registration Number: 19-FBAS/PhDPhy/F-12)

A thesis submitted to

Department of Physics

for the partial fulfilment of the requirement, for the award of the degree of

Doctor of Philosophy in Physics

Signature ……………………………………………………………….

(Chairperson, Department of Physics)

Signature………………………………………………………………...

(Dean, FBAS, IIU, Islamabad)

International Islamic University, Islamabad

Faculty of Basic and Applied Sciences (FBAS)

Department of Physics

Dated:

Final Approval

This is to certify that the work in this PhD dissertation titled **“Fabrication and Characterization of Carbon based Nanostructures”** has been carried out by **Ms. Aqsa Arshad** (Registration No. 19-FBAS/PhDPhy/F12) and completed in Laboratory of Nanoscience and Nanotechnology, Department of Physics, Faculty of Basic and Applied Sciences, International Islamic University, Islamabad, Pakistan, is of sufficient standard in scope and quality for the award of degree of **PhD** in **Physics**.

Committee

External Examiner 1

Dr. Iftikhar H. Gul ____________________________
Associate Professor, SCME,

NUST, Islamabad

External Examiner 2

Dr. Arshad Mahmood Janjua ____________________________

Deputy Chief Scientist

NILOP, Islamabad.

Internal Examiner

Dr. Naeem Ahmad ____________________________

Assistant Professor, Department of Physics

International Islamic University

Supervisor

Dr. Javed Iqbal Saggu ____________________________

Associate Professor, Department of Physics

Quaid-i-Azam University

Declaration of Originality

I hereby declare that this thesis "**Fabrication and Characterization of Carbon Based Nanostructures***"* neither as a part nor as whole, has been copied out from any source. It is further declared that the research work presented in this dissertation has not been submitted for any other degree or qualification to any other university. **It is also declared that Chapter 4 to Chapter 7 of this thesis are based on my own research papers that I published in international journals**. If any part of this work is proved to be copied from any source, I (Aqsa Arshad) shall be legally responsible for punishment under the plagiarism rules of Higher Education Commission (HEC), Pakistan. **The plagiarism test has been carried out using Turnitin via ID: 967 756638. The similarity index is 7% and it lies in permissible range set by Higher Education Commission (HEC) Pakistan**.

Aqsa Arshad

19-FBAS/PhDPhy/F12

Acknowledgements

I am greatly thankful to my research supervisor, Dr. Javed Iqbal for supervising my research work and facilitating experiments. I would like to thank my foreign supervisor Dr. Ian Terry (Durham University) for his support and guidance. I also thank Ex. Dean (FBAS) Dr. Muhammad Sher, Dean (FBAS) Dr. Muhammad Arshad Zia, and Chairperson Department of Physics, Dr. Shaista Shahzada for the necessary support.

I extend gratitude to Dr. Mahavir Sharma for his insightful comments on my manuscripts, and tremendous support. I also extend thanks to Dr. Arshad Saleem Bhatti, Dr. Ishaq Ahmad, Dr. Muhammad Siddiq, Dr. Muhammad Ismail, Dr. Rizwan Ahmed and Mr. Qaisar Mansoor for facilitating experiments. I express my thanks to Dr. M. R. C Hunt, Dr. B. G. Mendis, and Dr. D. Halliday for the useful discussions. I am also thankful to Dr. Khushbakht Akram, Ms. Madiha Sabeen, Ms. Uzma Nosheen and Mr. Muhammad Saqib for providing technical support. I acknowledge Dr. Wilayat, Mr. Tahir, Mr. Basharat, Dr. Muhammad Ajmal, and Dr. Tariq Jan for their technical advises. I am also thankful to Dr. Naeem Ahmad, Dr. Syed Salman, and Dr. Kashif Nadeem for the academic support during my PhD. Special acknowledgement goes to my lab mates Mr. Muhammad Umair Ali, Mr. Waqar Amin, and my student Ms. Sadia Janjua for their help in lab work.

I can’t forget to thank my friends Mrs. Riffat Malik, Mrs. Noseeqa Zulqarnain, Ms. Anam Afzal, Ms. Robina Khan Niazi, Dr. Siddiqua Mazhar, Ms. Ala Bahaldin, Mrs. Taghreed Alsulami, Mrs. Mudassara Kanwal, and Ms. Ayesha Rafique whose support made the things lot easier. I also thank Ms. Chenxi for her cherished company.

I extend heartiest gratitude to my beloved parents, my brothers Muhammad Zulqurnain, Muhammad Adeel, Waleed, Zarbab, Shahid and sisters Samia and Maham for their tremendous support. You all were the pillars of my strength during this long journey of PhD. I wouldn’t make it without your understanding.

Experimental work always demands the help of many people. I want to say thanks to all those who helped me in one way or the other, and I forgot to mention them here.

Dedicated to

All honest researchers…

List of Publications

This thesis is based on following four peer reviewed publications in international journals.

1. **Aqsa Arshad,** Javed Iqbal, Qaisar Mansoor, NiO nanoflakes grafted graphene: An excellent photocatalyst and novel nanomaterial for complete pathogen control, Nanoscale, 9, 16321 (2017). (Impact Factor 7.367)
2. **Aqsa Arshad**, Javed Iqbal, M. Siddiq, Qaisar Mansoor, M. Ismail, Faisal Mehmood, M. Ajmal, Zubia Abid, Graphene nanoplatelets induced tailoring in photocatalytic activity and antibacterial characteristics of MgO/graphene nanoplatelets nanocomposites, Journal of Applied Physics, 121, 024901, (2017). (Impact Factor 2.1)
3. **Aqsa Arshad,** Javed Iqbal, Qaisar Mansoor, Ishaq Ahmed, Graphene/SiO_2 nanocomposite: The enhancement of photocatalytic and biomedical activity of SiO_2 nanoparticles by graphene, Journal of Applied Physics, 121, 244901, (2017). (Impact Factor 2.1)
4. **Aqsa Arshad,** Javed Iqbal, Ishaq Ahmad, M. Israr, Graphene/Fe_3O_4 nanocomposite: interplay between photo-Fenton type reaction, and carbon purity for the removal of methyl orange, Ceramics International, 44, 2643 (2018). (Impact Factor 2.986)

Additional Publications:

5. **Aqsa Arshad,** Javed Iqbal, M Siddiq, M Umair Ali, Ahmed Ali, Hassan Shabbir, Usama Bin Nazeer, M Shahbaz Saleem, Solar light triggered catalytic performance of graphene-CuO nanocomposite for waste water treatment, Ceramics International, 43, 10654, (2017). (Impact Factor 2.986),
6. **Aqsa Arshad,** Javed Iqbal, Abid Alam, Bibi Khadija, Rani Faryal, Synthesis, characterization, enhanced dielectric and antibacterial properties of WxCu1-xO nanostructures, Ceramics International, 44, 5892, (2018). (Impact Factor 2.986)
7. **Aqsa Arshad**, Javed Iqbal, Qaisar Mansoor, Graphene/Fe_3O_4 nanocomposite: solar light driven Fenton like reaction for decontamination of water and inhibition of bacterial growth, Applied Surface Science, DOI: 10.1016/j.apsusc.2018.05.046 (Impact Factor 3.387)
8. Faisal Mehmood, Javed Iqbal, Tariq Jan, Waqqar Ahmed, Waheed Ahmed**, Aqsa Arshad,** Qaisar Mansoor, Syed Zafar Ilyas, M Ismail, Ishaq Ahmad, Effect of Sn doping on the

structural, optical, electrical and anticancer properties of WO_3 nanoplates, Ceramics International 43, 10654, (2016). (Impact Factor 2.986)

9. Tariq Jan, Javed Iqbal, Muhammad Ismail, Noor Badshah, Qaisar Mansoor**, Aqsa Arshad,** Qazi M Ahkam, Synthesis, physical properties and antibacterial activity of metal oxides nanostructures, Material Science in Semiconductor Processing, 21, 154, (2014). (Impact Factor 2.359)

10. Javed Iqbal, Tariq Jan, M Shafiq, **Aqsa Arshad**, Naeem Ahmad, Saeed Badshah, Ronghai Yu, Synthesis as well as Raman and optical properties of Cu-doped ZnO nanorods prepared at low temperature, Ceramics International, 40, 2091, (2014), (Impact Factor 2.986)

11. Javed Iqbal, Tariq Jan, Muhammad Ismail, Naeem Ahmad, Asim Arif, Mohsin Khan, M Adil**, Aqsa Arshad,** Influence of Mg doping level on morphology, optical, electrical properties and antibacterial activity of ZnO nanostructures, Ceramics International, 40, 7487, (2014). (Impact Factor 2.986)

List of Figures

List of Tables

List of Symbols and Abbreviations

C_{70}	Fullerenes
NPs	Nanoparticles
NC	Nanocomposite
CNTs	Carbon nanotubes
SWCNTs	Single wall carbon nanotubes
MWCNTs	Multi wall carbon nanotubes
DWCNTs	Double wall carbon nanotubes
BZ	Brillouin zone
2-D	2 dimensional
GO	Graphene oxide
rGO	Reduced graphene oxide
WHO	World health organization
XRD	X ray diffraction
GNPs	Graphene nanoplatelets
MO	Metal oxides
DNA	Deoxyribonucleic acid
OD	Optical density
TEOS	Tetraethyl orthosilicate
CB	Conduction band
iLO	In-plane longitudinal optical
iLA	In-plane longitudinal acoustic
iTO	Out of plane transverse optical
iTA	In plane transverse acoustic
VB	Valence band
e^{-}_{CB}	Electron in conduction band
h^{+}_{V1B}	Hole in valence band
M	Molar
UV-vis	Ultra violet visible
eV	Electron volt

TEM	Transmission electron microscope
SEM	Scanning electron microscope
SE	Secondary electrons
BSE	Backscattered electrons
CCD	Charge coupled device
•OH	Hydroxyl radical
•OOH	Hydroperoxyl radical
OH^-	Hydroxyl ion
FEG	Field emission gun
HR-TEM	High resolution transmission electron microscope
SAED	Selected area electron diffraction
VSM	Vibrating sample magnetometer
KBr	Potassium bromide
FTIR	Fourier transform infrared
Fe^{2+}	Ferrous ions
Fe^{3+}	Ferric ions
MgO	Magnesium oxide
NiO	Nickel oxide
Fe_3O_4	Magnetite
SiO_2	Silica
TiO_2	Titania
ZnO	Zinc oxide
PL	Photoluminescence
ROS	Reactive oxygen species
LB	Luria Bertani
E. coli	*Escherichia coli*
S. aureus	*Staphylococcus aureus*
P. aeruginosa	*Pseudomonas aeruginosa*
ZOI	Zone of inhibition

Abstract

The increased level of industrial pollutants in water and drug resistant pathogens are serious threat to human and aquatic life. Graphene based materials are an attractive choice due to numerous fascinating features of graphene. However, combining graphene with other nanomaterials in the form of nanocomposites give a window of opportunities to fabricate and investigate new materials. Herein, a set of four graphene based nanocomposites are presented that are combination of graphene and metal/non-metal oxides. These nanocomposites are synthesized, systematically characterized and are compared for their performance in environmental and biomedical applications.

As a start-up, synthesis, the physio-chemical characterizations, photocatalytic and antibacterial properties of MgO and graphene nanoplatelets (GNPs) nanocomposites are presented. The crystallinity, phase, morphology, chemical bonding, and vibrational modes of prepared nanomaterials are studied. The conducting nature of GNPs is tailored via photocatalysis and enhanced antibacterial activity. It is interestingly observed that the MgO/GNPs nanocomposite with optimized GNPs content shows a significant photocatalytic activity (97.23% degradation) as compared to bare MgO (43%) which makes it the potential photocatalyst for purification of industrial waste water. In addition, the effect of increased quantity of GNPs on antibacterial performance of nanocomposites against pathogenic microorganisms is researched, suggesting them toxic. MgO/GNPs 25% nanocomposite may have potential applications in waste water treatment and nanomedicine due its multifunctionality.

In the following chapter, immobilization of monodispersed silicon dioxide (SiO_2) nanoparticles on multiple graphene layers is demonstrated for intercalation of graphene nanoplatelets. The exceptional conducting nature of graphene makes it a viable candidate for enhancing the effectiveness of photocatalytic and biomedical nanomaterials. Interestingly, the addition of graphene nanoplatelets with SiO_2 nanoparticles enhances the photocatalytic efficiency from 46% to 99%. For

biomedical applications, it is found that 75% of Gram positive and 50% of Gram negative bacteria have been killed; hence, bacterial proliferation is significantly restricted. The prepared nanocomposites with a controlled amount of carbon in the form of graphene can be employed for photocatalysis based waste water remediation and biomedicine.

However, the photocatalytic and antibacterial performance obtained up to this stage of work is moderate only. An effective, fast and economic dye removal method is essential to meet the stringent economic requirements. Therefore, graphene/Fe_3O_4 nanocomposite is chosen. This nanocomposite obtained via soft chemical method is characterized for its crystallinity, morphology, microstructure, vibrational modes and magnetic properties. Graphene sheets decorated with magnetite nanoparticles are investigated for their photocatalytic response against methyl orange. The study reveals that the conducting nature of graphene, engineered bandgap and photo Fenton like reaction synergistically govern the efficient photocatalytic activity of nanocomposite. Interestingly, it is observed that methyl orange can be completely removed i.e., upto 99.24% by graphene/Fe_3O_4 nanocomposite (F_z) in 30 min only, whereas the removal efficiency is 43% for Fe_3O_4 nanoparticles, alone. The presence of graphene endows the delay in charge carriers' recombination whereas, photo Fenton like reaction stimulates the generation of reactive oxygen species. This ultimately leads to the highly enhanced photocatalytic activity and complete removal of methyl orange. The magnetically separable photocatalyst, presented in this work, offers great prospects for fast and economical decontamination of dye polluted water. The antibacterial performance is also significantly enhanced but a complete pathogen control is not achieved.

At final stage, NiO nanoflakes and graphene/NiO nanocomposite are synthesized. A study on their crystal phase analysis and morphology is presented. In addition, HR-TEM images, SAED patterns and Raman modes are also investigated. A solar light induced dye removal and bactericidal properties of nickel oxide (NiO) and GNPs nanocomposites are presented. The conducting nature of GNPs is the key factor that governs the enhanced photocatalytic and antibacterial activity. It is interestingly

found that the graphene/NiO nanocomposite shows outstanding photocatalytic activity (99% degradation) as compared to NiO (34%) alone, which makes it potential candidate for depollution of dye contaminated water. In addition, the optimized concentration of GNPs in graphene/NiO nanocomposite, renders it as an exceptional antibacterial material with 100% growth inhibition of pathogenic microorganisms (both Gram positive and Gram-negative bacteria). Therefore, graphene/NiO nanocomposite can be an innovative material to achieve complete pathogen control alongside being an economic solution for water treatment.

Table of Contents

Chapter No. 01

1. Introduction

Overview:

This chapter provides a brief introduction to carbon nanostructures and particularly includes graphene, graphene derived nanomaterials, and few ceramics nanostructures that include MgO, silica, magnetite, and NiO. It includes a description of their structure and most significant properties. Their potential applications are discussed, placing the work of this thesis into context.

1.1 Carbon Nanostructures

Three previous decades are marked with remarkable progress associated with discoveries of allotropes of carbon at nanoscale. Carbon nanostructures have been a focus of scientific interest since 1985 when Kroto *et. al.*, described in their work about C_{60}, buckminsterfullerene.[1] Following their discovery on carbon that existed in soccer ball shaped molecule, an enormous interest in nano-carbon research was observed among the scientific community. It was later followed by a few other discoveries of carbon nanostructures e.g., C_{70} (fullerene) by the same group. In later years, production of macroscopic quantities of these molecules remained a prime focus for scientists.[2] It was only in 1991, when Ijima was studying the electrodes surface used for the production of fullerenes soot, using high resolution electron microscopy, the cylindrical graphitic carbon was observed.[3] Though an un-noticed first discovery of same material was made previously by Radushkevich *et.al*, in 1952, but it was only after Ijima's work that this novel carbon nanostructure received significant attention. Cylindrical graphitic structures depending on number of graphitic layers were termed as single walled carbon nanotubes (SWNTs), double-walled carbon nanotubes (DWCNTs), and multi-walled carbon nanotubes (MWCNTs). These structures possessed ultrahigh mechanical strengths, and good electrical and thermal conductivity. Based on their outstanding properties, carbon nanotubes (CNTs) have been extensively researched in the following years.[4]

MWCNTs consist of more than two concentric graphitic cylinders spaced at 0.34 nm from each other. MWCNTs possess an outer diameter that ranges between 10 nm to 20 nm. SWCNTs are cylindrical structures composed of single graphitic layer with diameter 0.4- 2 nm. CNTs find numerous applications such as in molecular scale electronics, due to their electrical properties. CNTs possess ballistic transport of carriers over micron length scales. Their tuneable semiconducting or metallic behaviour allows their use in transistors. Some other applications are based on their high mechanical strength where CNTs show flexibility without a fracture e.g., in sporting goods.[5] Moreover, CNTs are used in flexible biomedical devices recently.[6, 7] CNTs have been used in cancer treatment applications as well, where they can be applied as nanoplatform for drug attachment.[8, 9]

1.2 Graphene

Graphene's boom started in 2004 with the isolation of single layer of carbon by a simple mechanical exfoliation method.[10] Scotch tape was used to transform graphite to monolayer graphene. Later, in 2010, discoverers, the Manchester giants won the Nobel Prize for Physics. Graphene is a perfectly two-dimensional honey comb lattice of carbon atoms with in-plane sp^2 bonding. The 2-D structure is interestingly stable at ambient conditions. The electronic properties of graphene were theoretically determined using tight binding model by P. R. Wallace in 1947.[11] It was found that graphene possesses zero bandgap. Graphene is significantly different from conventional two-dimensional electron gas systems. Here, some unusual physical properties of graphene are briefly outlined that make it different from 2-D systems. Carbon atoms are arranged in hexagonal lattice which is further composed of two interpenetrating triangular sub lattices as seen in Figure 1.1. The basis consists of two atoms A and B. The lattice vectors are given by

$$\boldsymbol{a_1} = \frac{a}{2}\left(3, \sqrt{3}\right), \qquad \boldsymbol{a_2} = \frac{a}{2}\left(3, -\sqrt{3}\right), \tag{1.1}$$

The reciprocal lattice of graphene is hexagonal lattice. The centre of 1st Brillouin zone (BZ) is labelled as Γ point, the middle point of edges of graphene's BZ is labelled as M point, whereas the corners of BZ are labelled as K and K′ points. The K and K′ points are known as Dirac points. The reciprocal lattice vectors for graphene lattice are given by

$$\boldsymbol{b_1} = \frac{2\pi}{3a}\left(1, \sqrt{3}\right), \quad \boldsymbol{b_2} = \frac{2\pi}{3a}\left(1, -\sqrt{3}\right), \tag{1.2}$$

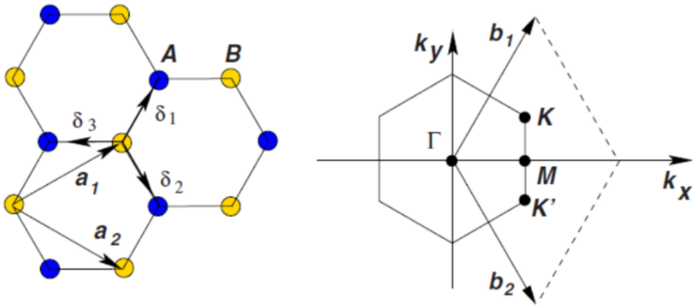

Figure 1.1 Graphene lattice in direct space (left), and reciprocal lattice of graphene (right).[12]

Electrons behave like massless Dirac fermions near the K and K′ point of this strictly 2-D system, and are essentially governed by Dirac like equation near these points. The wavefunction of electrons near the Dirac point K is a two-component spinor. It is given by the following equation,

$$\psi_{\mp,K}(\boldsymbol{k}) = \frac{1}{\sqrt{2}}\begin{pmatrix} e^{-i\frac{\theta_{\boldsymbol{k}}}{2}} \\ \pm e^{i\frac{\theta_{\boldsymbol{k}}}{2}} \end{pmatrix}, \tag{1.3}$$

Where, $\boldsymbol{k}$ is the wavevector, and $\theta_{\boldsymbol{k}} = arctan\frac{\boldsymbol{k}_x}{\boldsymbol{k}_y}$. The Hamiltonian for the wavefunction is,

$$H_{\mathbf{K}} = v_F \boldsymbol{\sigma}.\boldsymbol{k}, \tag{1.4}$$

Here $\boldsymbol{\sigma} = (\sigma_x, \sigma_y)$ are Pauli matrices, and $v_F \approx 10^6 \mathrm{m/s}$ is the Fermi velocity. The eigen energies, $E = \pm v_F k$, correspond to π (valence band) and π^* (conduction band) of graphene respectively. The wavefunction of electrons around K′ point is given below,

$$\psi_{\mp,\mathrm{K}'}(\boldsymbol{k}) = \frac{1}{\sqrt{2}}\begin{pmatrix} e^{i\frac{\theta_{\boldsymbol{k}}}{2}} \\ \pm e^{-i\frac{\theta_{\boldsymbol{k}}}{2}} \end{pmatrix}, \tag{1.5}$$

For the Hamiltonian,

$$H_{\mathbf{K}} = v_F \boldsymbol{\sigma}^* . \boldsymbol{k}, \tag{1.6}$$

The π^* and π bands of graphene meet at six Dirac points located at the corners of graphene. The energy dispersion relation becomes linear near these points.[13] It is quantum mechanical hopping between the sublattices of graphene that results in the formation of two energy bands, which intersect near the Dirac points as shown in Figure 1.2. Electrons behave like particles with zero effective mass thus is the basis of origin of exotic phenomenon exhibited by graphene. Therefore, graphene provides a nanoplatform to study the relativistic effects in lab.

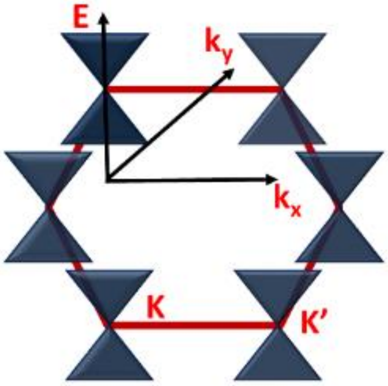

Figure 1.2 Electrons show linear energy dispersion relation around six Dirac points in graphene.

Graphene is coupled weakly with other stacked layers in graphite via van der Waal forces. If graphene is treated as a perfect two-dimensional system, then it has two acoustic phonon modes and two optical phonon modes, which are a consequence of essentially in plane vibrations of graphene's lattice. In the limit $k \rightarrow 0$, the dispersion relations are $\omega_{a\,(in\,palne)} \propto k$, and $\omega_{o\,(in\,palne)} \propto$ constant. However, the weak coupling forces between the graphene layers give rise to out of plane vibrations in the third dimension (i.e., towards c axis of graphite), which result in two additional phonon modes. These phonon modes are termed as flexural modes and refer to one optical and one acoustic mode. In the limit $k \rightarrow 0,$ the dispersion relation is $\omega_{a\,(flexural)} \propto k^2$. Acoustic flexural mode is essentially due to perpendicular vibration of monolayer graphene and dominate in low temperature regimes. The optical flexural mode basically arises due to out of plane oscillations of neighbouring atoms. The flexural modes of graphene play an important role in determining the superior thermal conductivity of graphene.[14] The thermal conductivity, however decreases with increasing the number of graphene layers and subsequently approaches that of graphite.[15] Graphene is the strongest material, with breaking strength is as high as 42 Nm^{-1}, and its Young's modulus is 1 TPa.[16]

The ballistic transport of electrons in graphene leads to very high electronic mobility in graphene. Graphene obtained by exfoliation on SiO_2 substrate possessed temperature independent mobility as high as 10000 cm^2/Vs.[17] However, removing impurities from graphene can further increase the mobility. Graphene possesses quantized conductivity (resistivity). An anomalous quantum Hall effect was predicted in graphene which made it significantly different from conventional 2-D systems.[18] Anderson localizations are absent in monolayer graphene.

1.2.1 Defects in Graphene

There are some intrinsic and extrinsic factors that control the disorder in graphene. The disorder in any form affects the transport properties of graphene. Surface ripples and topological defects are sources of intrinsic disorder in graphene. Vacancies, adatoms, sheet terminations at the edges, presence of charges on graphene's surface or substrate, and cracks are considered among the extrinsic defects. Defects modify the Hamiltonian of graphene by adding a new term in it.

$$H_{add} = \sum_i V_i(a_i^\dagger a_i + b_i^\dagger b_i), \tag{1.7}$$

Here V_i is the potential generated at the disorder site. Consequently, such defects cause a shift in the chemical potential of system and Dirac's points experience a local shift. Subsequently the spectroscopic and transport properties are modified as compared to those in a defect free lattice.[19, 20] An example is the Coulomb impurity that can generate screening effects in graphene and modifies its transport properties.

It is very much expected that thin sheet like structure will experience distortions and ripples will form on the sheet. These distortions occur due to adsorbents lying on graphene, substrate effects, scaffolds and thermal fluctuation in crystalline structure. This may result in decreased distance between carbon atoms in lattice, the rotation of p_z orbital, and readjustment in hybridization of graphene.[12]

Crystal structure distortions are topological defects and are observed as the existence of pentagons, heptagons and Stone-Wales defects (heptagon and pentagon in pair) among the regular hexagons of graphene. Crystalline deformations induced by topological defects modify the electronic paths within graphene and hence transport and spectral properties are altered.

Edges are important extrinsic defects observed in graphene. The dangling bonds and incompletely terminated hexagons at the edges provide high surface energy and impurity atoms tend to get attached with the broken bonds at the edges. Grain boundaries, microcracks, voids and self-doping are among other extrinsic defects that modify the properties of graphene.

1.3 Graphene Derived Nanomaterials

It was only after the laboratory synthesis of graphene, that provoked intense interest among the scientific community to develop variety of methods to produce graphene e.g., chemical vapor deposition[21, 22], shear exfoliation[23] assisted Langmuir Blodgett method[24], and hydrogen arc discharge exfoliation.[25] In later years, graphene derived materials became the focus and dragged the scientific attention. Numerous chemical methods[26, 27] were developed to synthesize graphene oxide[28] (GO), reduced graphene oxide (rGO) and graphene nanoplatelets (GNPs) with motivation of low cost gram scale production. In the following subsections, graphene derived materials are briefly discussed.

1.3.1 Graphene Oxide

Graphene oxide (GO) is a chemical assembly of unstacked graphene sheets with attached functional groups. The functional groups may be hydroxyl (-OH), carboxylic group (-COOH), epoxides and others. These chemical entities get attached on graphene's surface and edges by forming covalent bonds. The dangling bonds of graphene and modification in sp^2 network allow the attachment of different atoms or group of atoms to achieve desired chemical functionalization. Therefore, GO possesses mixed sp^2/sp^3 carbon domains. A schematic example of GO is presented in the Figure 1.3.

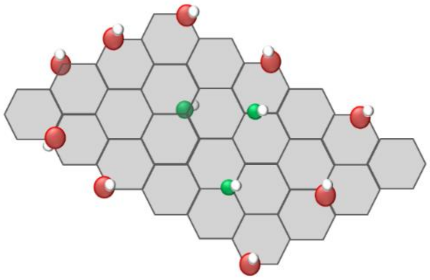

Figure 1.3 A schematic figure of GO, the attached assembly (red, green and white spheres) is symbolic of atoms or group of atoms attached on graphene sheet.

This chemically modified structure exhibits significantly deteriorated properties as compared to pristine graphene. This is because, the attached atoms or group of atoms serve the role of impurity and have drastic effects both on electrical and thermal transport properties. Attachment of aforementioned groups on graphene has advantages e.g., it improves its solubility in water and number of other solvents[26], whereas, graphene is hydrophobic. Graphene layers tend to stack together, but the covalent attachment of functional groups on basal planes is a way to intercalate the layers of graphite. It reduces the attractive forces between the sheets. The typical interlayer distance increases in layered GO structure.

The usual strategy that is adapted for the formation of GO is the oxidation of graphite using concentrated acids and different oxidizing agents.[29-31] The resultant graphite oxide is a graphitic structure that is populated with functional groups. Graphite oxide is basically a stacked structure. The nature of functional groups depends on the method and nature of chemicals used for oxidation process. In the next step, the exfoliation of graphite oxide can be carried out via different steps. The one simplest approach for exfoliation of graphite oxide is its sonication with or without surfactant.[32, 33] The other approaches include aqueous stirring of graphite oxide solution for long enough time periods.[34] Centrifugation based exfoliation is also reported in some studies.[35] Exfoliation process transforms the stacked graphite oxide to well dispersed functionalized graphene oxide sheets.

There has been an enormous research on GO in the last decade. It has found numerous applications in the field of biomedicine[36], energy storage[37], optical applications[38] among others.[39, 40]

1.3.2 Functionalized Graphene Oxide

Based on requirements and applications, GO can be modified by covalent or non-covalent attachments of amines, polymers, small molecules, DNA, drugs and proteins.[34, 41-43] These entities can be attached to -OH groups and carboxylic groups that lie on basal plane and edges of GO. Different organic solvents and cross-linking reactions are used to attach these biological and chemical species on GO. In functionalized GO, the sp^2 hybridization as found in neat graphene sheet is disrupted with formation of sp^3 hybridized networks. It is also not surprising that conductivity of functionalized GO decreases and it has insulating properties.

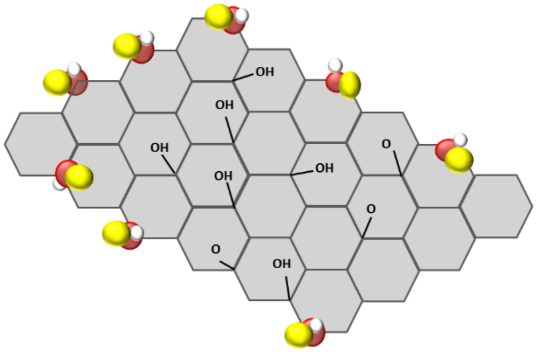

Figure 1.4 Schematic presentation of functionalized GO. The yellow spheres are symbolic of biological or chemical species, attached to carboxylic groups at the edges.

1.3.3 Reduced Graphene Oxide

Reduced graphene oxide (rGO) is graphene with no or significantly less number of oxygen containing groups, as compared to GO. However, it is important to understand that rGO is quite different from pristine graphene. Insulating behaviour in GO appears due to heavy population of hydroxyl, epoxides and carboxylic groups that reside on it. The graphene oxide is handicapped by the presence of atoms over it that contribute towards decreasing it electrical and thermal conductivity. A strategy, therefore, can be adapted to remove these groups from GO. It can be achieved by various methods, like thermal methods[44], green reduction[45], UV light assisted techniques[46] and chemically using reducing agents (e.g., sodium borohydride[47], hydrazine[48], hydroquinone[49], dimethylhydrazine[50]). The Figure 1.5 shows a stepwise description of formation of rGO. However, the transport properties of rGO definitely depend on reduction parameters and percentage of oxides that remain still present on rGO even after reduction.[51]

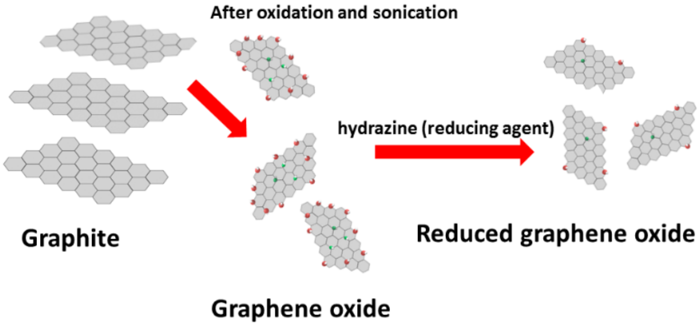

Figure 1.5 A stepwise schematic layout that distinguishes different graphene family nanostructures

1.3.4 Graphene Nanoplatelets

Graphene nanoplatelets (GNPs) are stacked layers of graphene sheets. They are not perfectly exfoliated graphene sheets and are held together by van der Waal's forces. GNPs usually possess a thickness in the range of 5 nm to 20 nm, and a diameter that equals a few microns.

GNPs can be synthesized in lab[52, 53], and they are also commercially available as well.[54, 55] Commercial GNPs have certain advantages such as low cost solution processing and gram scale production, therefore, they offer cost effective choice to further modify them chemically for numerous applications.[54, 56-60] However, one of the disadvantage of GNPs is the existence of large number of layers. The multi-layered stacked GNPs can eventually have the properties of bulk graphite.

In this work, commercially available GNPs were used. These GNPs were purchased from KNANO as black-grey powder. Their diameter ranges between 3 to 6 µm and thickness varies from 5-15 nm. The powder has an electrical conductivity 12000 S/m and thermal conductivity 3000 W/mK. The tensile and Young's modulus are of the order of 1000 GPa and 1060 GPa respectively. Figure 1.6 depicts their physical appearance.

Figure 1.6 Powdered GNPs used in this work

1.4 Ceramics (Metal Oxides and Non-Metal Oxides Nanostructures)

Miniaturization has led to significant scientific and technological advancement, which have enormous impact on everyday life moieties to space science's instruments. In brief, the technological evolution can be attributed to modern research, that encompasses the work in material science and nanoscience. In last 50 years, nanomaterials that include materials with different morphologies like nanoparticles, nanowires, nanosheets, nanobelts, nanorods, nano-discs and nano-hexagons etc. have been employed in numerous applications. Among them, ceramics as nanomaterials have been extensively researched due to their potential in a number of applications that include electrocatalysis,[61, 62] photocatalysis,[63, 64] environmental remediation,[65] biomedicine,[66] and energy storage devices[67] among others. This is because, the reduction in size and dimensions introduces exotic properties in nanomaterials, generally not found in their bulk counterparts. The novel possibilities that result due to reduced dimensions, are breath taking and therefore, nanomaterials have received tremendous attention from scientific community.

The work in this thesis is designed to include three metal oxides nanostructures i.e., magnesium oxide (MgO), magnetite (Fe_3O_4), nickel oxide (NiO) and a non-metal oxide, silica (SiO_2).

1.4.1 Magnesium Oxide (MgO)

Magnesium and oxygen as compound exist as MgO, MgO_2, and Mg_3O_2. Among these, a stable phase, MgO is included in this work. MgO, a white powder, has a cubic crystalline (NaCl like) structure with a bulk bandgap 5-7 eV. The bandgap energy varies due to quantum confinement effects as the particle size approaches the nanoscale. It's a refractory material, and is highly stable at elevated temperatures. MgO is insulating, both electrically and thermally. It is a diamagnetic material and possesses negative magnetic susceptibility. It is biocompatible material and has been used as antibacterial material. It has other biological applications as well. It is used as laxative agent, antacid, plant fertilizer, and magnesium supplement. Previous scientific studies have shown that it can also find applications as nanothermometer, dielectric material, substrate for superconducting material, passive layer for transistors (oxide barrier in spin tunnelling devices), and protective coating for plasma displays. Recently, the adsorption properties of chemically modified MgO have been studied, which provided the motivation for this work to study its photocatalytic properties after its modification as a nanocomposite material.

1.4.2 Silicon Dioxide (SiO_2)

SiO_2 appears as a white powder. It exists in amorphous and about forty crystalline forms. It is an insulating non-metal oxide with a wide bandgap (ca. 5eV or higher). It is an insulator both thermally and electrically. It is diamagnetic material and has a negative magnetic susceptibility. It is a non-toxic material. SiO_2 has found many electronic applications e.g., a substrate material. It has several biological applications as well e.g. it can be used as nanocarrier to deliver the drugs (attached to it via covalent bonding) at cancerous sites. This is because, it has a very low toxicity, and has ability to get functionalized by several polymers and molecules of medicinal value.

1.4.3 Magnetite (Fe_3O_4)

Iron and oxygen can exist combinedly in different phases, but there are few crystalline forms, that show close resemblance and can be transformed from one phase to another on variation of temperature, namely magnetite (Fe_3O_4), hematite (α-Fe_2O_3), and maghemite (γ-Fe_2O_3). Among these, magnetite is of interest because of its magnetic properties and their potentially non-toxic nature. Magnetite appears as black powder and it has inverse spinel structure. It has a wide bandgap which lies between 3 eV to 3.8 eV.[68]

Magnetite has found numerous application e.g., in catalysis, energy storage devices, chemical and biological sensing, electromagnetic waves absorption, magnetic resonance imaging, magnetic tunnel junctions, and hyperthermia etc. among others.[68]

1.4.4 Nickel Oxide (NiO)

Nickel and oxygen together can constitute different oxides that include NiO, Ni_2O_3 and NiO_2. NiO exists as green powder which turns to black when calcined at elevated temperatures. It has NaCl like crystalline structure. NiO has a non-zero magnetic moment and positive magnetic susceptibility which is a function of particle size and morphology of the nanosystems. Its bandgap energy varies between 3 eV to 3.8 eV and again it depends on exact particle size of NiO nanosystems. NiO is a very important nanomaterial as it can find electrochemical applications, particularly in fuel cells, batteries, and sensing devices.

1.5 Nanocomposites of Ceramics and Graphene Derivatives

Nanocomposites are binary, tertiary or quaternary combinations of different elements or compounds, that are held together by electrostatic interactions. These electrostatic interactions may be the primary bonds or the secondary bonds. The constituent units of nanocomposites may have different morphologies, crystal structures, and other physical or chemical properties. The nanocomposites are synthesized with an aim to fabricate a composite that can have the properties of all the constituent components. The tailored properties of nanocomposite can be adjusted by careful selection of amounts of materials that make it. For instance, the physical, chemical and biological properties of metal/non-metal oxides can be modified by formation of their nanocomposites with graphene based nanomaterials. Graphene being a rising star on the horizon of material science, provides a unique platform that can induce various desirable features in nanocomposite. A schematic view of graphene nanocomposites is shown in Figure 1.7.

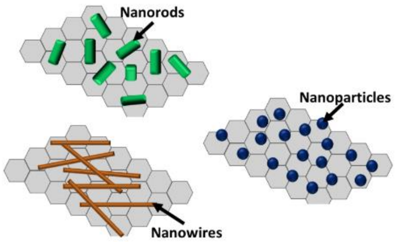

Figure 1.7 Graphene decorated with ceramics, that have different morphologies like nanoparticles, nanowires and nanorods

1.5.1 Applications

The nanocomposites obtained from this simple material graphene, have great potential. Graphene nanocomposites have found large number of applications in almost every field and have enormous impact on technological advancement. It is however not possible to cover all applications of graphene/ceramics nanocomposites that have been explored since 2004 till now, but few applications are mentioned in this section. The metal oxide embedded graphene nanocomposites have been used for energy storage applications[69-71], supercapacitors,[72, 73] sensing applications[74-77], and electromagnetic wave absorption.[78-80]

Environmental problems are also addressed by nanocomposites composed of graphene and ceramics. They have been extensively used for the treatment of wastewater, that includes removal of dyes, chemicals and metals/metal ion from water.[81-91] Graphene/ceramics nanocomposites also contribute significantly towards the treatment of antibiotic resistant pathogenic bacteria.[92-98]

1.6 Photocatalytic Applications

The reuse and recycling of water is an urgent requirement all around the world. The mushroom growth of industries has resulted a drastic generation of wastes that are released into water bodies. Detoxification of water that is contaminated with industrial wastes is essential to preserve it and to avoid the harmful effects of toxic chemicals on aquatic and human life. A list of harmful chemical contaminants that are routinely discharged in water bodies is tabulated in Table 1. 1.

Table 1. 1 A list of chemical pollutants, generally found in water bodies

Name of pollutant	Classification/source
Methyl orange, methylene blue, malachite green etc.	Synthetic dyes used in textile, plastic, leather industries.
Triton x-100	Detergents from any random industry and house hold wastes
Chlorobenzenes, chloroform, carbon tetrachloride etc.	Chlorinated liquids
Alcohols (phenols), acetone, benzenes etc.	Non-chlorinated liquids
Monuron, atrazine. Lindane, parathion, Aldrin etc.	Pesticides and insecticides
Arsenic, chromium, lead etc.	Metal and metal ions

When concentration of these contaminants in water crosses the safe limit, it becomes inadequate to use. Therefore, it becomes essential to address the decontamination of water by designing cost effective and simple strategies.

Among various strategies, photocatalysis is one of water clean-up methods that uses light (ultraviolet and visible) to induce a chain of chemical reactions in contaminated water, that consequently result the conversion of pollutants to harmless products. Heterogeneous photocatalysis has a potential due to the advantages associated with it. It was only after 1972, when photocatalytic splitting of water discovered on TiO_2 electrodes by Fujishima and Honda[99] provoked an intense interest among scientists to explore the pros and cons of heterogeneous photocatalysis. In the following half century, ever increasing demand of water clean-up has only arouse the need to setup advanced industrial grade photocatalytic units that can make use of newly fabricated materials.

In heterogeneous photocatalysis, photons induced chemical reactions take place at the catalyst and adsorbate interface that are triggered by electron transfer or energy transfer. The quantum mechanical phenomenon associated with absorption of photons by a molecule is determined by the probability of an electronic transition as given below,

$$Probability \propto E_o^2 \left|\mu_{i\to f}\right|^2 \tag{1.8}$$

Where, E_o is the amplitude of incident photons, and the transition dipole moment of an electron from an initial state ψ_i to a final state $\psi_f$is given by,

$$\mu_{i\to f} = < \psi_i|\mu|\psi_f > \tag{1.9}$$

The wavefunction of an electron here is a product of spatial, spin, and the nuclear wavefunction. Forbidden transitions have the zero-dipole moment and correspond to no excitation, and in that case the product of all the three wavefunction goes to zero. Allowed transitions can be determined by the selection rules. Absorption events are quick $\sim 10^{-15} s$, whereas, deexcitation are relatively slower. In semiconductors, the photons with energy equal to or greater than the bandgap energy of semiconductor produce electronic excitations. The electronic excitations between the discrete energy levels result in the formation of electron-hole pairs. The lifetime of electron-hole pairs is relatively longer i.e., in nanoseconds and therefore, allows the charge transfer at catalyst and solution interface. These charge carriers can follow a few pathways to generate the different active species. The various possibilities are shown in Figure 1.8.

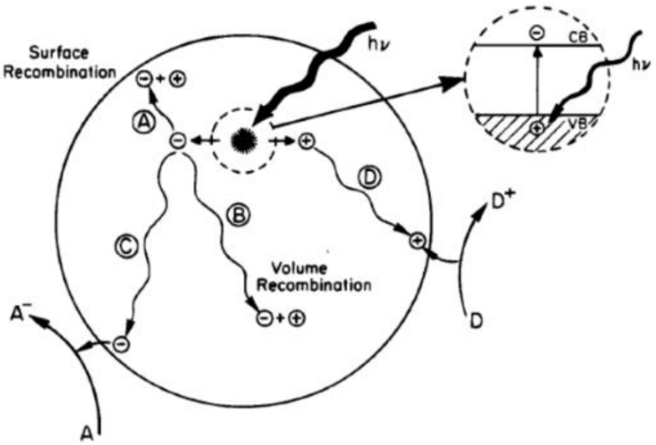

Figure 1.8 A schematic figure that depicts the possible pathways opted by charge carriers in a photocatalytic process, adapted from the work of Linsebigler *et.al.*[100]

Here, electron and holes can recombine as presented in path A and path B (surface recombination, and volume recombination respectively), photo-excited electrons can reduce oxygen as shown in path C, and holes move to the surface of semiconductor, where they oxidize donor species as seen in path D.

Band-edge position of photocatalyst and redox potential of adsorbates determine whether a semiconducting system can undergo photocatalysis. The efficiency of a photocatalytic process depends on numerous factors like recombination of electron-hole pairs. Greater the life time of these pairs, higher will be the quantum yield of the photocatalytic process. The retardation in their recombination can be achieved by their trapping. The trapping can be made possible by introduction of defects in semiconductor. Electrons and holes can get trapped on defects states, which can lengthen their recombination time. Another way to suppress the carriers' recombination is the chemical modification of semiconductor e.g., doping and composite formation with other semiconductors and metals.

In this work, it was planned to address the quick charge carriers' recombination by combining the ceramic nanomaterials with conducting graphene networks, together they form nanocomposites. The detailed analysis of graphene induced features in photocatalytic process for a nanocomposite system will be provided later in the following chapters.

There are different mathematical models to describe the reaction rate kinetics of the photocatalytic process e.g., Langmuir-Hinshelwood model,[101] direct-indirect model,[102] and the Eley-Rideal model.[103]

In this work, it was found that Langmuir-Hinshelwood model fits well to the system under consideration, which is a first order heterogeneous catalytic reaction. According to the Langmuir-Hinshelwood kinetic scheme, following equation describes the rate of reaction

$$r = -\frac{dC}{dt} = \frac{k_r K C}{1 + KC} \tag{1.10}$$

Here k_r = reaction rate constant, C = concentration of pollutant, and K is the reactant adsorption constant. Contaminant initially covers the surface of photocatalyst. As the time proceeds, due to the decomposition of pollutant, less and less surface of photocatalyst is covered by it, until the complete photodegradation occurs. Langmuir-Hinshelwood isotherms usually depict well to model the process mathematically, but the rate constants so obtained are only apparent rate constants.

In this work, we have used a textile dye, methyl orange ($C_{14}H_{14}N_3NaO_3S$) as model water pollutant. It has been widely used in industries to dye fabric and leather. The water released from industries into water bodies contains heavy amounts of dyes. This water is also usually acidic. The untreated water containing dyes is highly toxic for human life, aquatic animals, plants, and for the crops that are irrigated with polluted water. It is believed that azo dyes can be transformed to carcinogenic metabolites formed by intestinal anaerobes, some of which are excreted in feces and some are adsorbed in urinary bladder causing tumour.[104] Figure 1.9 shows powdered and aqueous forms of methyl orange. It shows a prominent absorption peak at 505 nm in water.

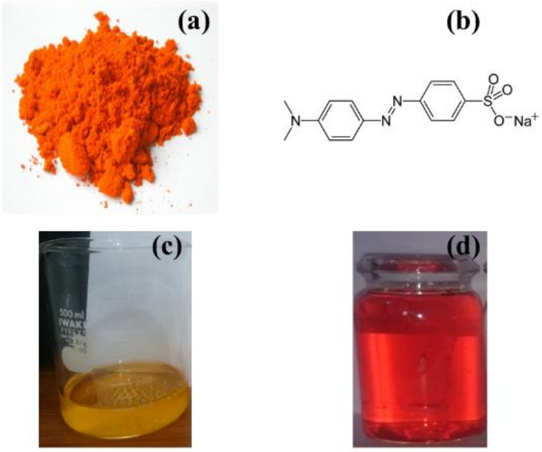

Figure 1.9 (a) Methyl orange in powder form, (b) chemical structure of methyl orange, (c) aqueous solution of methyl orange, and (d) aqueous solution of methyl orange at pH 4 (acidic).

1.7 Biomedical Applications

The devastating effects of pathogens on public health worldwide have stimulated a flurry of activity among scientific community to treat waterborne diseases and other diseases generated by pathogens. The pathogens include bacteria, protozoa, viruses, prions, helminths, protozoa, and fungi etc. Traditional methods include the use of antibiotics and conventional antimicrobial materials to kill infectious agents but the prevalence of multi-drug resistant pathogens demands the continuous need of testing novel materials that can eradicate them. World Health Organisation (WHO) provided its assessment as fact sheet on the status of mortality and morbidity among the population, stating that antibacterial resistance is present in every country including industrialized states. The risk of disease prevails in water, soil, air and can spread from one patient to another patient. For example, consider the case of United States, where 2 million people are infected every year by these pathogens and 23,000 deaths are reported annually.[93] It can be anticipated that this situation even gets worse in developing countries, where poor sanitation conditions, lack of medical facilities, and ignorance about self-hygiene can cause a higher mortality rate.

In this work, some graphene based nanocomposites are prepared to study their effect on growth inhibition of three selected model bacterial strains, two of which belong to Gram negative bacteria i.e., *Escherichia coli* (*E. coli*), and *Pseudomonas aeruginosa* (*P. aeruginosa*) and one is Gram positive, Methicillin resistant *Staphylococcus aureus* (*S. aureus*). All these three bacteria are potentially harmful. Table 1.2 presents the list of infections caused by them.

Table 1.2 A tabulated summary of infections caused by three bacterial strains

	Bacteria	**Infections**
1	*E. coli*	Neonatal meningitis, pneumonia, bacteraemia, cholecystitis, cholangitis, urinary tract infection, and diarrhoea.
2	*P. aeruginosa*	Hospital acquired infections that can also include endocarditis, septicaemia, malignant external otitis, meningitis, pneumonia, and endophthalmitis.[105]
3	*S. aureus*	Skin and soft tissue infections, food poisoning, bacteremia, infective endocarditis. It can also cause infections in animals e.g., bumblefoot in chickens, mastitis in cows etc.

The detailed line of action of prepared nanocomposites will be studied for their bacteriostatic and bactericidal activity in the next chapters. The mechanism for antibacterial activity of either ceramics nanostructures, or graphene and their combined assemblies, as nanocomposites will be included in the following chapters.

1.8 Motivation for Work

Inadequate access to clean water has gone worse due to the mushroom growth of industries. The scarcity of clean water calls out researchers to find new solutions to decontaminate the industrial waste water using new strategies that meet the stringent economic requirements. At the same time, infections caused by multidrug resistant pathogenic organisms raise the global concern to develop novel nanomaterials that have bactericidal effects. Graphene based nanocomposites offer potentially productive avenues to treat the industrial contamination in water and bacterial infections. Therefore, in this work, different graphene based nanocomposites are synthesized and characterized to address the removal of industrial chemical, methyl orange for the purification of water. In addition, the prepared nanomaterials are also tested for pathogen control. In short, rescuing public health provided the motivation to complete this work.

1.9 Organization of Thesis

The organisation of this thesis is outlined as follows: Chapter 2 reviews the literature that laid the foundation of the work; Chapter 3 discusses the theoretical basis of the experimental methods and techniques used in this work; Chapter 4 presents the synthesis, characterizations, photocatalytic and antibacterial applications of graphene nanoplatelets and MgO nanocomposites; Chapter 5 describes the synthesis and experimental results for graphene/SiO_2 nanocomposites; Chapter 6 details the fabrication of Fe_3O_4 decorated graphene nanocomposites for methyl orange removal and antibacterial applications; Chapter 7 explores the solar light activated photocatalytic performance and antimicrobial behaviour of graphene and NiO nanocomposites; finally, Chapter 8 presents a summary of the conclusions of the experimental work included in this thesis and outlines potentially productive avenues for future research building upon the results presented here.

Chapter No. 02

2. Literature Review

Overview:

This chapter reviews the literature on heterogeneous photocatalysis to establish ground for the degradation of azo dyes using graphene and ceramics nanocomposites. It will also encompass the literature necessary to develop an understanding of antibacterial applications of graphene and metal/non-metal oxides. This will build the foundation for waste water treatment and pathogen control using graphene based nanocomposites. In addition, the major gaps in literature for the two applications are also discussed.

2.1. Heterogeneous Photocatalysis

Heterogeneously dispersed nanomaterials in dyes contaminated solutions provide an efficient platform for electromagnetically induced redox reactions that influence the chemical reactivity of adsorbates. The cogent features of metal oxide semiconductors based heterogeneous photocatalysis are briefly described below. The reaction takes place at solid-liquid interface, and photocatalyst remains dispersed as solid in the solution, throughout the process. The electron can be photoexcited between discrete energy levels by electromagnetic irradiation only if the energy of electromagnetic waves is greater than or of the order of bandgap energy. To avoid the recombination of photoexcited carriers, a separation and diffusion strategy of carriers is usually adopted, which allows to initiate a series of redox reactions. Electrons (in the conduction band) initiate reduction reactions and holes (in valence band) tend to oxidize the adsorbed species. A general overview of redox reactions taking place in metal oxide based heterogeneous photocatalytic process, that subsequently lead to photodegradation of pollutants is given by following set of equations.

$$MO + h\upsilon \rightarrow MO\ (e_{CB}^{-} + h_{VB}^{+}) \tag{2.1}$$

$$h_{VB}^{+} + H_2O \rightarrow H^{+} + \mathrm{H}O^{\cdot} \tag{2.2}$$

$$h_{VB}^{+} + OH^{-} \rightarrow HO_{ads}^{\cdot} \tag{2.3}$$

$$e_{CB}^{-} + O_2 \rightarrow O_2^{\cdot -} \tag{2.4}$$

$$h_{VB}^{+} + R_{ads} \rightarrow R^{+} \tag{2.5}$$

$$MO\ (e^-_{CB} + h^+_{VB}) \rightarrow MO \qquad (2.6)$$

$$HO^{\cdot} + \text{Pollutant} \rightarrow\ H_2O + CO_2 \qquad (2.7)$$

However, it can be observed from these equations that the carriers' recombination occurs as well that leads to heat dissipation and emission of light. The separation time of carriers is detrimental towards efficiency of photodegradation, therefore, trapping of carriers is essential for sustaining the redox reactions for the complete degradation of pollutants. One of the methods is addition of sacrificial electron donors that act as hole traps.[106, 107] The other methods to suppress the carriers' recombination include building p-n and non p-n heterostructures of metal oxides,[108] doping,[109] and use of nanocomposites.[107]

The above-mentioned mechanism is generally followed by metal oxides. However, iron based compounds like magnetite can be utilized in a slightly different photocatalytic mechanism termed as heterogeneous Fenton-like reactions. In the presence of H_2O_2, the iron containing species attached to a catalytic support undergo the following reaction,

$$Fe^{2+} + H_2O_2\ \rightarrow\ Fe^{3+} + HO^{\cdot} + OH^- \qquad (2.8)$$

$$Fe^{3+} + H_2O_2\ \rightarrow\ Fe^{2+} + HOO^{\cdot} + H^+ \qquad (2.9)$$

Use of metal oxide based on heterogenous photocatalysis and Fenton-like photocatalytic reaction has the advantage that highly reactive oxygen species, $HO^{\cdot}$radicals are produced in both processes, which can decompose the dyes completely and non-selectively by oxidizing them.[110-112]

2.2. Graphene based Nanocomposites for Photocatalysis

Metal oxides e.g., titania (TiO_2), and zinc oxide (ZnO) are conventional photocatalysts and have been used extensively for the treatment of dyes contaminated water since many years. Nevertheless, the fabrication of novel photocatalysts is needed for the increasing demand of clean water. The scientific community has put efforts to develop cost cutting methods for the waste water clean-up. Alongside increasing the efficiency of photocatalytic process is important to meet the ever-increasing water pollution. Graphene based nanocomposites provide an interesting platform to enhance the photocatalytic performance of neat metal/non-metal oxides. This is due to outstanding properties of graphene family nanomaterials. Metal oxides and graphene synergistically govern the photocatalytic process in an effective manner. A summary of recent studies on degradation of textile dyes is tabulated in Table 2. 1.

Table 2. 1 Graphene based metal/non-metal oxide nanocomposites for oxidative degradation of dyes

Nanocatalyst	Light source	Dye	Removal efficiency/time	Reaction conditions	Reference
Graphene-NiO	UV light	Methyl orange	90.3% in 75 min	Not given, 0.05 g catalyst	[113]
Graphene-NiO	Visible light	Methyl orange	78% in 180 min	Not given, 0.05 g catalyst	[113]
Graphene-TiO_2	Visible light	Methyl orange	>65% in 180 min	10 mg/L dye, 1 gL^{-1} catalyst	[114]
GO-ZnO	Solar light	Methyl orange	97% in 120 min	$5x10^{-5}$M dye, 50 mg/50 mL catalyst	[108]
rGO-SnO_2	Visible light	Rhodamine B	130 min	$5.3x10^{-3}$mM dye, 6.3 mg/100 mL catalyst	[115]
rGO-SiO_2	300 Watt Xe lamp	Rhodamine B	98.99% in 60 min	10 mg/L dye, 12.3 mg/50 mL catalyst	[109]

Graphene-TiO_2	UV light	Methyl orange	95% in 30 min	20 mg/L dye, 0.25 g/L catalyst	[112]
Graphene-TiO_2	Visible light	Methyl orange	100% in 60 min	5x10^{-5}M dye, -	[116]
Graphene-WO_3	Stimulated sunlight	Methyl orange	92.7% in 120 min	0.025 gL^{-1} dye, 1 g/L catalyst	[117]
rGO-ZnO	Ultraviolet light	Methyl orange	94% in 90 min	15 mg/L dye, -	[118]
GO-TiO_2	Ultraviolet light	Methyl orange	95% in 9 min	10 mg/L dye, 0.5 g/L catalyst	[119]
GO-Fe_3O_4	Ultraviolet light	Acid orange 7	> 90% in 180 min	0.1 mM dye, 0.2 g/L catalyst	[120]
rGO-iron oxide	Sunlight	Methylene blue	100% in 60 min	10 mg/L dye, 2 mg/12 mL catalyst	[121]
Fe_3O_4-hydrophilic graphene	500 Watt mercury lamp	Methyl orange	87.68% in 30 min	10 mg/L dye, 3 mg/50 mL catalyst	[122]
GO-Fe_2O_3	Visible light	Rhodamine B	99% in 80 min	100 mg/L dye, 0.1 g/100 mL	[123]
rGO/α-Fe_2O_3	Sunlight	Methyl orange	97.8% in 4 h	10 mg/L dye, 50 mg/150 mL	[124]
rGO/CeO_2	Visible light	Methyl orange	88.3% in 60 min	1 mM dye, 0.5 g/L catalyst	[125]
Graphene/Mn_2O_3	UV light	Methylene blue	84% in 160 min	1.2x10^{-5} M dye, 0.5 g/L catalyst	[126]
rGO/ZnO	Visible light	Rhodamine B	>95% in 40 min	10 mg/L dye, 0.125 g/L catalyst	[127]

This survey indicates that several studies have investigated the photo-degradation of numerous dyes using graphene and metal/non-metal oxides nanocomposites based on photocatalysis. This is due to following advantages that are associated with both species i.e., metal oxides and graphene family nanostructures. i) The nanomaterials offer high surface area which results due to contribution of metal/non-metal oxide nanostructures and graphene. High surface area is useful for adsorption of organic pollutants on the surface of nanocomposite. The adsorption of pollutants may contribute partially or fully towards pollutant removal. ii) Inclusion of graphene, provides a support for the growth of nanostructures on it. It helps in reducing the agglomeration between the nanostructures and thus reduces the particle size. Agglomeration and increased particle size have negative impacts on photocatalytic activity. iii) The discrete energy levels of metal oxides provide energy states with definite bandgap. The bandgaps allow the photoexcitation of electrons from one state to another state. These photo-excited carriers can induce redox reactions. iv) To achieve the complete degradation of organic dyes, it is necessary to lengthen the recombination time of carriers. The presence of graphene based materials in nanocomposites provide conducting channels. These channels provide the pathways for photo-excited carriers that readily travel from conduction band of attached species towards graphene. It delays the recombination of carriers. Greater the time, electrons and holes are available for oxidations and reduction process, higher will be the degradation of pollutants. All these merits of graphene and metal/non-metal oxide nanocomposites make them superior materials for the clean-up of dye contaminated water.[110]

In addition, photo-Fenton type reaction also provides an efficient way to remove textile pollutants from contaminated water. This is achieved by Fe containing compounds e.g., magnetite (Fe_3O_4) which has been found to work as an efficient photocatalyst based on its high Fenton activity in the presence of H_2O_2. Its high degradation efficiency is attributed to its unique features such as i) The distribution of Fe^{3+} at both tetrahedral and octahedral sites, and presence of Fe^{2+} at octahedral sites. According to Haber-Weiss mechanism,[128] this unique distribution is helpful towards initiating the conversion of H_2O_2 to radicals, which are reactive oxygen species (ROS) and are essential for degradation of organic dyes. ii) The presence of both Fe^{2+} and Fe^{3+} in Fe_3O_4

facilitates the reversible oxidation and reduction of both species without a change in its structure. Fe containing compounds provide additional benefits other than removing pollutants. The best advantage is the magnetic separation of photocatalyst from cleaned water. Magnetic separation strategy is simple and cost saving.

Apart from all the work done in the field of graphene nanocomposites based photocatalysis, there exist gaps that need to be filled and demand the immediate attention of scientific community. The shortfalls in literature are discussed point by point. i) Adsorption is among other methods that are used for removal of pollutants. Adsorption can also work side by side and can decrease the concentration of contaminant to some extent by oxidizing it prior to exposure of contaminated water to light. Adsorption properties of GO/MgO for methylene blue[129] are reported previously, but there exists no literature for photodegradation of methyl orange using graphene/MgO and graphene/SiO_2 nanocomposites. There is also limited number of scientific reports on photocatalytic activity of NiO/carbon nanocomposites. It is, therefore, attractive to explore the unexplored nanomaterials. ii) In previous studies, the inactivation of photocatalyst has been observed during repeated cycles of use. It is caused due to the dissolution of metal ions in the acidic media via a process called as leaching.[130, 131] Leaching may be due to inefficient support and depends on interaction between support and attached species. This process can decrease catalytic efficiency of material, therefore, the photocatalysts with no leaching are highly desirable for recycling purpose. iii) Carbon purity is a major factor that governs the percentage photodegradation by controlling the recombination time of carriers. Different graphene family nanostructures have different electrical conductivity.[51, 132] The conductivity of GO, rGO, GNPs and pristine graphene is different due to presence/absence of atoms in each form of carbon. The provision of conducting networks for the flow of electrons plays the vital role in lengthening the lifetime of photo-excited carriers. Insulating GO, and semiconducting rGO behave differently due to attached -OH and -COOH groups on graphene's planar structure. Carbon in pure form as pristine graphene or GNPs can provide better conducting channels, which enable fast transfer of electrons from conduction band of attached specie to them. In the past few years, mostly GO and rGO have been used as carbonaceous support.[133, 134] Therefore, the graphene with least number of functional groups are vital for the development of efficient photocatalysts. It can be envisioned that use of graphene in its pure form will pave the way towards enhanced photocatalytic efficiency.

2.3 Bacterial Growth Inhibition

The high morbidity and mortality rate around the globe was controlled by invention of antibiotics in 20th century. Antibiotics can effectively control many diseases but over the time, many pathogenic microorganisms have gained resistance against antibiotics. It poses serious risk of disease spread and demands urgent attention of scientific community to address the complications related to these infectious microorganisms. Different nanomaterials have been extensively used for microbial control. Among these, silver (Ag) nanoparticles,[135, 136] gold (Au) nanoparticles,[137, 138]ZnO nanostructures,[139-141] and TiO_2 nanostructures[142-145] are well known for their antibacterial properties. TiO_2 is known to combat bacteria under UV light irradiation, whereas ZnO has effective antibacterial performance under visible light conditions. There are various mechanisms that have been proposed to describe the line of action of these nanostructures to combat bacteria. One of the factors that affect the growth of bacteria in the presence of antibacterial nanomaterials is their surface area. The high surface to volume ratio provides the better contact between nanomaterial's surface and bacteria during the exposure of nanomaterial to microorganisms. During the contact time, antibacterial nanomaterials may target the bacterial membranes by indenting it thus destroying the bacterial integrity. Further, the nanomaterials may also enter the bacterial cell and can produce a different molecular weight regions inside bacteria, where they may attack the respiratory organelles, which induces cell death.[135] The other toxic effects of metal ions like Ag^+, Au^+ that enter the bacterial cell, include the inhibition of phosphate uptakes, generation of transmembrane proton gradient,[146] production of complexes with bases in deoxyribonucleic acid (DNA), enzyme inactivation, inhibition of oxidation of glucose etc.[147] For inorganic oxides, somewhat similar mechanisms as mentioned above are suggested for antimicrobial activity of inorganic metal oxides. One of the mostly reported mechanism for the growth inhibition of bacteria by inorganic oxides nanostructures is the generation of reactive oxygen species (ROS). Various studies have proposed that radicals and singlet oxygen are produced during interaction of bacteria and metal oxides.[148-150] The generation of these ROS is fatal towards bacteria. Some studies have shown that the antibacterial activity of a nanomaterial is size dependent and smaller nanoparticles produce much better bacteriostatic effects as compared to larger particles.[151] This is due to large surface area of smaller size particles. The accumulation of metal oxides nanostructures on the surface of bacteria may produce abrasive effects on the outer layer of bacteria which can be subsequently disorganized. The rupture of bacterial boundaries stops the normal function of cell which may lead to cell death.[139] According to another hypothesis, the accumulation of metal oxides nanostructures on the surface can be followed either by their internalization or an electrostatic binding with the surface of microbes.[152] Although, an extensive work has been done to inhibit the bacterial growth but due to excessive use of antibiotics, bacteria have gained resistance against many pathogen control drugs. Therefore, it is need of the hour to fabricate novel nanomaterials that have antimicrobial properties. In the following section, one of such class of novel antimicrobial materials that are fabricated very recently is discussed.

2.4 Antibacterial Activity of Graphene based Nanocomposites

The isolation of graphene[10] and chemical synthesis of graphene family nanostructures[132] paved the way for fabrication of novel nanocomposites and investigation of their performance in biomedical applications. The performance of different graphene related nanostructures i.e., rGO, GO, graphene on substrates and graphene's nanocomposites with metal oxides is tabulated in Table 2. 2. For this purpose, *E. coli,* and *P. aeruginosa* are selected as representative of Gram negative bacteria and *S. aureus* is chosen as representative of Gram positive bacteria. This comparison will not only provide an overview of the extensive use of graphene related materials in the field of biomedicine but will also give an insight to new dimensions that need to be explored. The choice of these materials provides a new strategy to pursue the solutions to eradicate the diseases caused by multi-drug resistant bacteria.

Table 2. 2 A comparative review of antibacterial performance of graphite and graphene based nanomaterials. Here zone of inhibition is written as ZOI, nanocomposites as NC, nanoparticles as NPs

Material	**Morphology**	**% cell inactivation /(ZOI) for *S. aureus***	**% cell inactivation /(ZOI) for *P. aeruginosa***	**% cell inactivation / (ZOI) for *E. coli***	**Reference**
Graphite	Sheet	Not tested	Not tested	26 ± 4.8%	[153]
Graphite oxide	Sheet	Not tested	Not tested	15 ± 3.7%	[153]
Graphene oxide	Sheet	Not tested	Not tested	69.3 ± 6.1%	[153]
rGO	Sheet	Not tested	Not tested	49.5 ± 4.8%	[153]
rGO coated on cloth	Sheet on cloth	Not tested	Not tested	98%	[154]
Graphene oxide film	Sheet	61%	Not tested	51%	[155]

Graphene on Cu substrate	Sheet	34%	Not tested	56%	156
Graphene oxide	Sheet	Not tested	Not tested	Growth is enhanced	157
Graphite	Sheet	< 10%	< 10%	Not tested	158
Graphene-R	Sheet	ca. 49%	ca. 83%	Not tested	158
Graphene oxide	Wrinkled nanosheets	ca. 99%	Not tested	ca. 99%	159
Graphene oxide	Sheet	Growth is enhanced	Not tested	Growth is enhanced	160
Graphene oxide	Sheet	No effect	Not tested	No effect	161
Graphene oxide	(i) Larger sheets (ii) Smaller sheets	Not tested	Not tested	(i) 100% (ii) 60%	162
Graphene oxide	Sheets	Not tested	Not tested	50%	163
Few layered graphene-ZnO	Nanoparticles on sheets	Not tested	Not tested	6-11 mm at concentration 25-75 μL	164
Cu and graphene activated ZnO	Irregular shaped nanostructures on sheets	16 mm	Not tested	16 mm	165
Graphene-SnO$_2$	Nanoparticles on sheet	Complete eradication (0.50 mg/mL, 24 h)	Complete eradication (0.50 mg/mL, 24 h)	Not tested	166
rGO-TiO$_2$	Thin films	Not tested	Not tested	7.5 times more growth inhibition as compared to bare TiO$_2$ (under sunlight irradiation)	167
Magnetic rGO-TiO$_2$	Nanoparticles on sheets	Not tested	Not tested	99%	168

GO-ZnO	Nanowires on sheets	Not tested	Not tested	95-99.5% (under visible light irradiation)	169
rGO-Fe_3O_4	Nanoparticles on sheets	92.79%	Not tested	93.09%	170
Graphene-Fe_3O_4	Nanoparticles on sheet	Not tested	Not tested	97% at 100 μg/mL	97
Magnetic-GO NC	Nanoparticles on sheet	Not tested	Not tested	91.49% ± 2.82% at 100 μg/mL	171

In the light of Table 2. 2 and recent work, it can be established that graphene, GO and rGO have a controversial antibacterial activity.[157, 160, 172, 173] In few studies it has been shown that antibacterial activity of GO depends on its purity. The reaction conditions (e.g., pH) during synthesis, and the functional groups or atoms/group of atoms (e.g., carbonyl, epoxy, and hydroxyl groups) attached on graphene sheets are the major factors that affect antibacterial activity of GO and rGO.[173] However, many studies based on graphene nanocomposites firmly establish their strong antibacterial characteristics as detailed in Table 2. 2.

There are several mechanisms that are suggested for the bacterial death induced by two-dimensional sheet like graphene based materials and their nanocomposites. These mechanisms are discussed in the following. i) Highly wrinkled surface of graphene oxide films develops a surrounding contact with bacteria, which acts as a robust trap for bacteria. The wavy and corrugated surface and nanoscale grooves are source of roughness that endows GO films with antimicrobial properties. The toxic effects produced by rough and wrinkled surface are manifested as damaged bacterial membranes.[159] ii) Wrapping effect is another mechanism that is mostly reported for graphene based materials. The 2-D sheet like structure of graphene develops an intimate contact with bacteria which isolates them from their environment that contains both nutrients and suitable aerobic atmosphere. This isolation proves to be fatal for bacteria. This mechanism strongly depends on size of sheets. Larger sheets being able to completely wrap bacteria have stronger antibacterial activity than smaller sheets.[162] However, in some reports, several bacteria were found viable after their separation from sheets.[174] iii) Orientation of graphene or GO sheets also influence the bacterial inactivation. It was proposed that graphene edges act as cutters. The edges when meet bacterial surface can rupture the cell membranes and cell walls. This results the leakage of cytoplasmic content and lipid extraction from membranes, which stop the normal functioning of cell and induces cell death.[175-177] iv) Charge transfer between graphene surface and bacteria can harm bacterial membrane integrity. Graphene prepared on different substrates like Cu, SiO_2 and Ge were studied to manipulate the electrostatic interactions between graphene and bacteria.[92] It was proposed that respiratory proteins behave like n-type semiconductor with a definite bandgap.[178] Upon physical contact between graphene and bacteria, a Schottky barriers is formed between them. Graphene being a good conductor accepts electrons from microbial membranes. An imbalance of charge on membranes generates ROS independent oxidative stress and destroys the normal respiratory process thus damaging the bacterial viability. v) Generation of oxidative stress is another cause of cell death.[179] The production of ROS is the primary source of oxidative stress. In addition, the oxidative stress may be due to all of the above-mentioned mechanisms.[153] Oxidative stress can cause disruption of cellular metabolic pathways by oxidizing cellular proteins, nucleic acids and lipids. Loss of glutathione[175] and ROS quantify the oxidative stress. It was proposed that generation of hydroxyl radicals due to interaction of water and GO defects can contribute to oxidative stress via interaction with carbonyl groups present in cell wall.[180] It was observed that all the graphene derived materials and nanocomposites showed differential cytotoxicity towards Gram positive and Gram negative bacterial strains. This can be attributed to different chemical compositions of the cell boundaries possessed by two classes of bacteria.

These mechanisms establish that GO, rGO and graphene possess unique ways to kill bacteria that can be ascribed to their peculiar two-dimensional geometry and intrinsic electrical and chemical properties. These features of graphene family nanostructures can be incorporated with those of metal/non-metal oxide antibacterial materials to achieve the synergistic effect of both species for pathogen control in a highly efficient way. However, the literature review shows that there is much to explore in this field. For instance, MgO has well known antibacterial properties[181] and it is biocompatible, which makes it potential candidate for evaluation of antibacterial features of graphene/MgO nanocomposites. Similarly, nano sized SiO_2 is again a biocompatible nanomaterial, but there is a lack of literature on effects of graphene/SiO_2 nanocomposites for bacterial growth inhibition. Moreover, there is need to conduct a systematic study that explores the effects induced by increased amount of graphene in their nanocomposites, on their bacteriostatic or bactericidal activity. The survey also depicts that the fabrication of novel materials with bactericidal properties rather than bacteriostatic features is need of the hour to tackle the dangers associated with drug-resistant bacteria. Keeping in view these loopholes, it is envisaged in this thesis to conduct a systematic study that will focused to probe the impacts of graphene on antibacterial activity of unexplored graphene based nanocomposites with an aim to achieve complete pathogen control.

2.5. Summary

The review covers the recent trends and development in photocatalytic and antibacterial properties of graphene based nanomaterials. Nevertheless, there is much to explore in wastewater treatment and bacterial growth inhibition. A foundation is developed to understand the shortcomings and experimental gaps in the present state of research associated with dye contaminated water and pathogen control and hence the thesis is planned to endeavour a study that is aimed on the development of i) cost saving, recyclable photocatalysts for complete photodegradation of methyl orange and, ii) novel bactericidal antibacterial graphene based nanocomposites that can completely inhibit the growth of *P. aeruginosa, S. aureus,* and *E. coli*.

Chapter No. 03

3. Synthesis and Experimental Techniques

Overview:

In this chapter, a concise and conceptual introduction to synthesis of metal/non-metal oxide and graphene nanocomposites is presented. This chapter also provides the basic principles and theoretical background of experimental techniques that have been employed to acquire data. The instrumentation and experimental procedures associated with the measurements undertaken are also described briefly.

3.1 Introduction

There are number of ways to synthesize inorganic oxides nanostructures and their nanocomposites with graphene family nanomaterials. Chemical methods that include solvothermal method, hydrothermal method, co-precipitation method and sol-gel method are usually employed for the synthesis of powdered nanomaterials. There are numerous advantages that are associated with use of these methods like high yield of end products, synthesis of nanomaterials with desired morphology, and cost saving.

Next, there are number of powerful experimental tools that are available to characterize carbon based nanostructures and metal/non-metal oxides. There are different techniques that can be used to investigate physical and chemical properties of graphene and inorganic oxides individually and their nanocomposites. The most common characterization tools include Raman spectroscopy, field emission scanning electron microscopy (FE-SEM), transmission electron microscopy (TEM), selected area electron diffraction (SAED), energy dispersive X-ray spectroscopy (EDX), X-ray diffraction (XRD) and Fourier transform infrared (FTIR) spectroscopy. The unique and complete picture of a nanomaterial is obtained by combining the information acquired from these individual techniques, as each tool furnishes complementary information.

The need of multiple experimental techniques for the characterization of nanomaterials under investigation is inevitable. Here, a brief account of information about the nanomaterials furnished by each technique is given. Raman spectroscopy is considered as a tool that provides fingerprints of carbon based nanostructures and their nanocomposites. It provides a valuable insight to vibrational modes of solids by giving information about perfection (defects), composition, and number of layers in graphene based materials. FE-SEM and TEM are useful imaging techniques. Both provide picture of morphology of the surface of nanomaterial. These imaging techniques are useful to image graphene, metal/non-metal oxides, and their nanocomposites. An information about texture, sheet's dimensions, particle sizes, and wire's dimensions etc. can be obtained from these techniques. EDX analyzer usually coupled with either FE-SEM or TEM is used to determine the elemental compositions of nanomaterials under investigation. SAED is a complementary method associated with TEM and can be performed inside it. It delivers the crystallographic information about the nanomaterial. XRD is crystallographic technique that is used to probe the crystal structure of the material. The information about crystallinity and lattice dimensions can be acquired from it. Considering the nanomaterials under investigation, information regarding crystal structure of metal/metal oxides is obtained by XRD. Vibrating sample magnetometer (VSM) is used to determine magnetization, magnetic dipole moment and coercivity of magnetic materials.

Finally, for photocatalytic applications of prepared samples, a photocatalytic chamber equipped with different light sources is used to investigate wastewater treatment. To monitor the optical changes associated with dye degradation, UV-vis spectrophotometer is used. It probes the solution of dyes and nanomaterials by acquiring data of absorbance. Photodegradation of azo dyes can be calculated indirectly from data obtain by UV-vis spectrophotometer. In addition, the optical bandgap energies of nanomaterials can be determined indirectly using UV-vis spectrophotometer.

For antibacterial applications, a spectrophotometer is used to obtain optical density (OD) of bacterial cultures at 600 nm. The data acquired using spectrophotometer gives an account of bacterial growth profile. Bacterial viabilities can be indirectly obtained using the information collected by this instrument.

3.2 Synthesis of Graphene and Metal/Non-Metal Oxides Nanocomposites

Chemical methods are used to synthesize MgO and GNPs nanocomposites, graphene/SiO_2 nanocomposites, graphene/Fe_3O_4 nanocomposites and graphene/NiO nanocomposites. The methods are explained in the following sub-sections.

3.2.1 MgO and GNPs Nanocomposites

The materials used in the synthesis of MgO and GNPs nanocomposites were: magnesium nitrate hexahydrate ($Mg(NO_3)_2.6H_2O$) (99%, Merck), sodium hydroxide (NaOH) (>98%, Merck), ethyl alcohol (99%, Merck), GNPs (> 99%, KNano), and distilled water.

The nanocomposites were synthesized by sonication assisted solvothermal method. The GNPs were dispersed in a mixed solvent of absolute ethanol and distilled water (1:1) by sonication for few hours at room temperature. At this stage 14.74 g of $Mg(NO_3)_2.6H_2O$ was dispersed in the above solution, followed by sonication. NaOH was prepared in a mixed solvent of distilled water and absolute ethanol (1:1). The sonicated solution was added to the basic solution in a controlled manner, followed by vigorous magnetic stirring at 1200 rpm. This solution was transferred to tightly sealed Teflon lined autoclave. The autoclave was transferred to a pre-heated electric oven at 180^oC for 10 h. After cooling down the autoclave naturally at room temperature, the collected material was washed several times using distilled water and ethanol. The precipitates so obtained were dried in an electric oven at 100^oC for 2h. To completely transform the $Mg(OH)_2$ phase to MgO cubic phase in the composite material, it was given a post annealing session at 500^oC for 3 h in a tube furnace. The MgO nanohexagons were prepared by following same route but without the addition of GNPs. Two nanocomposites labelled as MgO/GNPs 12% and MgO/GNPs 25% were prepared with different loadings of GNPs, i.e., 12% and 25% of MgO, respectively.

The chemical reaction for formation of MgO is given below,[182]

$$Mg(NO_3)_2.6H_2O + 2NaOH \xrightarrow{Heat} Mg(OH)_2 + 2NaNO_3 \tag{3.1}$$

$$Mg(OH)_2 \xrightarrow{Heat} MgO + H_2O \tag{3.2}$$

The electrostatic charge transfer between MgO and C results in the formation of MgO/GNPs nanocomposites.

3.2.2 Graphene/SiO_2 Nanocomposites

Tetraethyl ortho silicate (TEOS) (99%, Fluka), liquid ammonia (NH_3) (32%, Millipore Sigma), ethyl alcohol (99%, Merck), GNPs (>99%, KNano), and distilled water were used in the fabrication of monodispersed SiO_2 particles and graphene/SiO_2 nanocomposites. All the chemicals were used as obtained.

The synthesis process was initiated by mixing and stirring definite amounts of TEOS in the double solvent of ethyl alcohol and distilled water in the ration of 10:3 (v/v). The pH of the solvent was controlled by NH_3. With careful monitoring of pH, different amounts of sonicated GNPs were added to the solution. The reaction was completed in 2 h. The solution was dried at 373.15 K for 12 h in an electric oven with the post annealing session at 923.15 K for 1 h in a tube furnace. The SiO_2 was prepared under similar conditions without the addition of GNPs. Two nanocomposites labelled as S_y, and S_z were prepared with different feed ratios of GNPs, i.e., y = 80 mg, and z = 100 mg.

The underlying chemical mechanism for the formation of SiO_2 is either alcohol condensation or water condensation.[183] TEOS undergoes hydrolysis, given by following reaction,

$$Si(OC_2H_5)_4 + xH_2O \xrightarrow{Heat} Si(OC_2H_5)_{4-x}(OH)_x + xC_2H_5OH \tag{3.3}$$

The intermediate products either undergo alcohol condensation or water condensation.

$$\equiv Si - OC_2H_5 + HO - Si \equiv \ \longrightarrow \ \equiv Si - O - Si \equiv + C_2H_5OH \tag{3.4}$$

$$\equiv Si - OH + HO - Si \equiv \ \longrightarrow \ \equiv Si - O - Si \equiv + H_2O \tag{3.5}$$

Overall, the reaction can be presented by following equation,

$$Si(OC_2H_5)_4 + 2H_2O \ \longrightarrow \ SiO_2 + 4C_2H_5OH \tag{3.6}$$

Ammonia acts as catalyst and serves to speed up the reaction. In presence of graphene, the silica grows on it and a charge transfer takes place between the two species.

3.2.3 Graphene/Fe_3O_4 Nanocomposites

Ferric chloride hexahydrate ($FeCl_3.6H_2O$) (98%, Sigma Aldrich), ferrous chloride tetrahydrate ($FeCl_2.4H_2O$) (99%, Sigma Aldrich), sodium hydroxide (NaOH) (Calibochem), ethyl alcohol (99%, Merck), isopropyl alcohol (99%, Sigma Aldrich), graphene nanoplatelets (GNPs) (>99%, KNano), and distilled water were used for the synthesis of Fe_3O_4 nanoparticles (NPs) and graphene/Fe_3O_4 nanocomposites. All the chemicals were of analytical grade.

Appropriate amounts of $FeCl_3.6H_2O$ and $FeCl_2.4H_2O$ were added in 50 ml of distilled water. 1M aqueous NaOH was added to the precursor solution drop by drop at room temperature, under constant stirring. The GNPs solution (sonicated in a mix solvent of distilled water and isopropyl alcohol) was added to the basic solution. The pH was maintained at 10. The solution was stirred for 30 minutes and was transferred to a Teflon-lined autoclave, for a heat treatment at 80^oC. The precipitates were collected by centrifugation, and were dried overnight in an electric oven at

80^{o}C. Then the grinded powder was annealed in a tube furnace at 500^{o}C for 4 h in N_2 atmosphere. Fe_3O_4 nanoparticles were prepared using similar method, without adding GNPs.

Magnetite nanoparticles are prepared typically by simultaneously co-precipitating two ions Fe^{2+} and Fe^{3+} in aqueous solution.[184]

$$Fe^{2+} + Fe^{3+} + 8OH^- \longrightarrow Fe_3O_4 + 4H_2O \tag{3.7}$$

This reaction takes place under basic conditions. The drying and annealing in a non-oxygen atmosphere is essential for the formation of magnetite. The magnetite nanoparticles grow on graphene and develop van der Waal's interaction with it due to the charge transfer that takes place between two species.

3.2.4 Graphene/NiO Nanocomposites

Nickel (II) nitrate hexahydrate ($Ni(NO_3)_2.6H_2O$) (99. 99 % Sigma Aldrich), isopropyl alcohol (≥98 % Sigma Aldrich), ammonia solution (32% Millipore Sigma), GNPs (100% KNANO) and distilled water were used without further purification for the synthesis of graphene/NiO nanocomposites.

2.617 g $Ni(NO_3)_2.6H_2O$ and two different quantities of GNPs were dispersed in a mix solvent (isopropyl alcohol and distilled water). The pH of solution was adjusted using liquid NH_3. This solution was transferred to autoclave after stirring for 2 h. The autoclave was heated at 180^{o}C for 6 h. The precipitates were collected after centrifugation. Later, the precipitates were dried in an electric oven at 95^{o}C for 12 h. The dried and grinded samples were annealed at 350^{o}C for 3 h. The neat NiO was prepared using similar method without addition of GNPs.

The metal precursor (in solid form) converts to ions in aqueous solution,[185]

$$Ni(NO_3)_2.6H_2O \longrightarrow Ni^{2+} + 2NO_3{}^- + 6H_2O \tag{3.8}$$

$$NH_3 + H_2O \longrightarrow NH_4{}^+ + OH^- \tag{3.9}$$

$$Ni^{2+} + 2OH^- + xH_2O \longrightarrow Ni(OH)_2.xH_2O \tag{3.10}$$

$$Ni(OH)_2.xH_2O \xrightarrow{Heat} NiO + xH_2O \tag{3.11}$$

NiO obtained via above reactions grows on the surface of graphene and develops attractive interactions with it via formation of graphene/NiO nanocomposite.

3.2.5 Growth Model for Graphene based Nanocomposites

GNPs are stacked layers of graphene sheets that are held together by secondary bonding, known as van der Waal’s bonding.

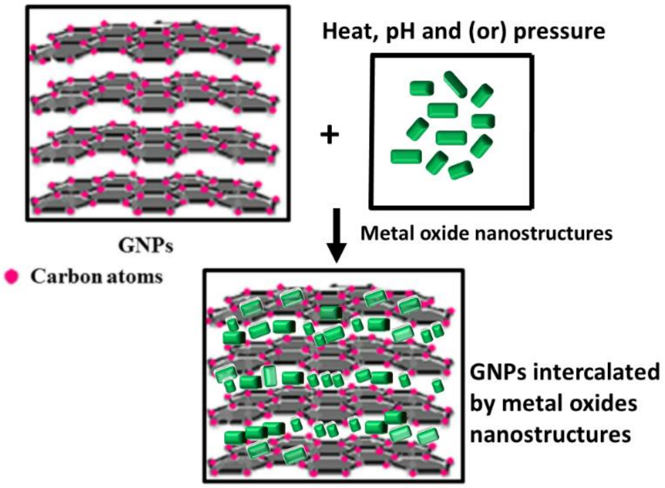

Figure 3. 1 Growth mechanism for metal/non-metal oxides and graphene nanocomposites via intercalation of GNPs.

The presented synthesis methods were designed with an aim to intercalate the GNPs using different metal/non-metal oxide nanostructures, thereby reducing the attractive forces between sheets in GNPs. A general growth mechanism for afore-mentioned nanocomposites is explained schematically in Figure 3. 1. The precursors (metal salts/TEOS) are converted to ions in aqueous form. Drop-wise addition of basic solution promotes the formation of metal/non-metal oxides nanostructures. The graphene sheets offer active sites and a large surface area for the growth of metal/non-metal oxide nanostructures under given reaction conditions (i.e., heat treatment, pressure, and pH). This gives the advantage that a large surface area is available for the nucleation of the primary particles, thereby reducing the particle size of metal/non-metal oxides in nanocomposite as compared to neat metal/non-metal oxides. The confining effect of graphene sheets also contributes to stop the nucleation process after a certain limit, thus leading to the reduced particle size as compared to pristine metal/non-metal oxides. This behaviour has been previously observed in graphene based nanocomposites.[186] These nano-sized species serve to intercalate the graphene sheets as they get drafted on graphene, both above and below them. This reduces the van der Waal’s interaction between them. Under applied reaction conditions, an electric charge transfer is inevitable between graphene and attached species, which results the random distribution of metal/non-metal oxides over the entire plane of graphene sheets. Thus, the obtained final product shows a bi-phase chemical entity called nanocomposite which is comprised of graphene sheets decorated by metal/non-metal oxide nanosystems. The thermal treatment (annealing) of the nanocomposites serves to i) improve the crystallinity of attached metal oxides, and ii) convert the metal/non-metal hydroxides to metal/non-metal oxides.

3.3 Raman Spectroscopy

3.3.1 Introduction

Raman scattering of light was first experimentally observed by C.V. Raman in 1928[187] and later by L. Mandelstam.[188] The interaction between low energy monochromatic photon of Laser and atoms of solids results the creation and annihilation of vibration quanta i.e., phonons. In Raman scattering, the interaction of electric field of photon and electron of material results in excitation of electrons in virtual or real electronic states.[189] The perturbation of ionic cores caused by electric field of excited electronic states results in lattice vibrations. Two types of scattering processes take place. The first one is labelled as Rayleigh scattering, in which elastically scattered photons have the same energy as that of incident light. The second one is termed as Raman effect in which inelastic scattering of photons takes place. The scattered photons have either gained or lost the energy as compared to incident photons.

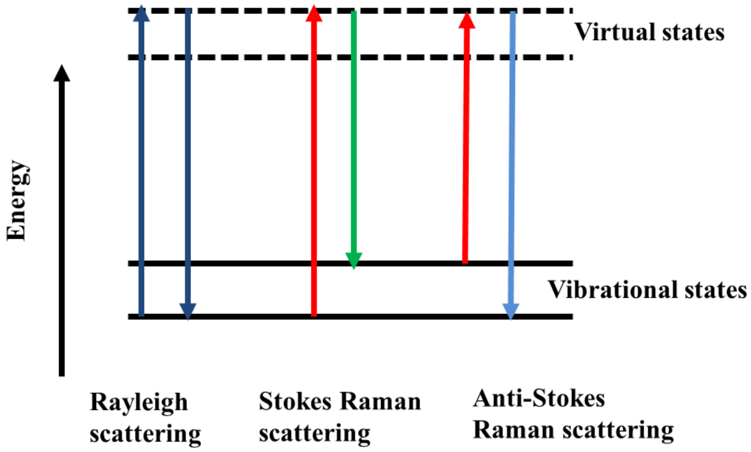

Figure 3. 2 Different scattering incidents between photon and electrons of atoms[189]

If the energy of incident photons is transferred to lattice, the scattered photon will have less energy (the phenomenon is associated with Stokes lines), and if lattice transfers energy to incident photons, the scattered photons have higher energy (anti-Stokes lines). Rayleigh effect is removed by a notch filter in Raman instruments. The energy level diagram that depicts the three processes is shown below (see Figure 3. 2). Here virtual states are short lived electronic states and obey Heisenberg uncertainty principle. Knowledge of phonon dispersion relation of a solid allows to predict its Raman spectra. The ratio between intensity of Stokes and anti-Stokes lines allows to determine the temperature of system.

3.3.2 Raman Spectra of Graphene based Systems- Theoretical Aspects

Raman spectrum provides rich information about carbon based nanostructures. It is considered as finger print technique that gives details about structure and perfection of carbon based nanostructures. The phonon dispersion relation of graphene is foundation to understand Raman spectra of complete range of carbon nanostructures like nano-diamond, fullerenes and CNTs. It also provides fine details to an extent that is helpful to distinguish between monolayer graphene, few-layers graphene and stacked graphene.

Here, the discussion on Raman spectroscopy will be limited to graphene and graphene nanocomposites only. The unit cell of graphene consists of two inequivalent carbon atoms A and B. The in-phase (i) and out-of-phase (o) i.e., (parallel and perpendicular to graphene's plane) vibrations of A and B produce acoustic (A) and optical (O) phonon modes. The vibrations perpendicular and parallel to the plane containing C-C bond of A and B atoms are termed as transverse (T) and longitudinal (L). So altogether, there are six phonon modes labelled as iLO, iLA, iTO, iTA, oTA and oTO.[190] (See Figure 3. 3(a)). Figure 3. 3(b) shows the Raman spectrum of monolayer graphene, which consists of three prominent features i.e., (i) D band, that appears at ca. 1350 cm^{-1}, (ii) G band, that appears at 1582 cm^{-1} and an associated shoulder termed as D' band, and (iii) 2D band also known as G′ band, located at ca. 2672 cm^{-1}.

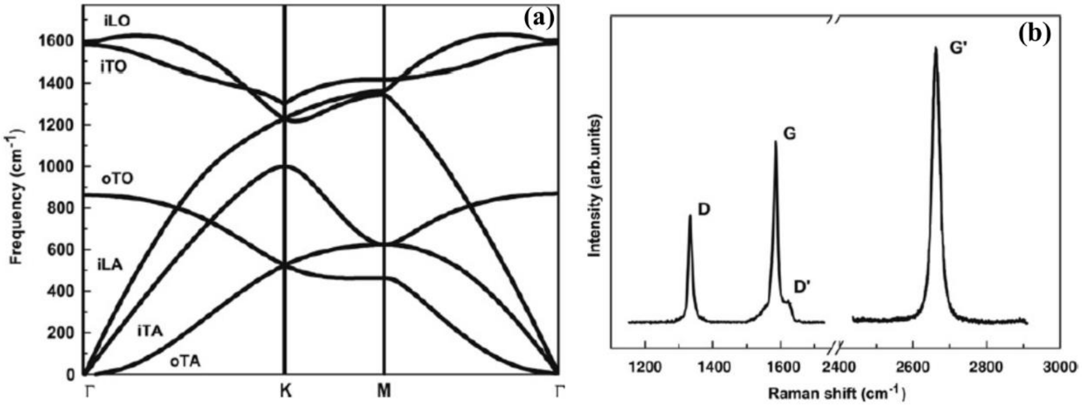

Figure 3. 3 Left panel: Phonon dispersion of graphene, adapted from work of Lazzeri *et. al.*,[191] (a). Right panel: Raman spectrum of monolayer graphene adapted from work of Malard *et. al.*[190] (b).

The fine details of G band provide distinguishing information about graphene, graphite, few layers' graphene and CNTs. It appears because of first order Raman scattering as can be seen in Figure 3. 4(a). The doubly degenerate iTO and LO phonon modes give rise to G band at the Brillouin zone centre (Γ). This band shifts to lower values in case of graphite. Considering doped graphene and graphene nanocomposites, it is important to mention that G band shifts its position to higher values, which indicates the strain in graphene (in case of neat graphene), or a charge transfer between graphene and other species (in case of doped graphene, and graphene nanocomposites). A shoulder (D′ band) that appears next to G band, at *ca*. 1620 cm^{-1}, is due to defects in graphene.

The 2D or G′ band provides details about number of layers in graphene/graphitic samples. It appears due to double resonance Raman process and involves two iTO phonons modes near the Γ point of Brillouin zone. The symmetric and well defined single 2D peak represents monolayer of graphene. However, if the peak seems to be composed of merged peaks, is an indication of increased number of layers in samples.[192]

The D band appears due to defects in graphene. These defects describe the edge termination, dangling bonds of carbon in case of pristine graphene. It is noteworthy that the D band appears at same position on GO, rGO, GNPs and graphene nanocomposites. For GO and rGO, the D band is ascribed to defects that appear on graphene's basal plane and edges due to attachment of functional groups. For graphene nanocomposites, D band appears with pronounced intensity and high area under the curve due to decoration of nanostructures on graphene's surface. Considering the phonon dispersion relation, it is reported that D band appears due to one iTO phonon mode and one defect. A dispersive behaviour is exhibited by D and 2D bands that depends in the energy of incident laser beam.[190] The double resonance process for D and 2D band is explained in Figure 3. 4(b) and (c) respectively.

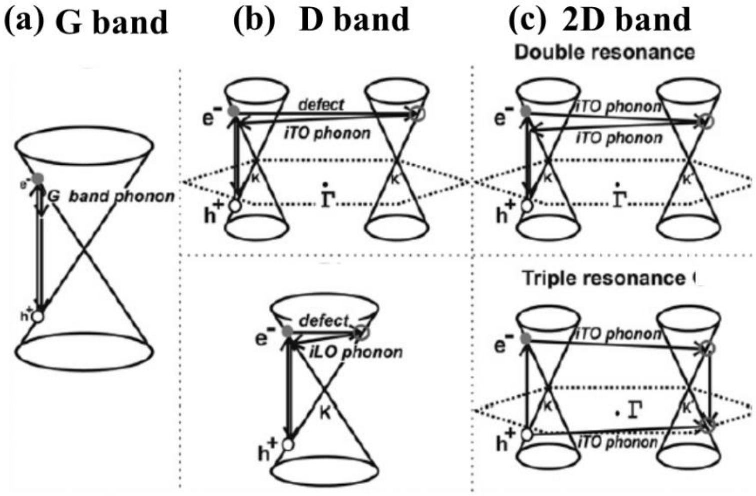

Figure 3. 4 (a) First order Raman scattering for G band, (b) second order Raman scattering giving rise to D band (top), and D' band (bottom), and (c) double resonance (top) and triple resonance (bottom) process for 2D band[190, 193]

Double resonance scattering events taking place in D band is based on excitation of an electron by an incident photon in one valley. This electron gets elastically scattered by a crystal defect to another state in the other valley. This electron returns to original valley via inelastic scattering (by electron-phonon interaction) and refills the original hole and emits the photon. These two events of double resonance process also take place in 2D band, but both events are inelastic and caused by interaction between electron and two phonons (that have equal and opposite wave-vector).

3.3.3 Ramboss Raman and Photoluminescence (PL) Spectrometer

The Raman spectroscopy measurements presented in this thesis were made in Centre of Micro and Nano Devices, Department of Physics, CIIT, Islamabad, Pakistan using Ramboss Raman spectrometer equipped with Ar-ion laser set of excitation wavelength 514 nm (Figure 3. 5). It possesses a neutral density filter to eliminate Rayleigh scattering effect. The laser beam is focussed on sample using microscope installed inside chamber that enables the selection of specific region of sample under view.

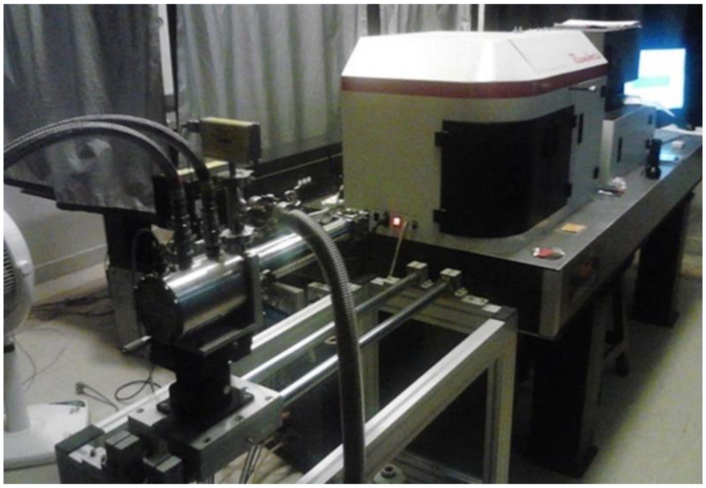

Figure 3. 5 Ramboss Raman and PL spectroscopy system located in CIIT

Before data acquisition, the samples were prepared either in compacted powder form or in pellet form. The pellets were formed using a hydraulic press under 20 MPa pressure for 10 minutes. The pellets were placed on a clean glass slide which were then placed on the stage and laser light was focused on it. The scattered light was then analysed using spectrograph. The layout of a typical Raman spectrometer is depicted in Figure 3. 6 (left panel).

Laser is used as excitation source that provides high intensity, monochromatic and collimated beam of light, which is made to fall on sample's surface. The collimation optics provide a way to enhance the intensity of Raman signals by focusing the beam on sample. Typically, only 1 out of 10^7 photons experience Raman scattering (inelastic scattering). Thus, Raman signal is weak. This can be avoided by use of light focusing lenses. The other way is to use the light that has photons resonant with electronic transitions. This issue can also be addressed using surface enhanced Raman scattering substrate. Collection optics serve to collect the scattered photons.

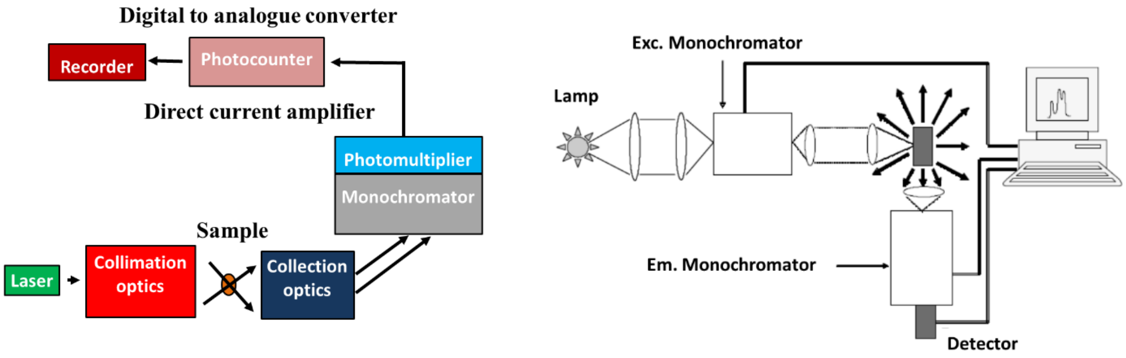

Figure 3. 6 A schematic layout of a typical Raman spectrometer (left panel) and PL spectrometer (right panel)[194]

At this stage, a filter is used to eliminate the Rayleigh scattered signals. Raman signals are then passed through a charged couple device (CCD) detector which records the data as Raman intensity versus wave number (cm^{-1}).

3.3.4 PL Measurements

When a material absorbs light, the emitted intensity is proportional to incident intensity. The two types of spectra are observed called emission spectrum and excitation spectrum. Stoke's shift and anti-Stoke's shift can be observed in atomic and molecular systems. Information about bandgap energy and defects can be obtained from PL spectra of the materials.

The components of a typical PL spectrometer are shown in Figure 3. 6 (right panel). A laser beam is used to generate excitations in the sample. The sample absorbs light. Next to this, a primary monochromator is used to analyse the emitted beams. A focusing lens then collects the emitted light from sample. An emission monochromator is used to collect the radiations. A detector connected to computer detects the signal and data is acquired.

The measurements for this work were made on the samples that were pressed in the form of pellets. The data was acquired using Ramboss Raman and PL spectrometer (see Figure 3. 5). The pellets were mounted on the sample stage and were irradiated with a laser beam that had wavelength 325 nm.

3.4 X-ray Diffraction (XRD)

3.4.1 Introduction

The discovery of X-ray diffraction in 1912[195, 196] has made it a primary method for crystal analysis. XRD is most effective and extensively used experimental technique to investigate crystal structure of nanomaterials and to identify the chemical compounds. There are two types of this method, X-ray powder diffractometry and X-ray diffractometry. However, X-ray powder diffractometry is most widely used technique to investigate all types of crystalline materials. X-ray diffractometry is a photographic technique. Wide angle X-ray diffraction method is used to investigate polymers and glasses.

The high energy electromagnetic radiation, X-rays are produced by collisions of electrons (accelerated under high voltage V) on metal targets. The deceleration of electrons converts kinetic energy of electrons to X-rays energy, whose wavelength is given by,

$$\lambda = \frac{1.2398 \times 10^3}{V}\, nm \tag{3.12}$$

A cooling system provides protection against conversion of kinetic energy of electron into heat. Two types of X-rays are generated in this process, i) continuous X-rays/white X-rays, and ii) characteristic X-rays. Continuous X-rays form the background spectrum. However, X-rays of certain wavelength superimpose the background radiation in a way that an intense maximum is formed. These are known as characteristic X-rays. Monochromatic X-rays are required for X-ray diffraction methods; therefore, these are obtained from characteristic X-rays only by filtering out the continuous X-rays from the spectrum. Inner shell transition of electrons produced by incident electrons generate many of characteristic X-rays on Cu target (normally used in X-rays diffractometers) with certain wavelengths are given by the following equations,

$$\lambda_{K\alpha'} = 0.15406\, nm, \tag{3.13}$$

$$\lambda_{K\alpha''} = 0.15444\, nm, \tag{3.14}$$

$$\lambda_{K\beta} = 0.13922\, nm, \tag{3.15}$$

The inner shell transitions are shown in Figure 3. 7. Among these, only $K_{\alpha\prime}$ radiations are used to examine the samples.

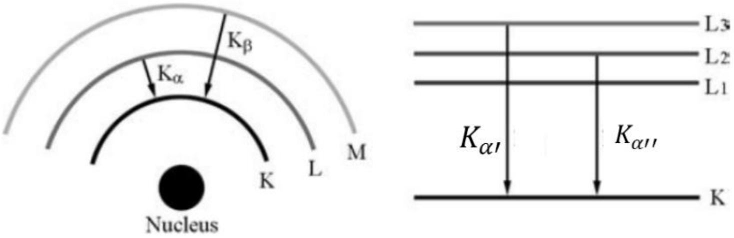

Figure 3. 7 Schematic illustration of generation of characteristic X-rays, adapted from Leng *et. al.*,[197]

The rest of characteristic X-rays and continuous X-rays are filtered out using a mechanism based on absorption edge filtration. For this purpose, such materials are used in X-ray tubes that have good absorption characteristics for X-rays other than $K_{\alpha\prime}$ radiations. The absorption of X-rays is governed by following equation,

$$I_x = I_o e^{-(\frac{\mu}{\rho})\rho x}, \tag{3.16}$$

where μ is linear absorption coefficient, ρ is mass density, I is X-ray intensity, x is thickness of absorption layer, and $\mu\rho^{-1}$ is mass absorption coefficient. Mass absorption coefficient shows sharp jump at certain wavelengths which are required for generation of characteristic X-rays. The mechanism of filtration is based on this feature of absorption edge. Such an absorption material is used for which absorption edge just lies at wavelength slightly smaller than that of $K_{\alpha\prime}$ radiation. The material absorbs K_β, continuous radiations, and those with wavelengths smaller than that of absorption edge. In this way, generation of $K_{\alpha\prime}$ is ensured.

3.4.2 Theoretical Aspects of X-rays Diffraction Method

The wavelength of X-rays is *ca.* 0.1 nm, and is comparable to the crystal dimensions in a system of atoms or molecules. It, therefore becomes possible to treat a crystal as natural diffraction grating to investigate the interference of X-rays incident on a crystal. A diffraction process is explained in the Figure 3. 8, where incident ray falling on the crystal at an angle θ, experiences specular reflection. Different reflected rays interfere constructively or destructively, depending on the path difference of the two beams.

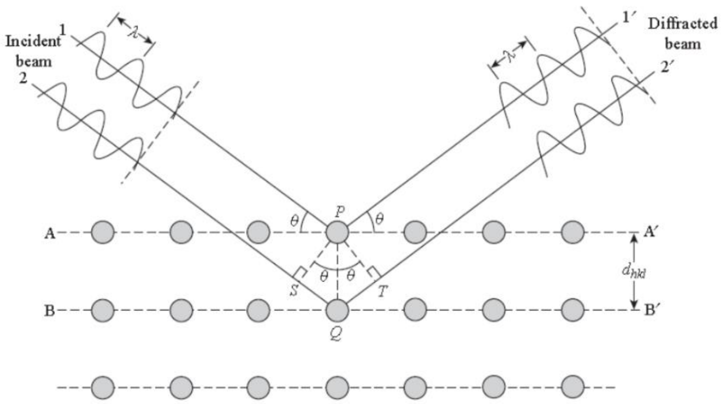

Figure 3. 8 Incident X-rays are reflected from parallel atomic planes following Bragg's law. Adapted from[198]

X-rays following Bragg’s law given by following equation,

$$n\lambda = 2d \sin\theta, \tag{3.17}$$

where, λ is wavelength, n is an integer, and d is distance between atomic planes. Bragg’s law provides the necessary conditions to detect the atomic planes in crystal by diffraction. In reciprocal space, the Bragg’s conditions can be graphically obtained using the Ewald’s sphere. The diffraction intensity is important for detection of diffraction and it depends on a few factors. The collective scattering of all the beams from different atoms determine the diffraction intensity. It is given by following equation,

$$I(2\theta) = \frac{I_o}{r^2} K \frac{1 + cos^2(2\theta)}{2}, \tag{3.18}$$

Here, 2θ is angle between incident beam and scattering direction, I_o is intensity of incident beam, r is distance between electron and detector, and K is constant that depends on atomic properties. The last term is known as polarization factor and depicts the angular dependence of scattered beam. A simple sum of intensities doesn't give the total scattered intensity, instead, atomic form factor is used to describe the scattering intensity of an atom.

3.4.3 PANalytical X'Pert pro X-ray Diffractometer

The X-ray diffraction patterns of samples presented in Chapter 4-7 were obtained using PANalytical X'Pert pro diffractometer (see Figure 3. 9).

Figure 3. 9 PANalytical X'Pert pro diffractometer placed in CIIT, Islamabad.

This instrument is used to acquire X-ray diffraction patterns of powdered samples, compact pellets and thin films on substrates. The typical setup showing components of X-ray diffractometer is shown in Figure 3. 10. The major components are X-ray source, specimen holder and detector. A collimating assembly collimates the X-ray beams generated by X-ray tube. The collimating assembly is composed of Soller slits which are closely spaced metal plates. They serve to prevent the divergence of X-ray beams, which are then focused on the specimen place on specimen table. The X-ray beams are then diffracted from the sample. A convergent beam of X-rays then passes through receiving slits and a monochromatic filter. The filter serves to eliminate the radiations other than $K_{\alpha\prime}$. The filter is usually made of graphite crystal. The filtered beam then finally enters the detector that detects the diffracted X-ray beam.

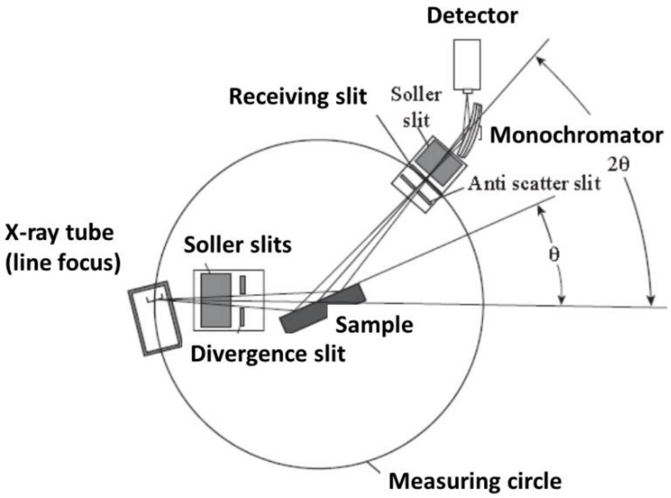

Figure 3. 10 A geometric presentation of components of a typical diffractometer[197]

The acquisition of X-ray intensity is based on relative motion of X-ray tube, specimen, and detector. Commercially available diffractometers usually use Bragg-Brentano arrangement for analysis of powdered samples or pellets. In this kind of arrangement, incident beam is fixed, but the specimen table is rotated around the axis in a perpendicular direction to change the incident angle. The detector also rotates in perpendicular direction. To maintain the angular correlation $(\theta - 2\theta)$, the detector is rotated at a speed which is twice that of specimen's stage.

The data is acquired in the form of variation in intensity as function of 2θ. The preferred 2θ range for graphene and ceramics nanocomposites is between 5°-80°. The intensity peaks located at different 2θ give information of crystalline phase of both graphene and inorganic oxides.

Each peak shows diffraction from specific atomic planes of crystal and has a finite width. The data is acquired at different step widths e.g., 0.02°.

The X-rays diffraction patterns for this thesis were acquired using powdered samples which were first grinded using mortar and pestle. Small amounts of well grinded samples were then placed on cleaned glass substrates, which were then mounted on specimen stage of diffractometer for examination. The substrate's spectrum was subtracted from acquired data. Crystallite sizes using Scherrer's equation, and effect of micro strain on crystallite sizes can also be evaluated indirectly from data acquired using XRD.[199, 200]

3.5 Scanning Electron Microscopy (SEM) Coupled with EDX Analyzer

3.5.1 Introduction

Invention of SEM in 1938[201] followed by further development in the later years[202] has made it an extensively used instrument for imaging surfaces. SEM can provide a detailed and magnified three-dimensional image, whereas a light microscope provides only a planar image. A beam of electron with energy 1-40 KV is used to scan the surface of specimen to get the image with high depth of field, and is of the order of few micrometres at $10^4\times$ magnification. In addition, SEM is usually coupled with EDX analyser, which is an elemental analysis technique and gives the composition of specimen's surface.

3.5.2 Theoretical Aspects and Components of SEM

A typical SEM consists of three major components that include optical arrangement, detector, and probe. There is an electron gun (thermionic or field emission) that is used to produce the accelerated beam of electrons. Field emission gun gives high beam brightness. The emitted beam is condensed in a probe, which is achieved by the optical arrangements. The optical arrangements include a series of apertures and electromagnetic lenses. The beam passes through a pair of condenser lenses and an objective lens (demagnifier lens) to reduce the crossover diameter of electronic beam and its focus on a narrow region of the order of few nanometres respectively. The apertures limit the divergence of electronic beam. The objective lens has an incorporated deflection system (i.e., two pairs of electromagnetic coils called scan coils) which controls the probe to scan the specimen's surface. A graphical presentation of SEM setup is given in Figure 3. 11. The inelastic and elastic scattering events of electrons on specimen's surface produce secondary electrons (SE) and back scattered electrons (BSE) respectively. The signals generated by SE are useful for topographic contrasts, whereas that of BSE are used for formation of elemental composition contrasts.

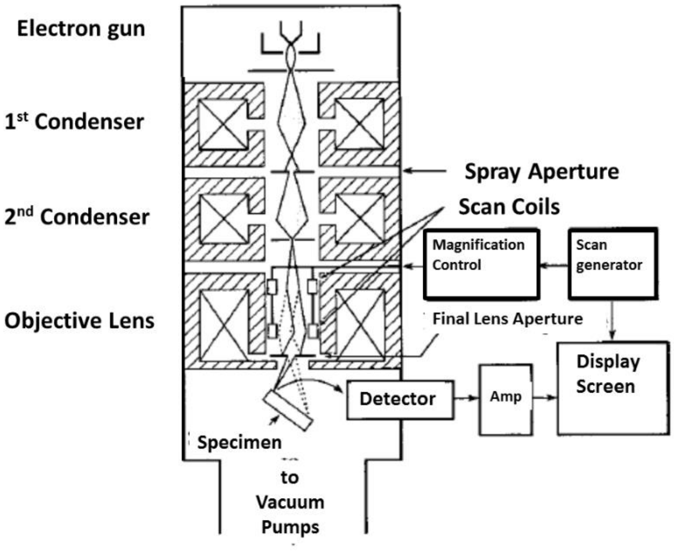

Figure 3. 11 A graphical description of SEM adapted from[203]

Everhart-Thornley (E-T) detector detects signals from both SE and BSE. It is a combination of Faraday-cage, scintillator and photomultiplier tube. Fluctuations of electron beam current and signal amplification of detector are sources of background noise, which can be reduced by digital imaging of signals. Surface charging is produced in case of non-conducting samples due to accumulation of electrons and creates the distortion in image. It can be reduced by coating the specimen with a conducting layer.

A high-resolution image depends on cross-sectional diameter of probe, d_p given by following equation,

$$d_p = \sqrt{\frac{4i_p}{\beta\pi^2\alpha_f^2}}, \tag{3.19}$$

where i_p is the probe current, β is the beam brightness, and α_f is the convergence angle of probe. Brightness of beam is also proportional to accelerating potential of electron beam, i.e.,

$$\beta \propto eV_o , \tag{3.20}$$

where, V_o is the accelerating voltage and e is electronic charge. The magnification in SEM is defined as the ratio of linear size of display screen to the linear size of sample under consideration.

3.5.3 EDX Analyzer

The elements and their quantities present in specimen can be determined by EDX microanalyzer present in SEM. It is a technique that relies on characteristic X-ray detection, emitted by materials that are exposed to accelerated electron. The X-rays are also generated when SE and BSE electrons are produced due to interaction of primary incident electrons and specimen. The generation of X-rays is explained in Figure 3. 12. High energy incident electrons can knockout the electrons from atoms of specimen and atoms will get ionized. The refilling of an inner shell electron by an outer shell electron will produce X-ray photon. The energy of this characteristic X-ray photon depends on the atomic number as given by Mosley's law,

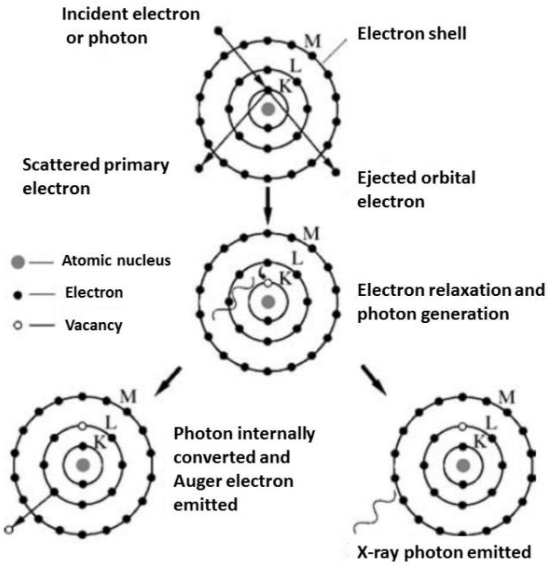

Figure 3. 12 Graphical description for production of X-rays and Auger electron by interaction of electrons and atoms in specimen. The figure is adapted from the work of Leng *et. al.*,[197]

$$\lambda = \frac{B}{(z-\sigma)^2}\,, \tag{3.21}$$

where λ is wavelength of X-ray photons, z is atomic number, σ and B are constants. Allowed electronic transitions between two shells are determined by the selection rules. The emitted X-rays are analysed by their wavelength or energies. The components of EDX microanalyzer are shown in Figure 3. 13.

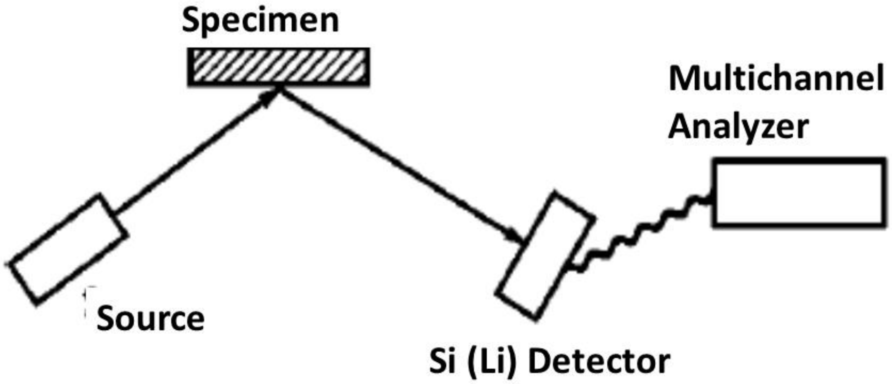

Figure 3. 13 Components of EDX microanalyzer adapted from[197]

The produced X-rays signals are collected by a Si (Li) photo diode. A photon detector detects signals from whole range of elements. EDX work in stationary and scanning mode. The signals are recorded as intensity of characteristic X-rays as a function of energy. Elements are identified in a microscopic volume using software installed.

3.5.4 MIRA3 TESCAN Field Emission Scanning Electron Microscope (FE-SEM)

The FE-SEM images and EDX spectra obtained for neat inorganic oxides and graphene nanocomposites included in thesis were acquired from MIRA3 TESCAN FE-SEM placed at Institute of Space Technology, Islamabad, Pakistan. (see Figure 3. 14)

Figure 3. 14 Scanning electron microscope placed at IST, Islamabad.

To acquire images using FE-SEM, the samples were prepared using specific steps. A carbon tape was used to cover the clean stub. A small amount of finely ground powdered sample was placed over it. The samples were then carbon coated using a sputtering unit, which formed a thin film (a few nm thick) over the specimen’s surface. The coating of conducting material helps to avoid the surface charging effects produced in non-conducting samples during analysis.

3.6 Transmission Electron Microscopy (TEM) and Selected Area Electron Diffraction (SAED)

3.6.1 Introduction

A TEM provides several times higher resolution and magnification than transmission light microscopes, which is due to 10,000 times shorter wavelength of electrons as compared to light. It can operate in different modes which makes it an imaging technique that not only visualizes morphology but also provides crystallographic information (SAED and HR-TEM) about the material under observation, when operated in diffraction mode. It is also used to study the defects in the materials.

3.6.2 Components of TEM

The major components of TEM are electron source, optical assembly, specimen stage, and data acquisition unit. TEM operates under high vacuum. The electron gun can be either thermionic or field emission that generates a beam of electrons with very high energy. Field emission guns are usually preferred because a high intensity (10^4 times higher than tungsten filament) electron beam is obtained. Therefore, the image obtained has a high brightness. A high resolution is determined by wavelength which in turn depends on the high energy of accelerated particles. The electrons are accelerated with voltages greater than 100 KV. The optical path is comprised of two condenser lenses, specimen objective lens, intermediate lens and projector lens.

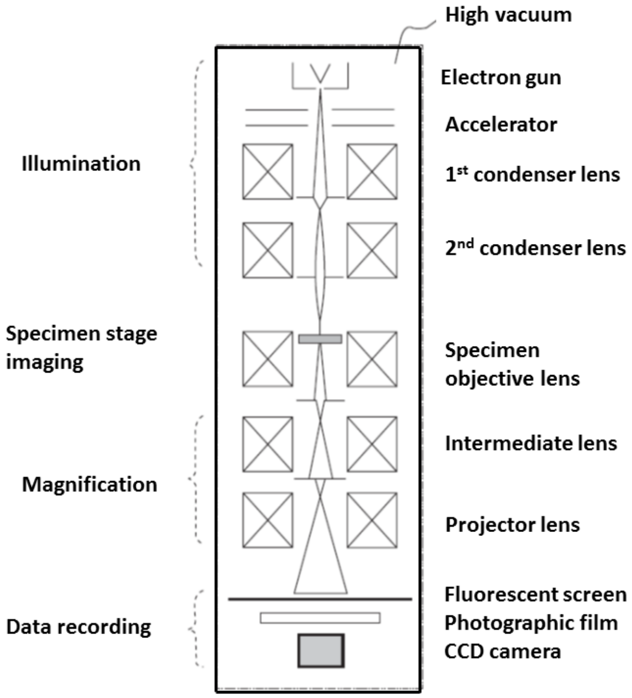

Figure 3. 15 Optical path in TEM adapted from the work of Leng *et. al.*,[197]

Figure 3. 15 depicts the arrangement. Electromagnetic lenses are used to magnify power by controlling the applied current in solenoid. Condenser lens demagnify the electron beam by controlling the beam diameter and its convergence angle. The intermediate lens is used to switch between image mode and diffraction mode. The projector lens is used to further magnify the image and to project the image of diffraction pattern on the screen. The specimen stage is in the form of mesh (3 mm) that can transmit electrons. A Cu mesh coated with thin film of carbon can be used for this purpose.

3.6.3 Image Modes, HR-TEM and SAED

Electron scattering creates image by two types of amplitude contrasts i.e., mass-density contrast and diffraction contrast. The elastic collisions between electron and atomic nuclei results the deflection of electrons. The amount of electron scattered from different points of specimen depend on the mass-density of those points. Thus, there will be a variation in electronic intensity received at TEM detector. Contrast in TEM is defined in terms of primary beam intensity, I_o and transmitted intensity, I_t as

$$C = \frac{I_o - I_t}{I_o}, \tag{3.22}$$

These mass density contrasts lead to image formation in amorphous materials. Whereas, diffraction contrasts are used for image formation in crystalline materials. Electrons satisfy Bragg's law. The objective's aperture allows electron beams diffracted at certain angles only. Consequently, diffraction contrasts result in image formation.

The third type of contrast called phase contrast is associated with phase of electron waves. At least two beams, transmitted and diffracted beam with different phases produce interference pattern that is recorded on screen as a pattern of dark and bright fringes. It shows the periodicity of crystal structure. This is known as high resolution TEM mode (HR-TEM). The spacing between parallel crystal planes and hence (hkl) indexing of planes is possible from micrographs obtained using HR-TEM.

A change in optical path of electronic beam allows the operation of TEM in image and diffraction modes. If intermediate lens is focused on image plane, TEM works in image mode. A diffraction mode is achieved when intermediate lens is focussed on back focal plane of objective lens. The micro-structural images of samples are obtained in image mode, whereas, the diffraction pattern as the plane of reciprocal lattice is obtained in diffraction mode and it is known as selected area electron diffraction (SAED). SAED provides complementary information about the crystal planes in reciprocal lattice of specimen. Images with diffraction spots (reciprocal lattice points) for single crystal and circular rings for crystals oriented in different directions are obtained.

3.6.4 JEOL-2100F FEG TEM

The TEM images, SAED patterns and HR-TEM images were acquired using JEOL-2100 FEG TEM placed in Department of Physics at Durham University, UK. (See Figure 3. 16). To get the images, specific methods are required for sample preparation.

Figure 3. 16 Transmission electron microscope placed at Durham University, UK.

The thinning of powdered samples was acquired by dispersing the powdered samples in appropriate amount of deionized water and sonicating the solution for some time. The drop of this solution was poured on TEM grid, which was then placed on the specimen's stage to acquire required images. TEM images give the morphology of samples. A particle size distribution can be obtained using TEM images. HR-TEM images give information about spacing between two atomic parallel planes of crystal. SAED patterns help to identify crystal planes of samples.

3.7 Vibrating Sample Magnetometry (VSM)

A very simple instrument VSM is used to measure the magnetic dipole moment, saturation magnetization and coercivity of bulk, thin films and nanomaterials. Foner in 1956 proposed a very simple and inexpensive design of this instrument.[204] A number of variants were suggested to the basic design in later years.[205] A VSM can detect magnetic susceptibility up to 10^{-8} emu/g.

3.7.1 Working and Components of Vibrating Sample Magnetometer

The components of VSM are presented in the following Figure 3. 17. The major components that are needed for working of VSM are i) a vibrating assembly in which sample is fixed at the time of measurement, ii) an electromagnet that is used as source of magnetic field and makes vibrating assembly vibrate, iii) a bipolar power supply that is used to generate current and it is interfaced with DC source, iv) a lock-in amplifier that serves to induce voltage in pickup coils, iv) auxiliary signal source, that is used to drive the vibration amplitude, v) a field sensing system, vi) a temperature control system, and vii) a computer to control measurements.

The sample placed in vibrating assembly is so adjusted that it lies in a region of uniform magnetic field. It is very fundamental requirement that vibrating rod executes vibration with uniform frequency and amplitude. A magnetic field that varies with time is applied on vibrating sample, thus the voltage induced in pickup coils is detected and further processed to determine the magnetic moment of the sample.

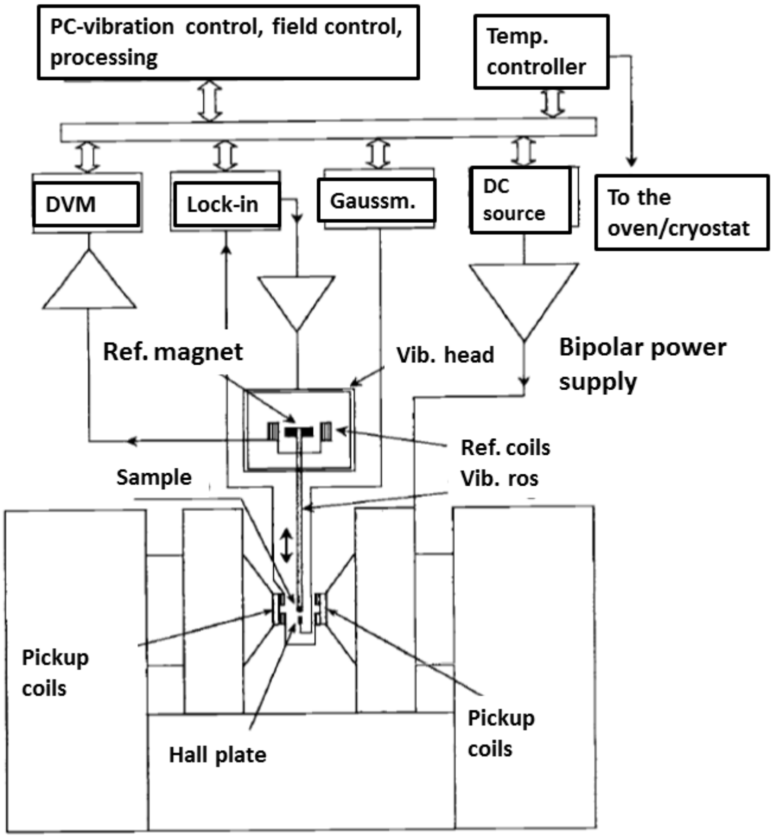

Figure 3. 17 The typical components of a VSM. Adapted from[206]

3.7.2 7407 VSM Lake Shore

The magnetic measurements of magnetic nanocomposites that are included in this thesis were made using 7407 VSM (Lake shore) placed at Centre of Excellence in Solid State Physics, University of the Punjab, Lahore, Pakistan. (See Figure 3. 18)

To acquire data, powdered samples were compacted in the form of a small square pellet and were weighed. Then the samples were placed inside the vibrating sample holder that lies in the middle of poles of electromagnet and the data was acquired.

Figure 3. 18 7400 series VSM (Lake Shore)

3.8 Fourier Transform Infrared (FTIR) Spectroscopy

Energy of infrared waves having same values as that of vibrational energies of sample molecules give an advantage of absorption of IR waves upon interaction with molecule and is fundamental principle of vibrational spectroscopy.

Molecules of solid are always in vibrational motion executing simple harmonic motion with energy,

$$E_{vib} = \hbar\nu_{vib}\left(\upsilon + \frac{1}{2}\right), \qquad \upsilon = 0, 1, 2 \ldots.. \tag{3.23}$$

υ is vibrational quantum number. Energy of molecular vibrations can increase with $\Delta\upsilon = +1$. The normal modes of vibration can have symmetric, torsion, in planar and out of planar bending vibrations. Among these, IR active modes must involve alteration of dipole moment. Mathematically, it can be expressed as,

$$\left(\frac{\partial\mu}{\partial q}\right)_{q=0} \neq 0, \tag{3.24}$$

Where, μ is dipole moment, q is magnitude of normal vibration.

The FTIR spectrometer is comprised of source of IR waves, Michelson interferometer as the key component, detector, and a computer equipped with fast Fourier transform algorithm. The components are shown graphically in Figure 3. 19. The beam splitter in interferometer transmit half of IR beam, and reflects the other half. Later, the transmitted and reflected beams are directed to fixed and moving mirror respectively. These two beams then recombine at beam splitter and are made to fall on the sample. The information from IR active modes is received at detector. The interferogram received at detector is converted to IR spectrum (intensity versus wavenumber curve) by a fast Fourier transform algorithm on attached computer.

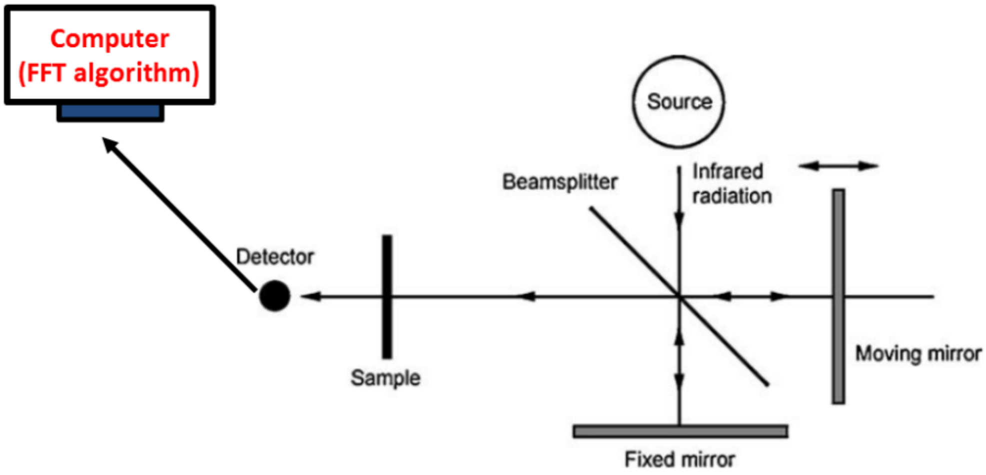

Figure 3. 19 Components of FTIR spectrometer, adapted from the work of Leng *et. al.*,[197]

3.8.1 Shimadzu IR Tracer-100

FTIR spectroscopic data was acquired using Shimadzu IR Tracer-100 placed at Department of Physics, International Islamic University, Islamabad, Pakistan. (See Figure 3. 20). The samples for acquiring FTIR spectroscopic data were prepared by KBr pellet method. The powdered samples were diluted by addition of KBr. The mixture was then grinded and was pressed into pellets using a hydraulic press. The pellets so obtained were mounted on sample holder and were irradiated with IR waves and spectra were obtained from 400-4000 cm^{-1}.

Figure 3. 20 Shimadzu IR Tracer-100 at Department of Physics, IIU.

3.9 Applications-Photocatalytic Activity

The experimental procedures that were followed to evaluate the photocatalytic activity of graphene based nanocomposites (included in this work) are described below.

3.9.1 Photocatalytic Chamber

The photocatalytic (UV assisted) experiments were performed in a home-made chamber that was equipped with 90 Watt, type-c UV lamp (with wavelength, 100 nm- 280 nm). The adsorption-desorption equilibrium experiments were performed in the same chamber without illumination of light. The periodically collected aliquots were analysed for absorption using UV-vis spectrophotometer described in Section 3.11.

3.9.2 Photocatalytic Experiment of MgO and GNPs Nanocomposites

In each experiment, 40 mg of each sample was dispersed in 100 ml of $1.5 \times 10^{-5} M (5\ ppm)$ methyl orange aqueous solution. The experiment was done without altering the natural pH of the system. The solution was magnetically stirred in dark to achieve an adsorption-desorption equilibrium. Thereafter, the solution was exposed to UV light in a photocatalytic chamber and 4 ml of the exposed solution was collected at regular intervals of 30 min. The collected samples were centrifuged to remove the photocatalysts.

3.9.3 Photocatalytic Experiment of Graphene/SiO$_2$ Nanocomposites

A textile dye, methyl orange was selected as a model pollutant to check the photocatalytic performance of graphene/SiO$_2$ nanocomposites. 0.03g of each photocatalyst was added to 100 ml of $1.5 \times 10^{-5} M (5\ ppm)$ aqueous methyl orange solution. The pH of the solution was adjusted to 3 using 1 M HNO$_3$ (1 M NH$_3$). 100 ml of each solution was subjected to the experiment. After establishing the adsorption-desorption equilibrium between the photocatalyst and methyl orange, the solution was exposed to the UV light source. 4 ml of each sample was withdrawn at regular intervals from all the solutions. The samples of the experimented solutions were centrifuged. The collected samples were analysed for absorbance immediately after centrifugation. Each experiment was repeated three times to ensure the accuracy of results.

3.9.4 Photocatalytic Experiment of Graphene/Fe$_3$O$_4$ Nanocomposites

The photo induced Fenton like reaction of prepared samples was evaluated in a photocatalytic chamber for the degradation of methyl orange. $0.2\ g/L$ of each photocatalyst was added to $20\ mg/L$ $(20\ ppm)$ of methyl orange solution. 1M HCl was used to adjust the pH of solution to 3. Later, $1\ ml$ of H$_2$O$_2$ was added to above solution. Adsorption-desorption equilibrium was achieved by stirring 100 ml of solution for 30 min in dark. The solution was then exposed to UV light. To monitor the time evolution of concentration of dye, $4\ ml$ aliquots were collected at regular intervals. The photocatalyst was removed by centrifugation, and the absorbance spectra were recorded. Data reproducibility was ensured by repeating experiments three times

3.9.5 Photocatalytic Experiment of Graphene/NiO Nanocomposites

The photo induced photocatalytic reaction of prepared samples was evaluated on a bright sunny day between 10.00 to 14.00 hours for the degradation of methyl orange.$0.2\ g/L$ of each photocatalyst was added to $20\ mg/L\ (20\ ppm)$ aqueous solution of methyl orange. 1M HCl was used to adjust the pH of solution to 3. Adsorption-desorption equilibrium was achieved by stirring 100 ml of prepared solutions in the dark prior to its exposure to solar light. Time evolution of dye concentration was recorded by collecting 4 ml aliquots at regular intervals (after removing photocatalyst by centrifugation). Each experiment was repeated three times to ensure data reproducibility.

3.10 Application to Antibacterial Activity

A uniform protocol was followed to evaluate the antibacterial performance of all the samples considered in this work. Briefly the test samples (neat metal/non-metal oxides and graphene nanocomposites) were mixed and sonicated in sterile water at a fixed concentration $10\ mg/ml$. The 200 μl of the test sample was added to 5 ml Luria-Bertani (LB) medium. 100 μl of the inoculum (bacterial culture in LB) was added to the above modified growth medium. The inoculated media containing the test sample was incubated at 37^{o}C for 24 h.

3.11 UV-vis Spectroscopy

3.11.1 Introduction

Quantitative foundation of taking measurements from UV-vis spectroscopy was laid in 1852.[207] This spectroscopy is used to investigate the interaction of electromagnetic radiation with liquids. This technique is widely used to investigate chemical reactions, chemical equilibria, and liquids. Optically linear liquids obey an intensity law called Beer-Lambert law, which states that light is exponentially attenuated by medium. This is depicted by following equations,

$$dI/dx = -\alpha I, \tag{3.25}$$

$$I = I_o e^{-i\alpha(\lambda)d}, \tag{3.26}$$

where I_o is the intensity of incident light, d is the thickness of sample, λ is the wavelength of incident light, and α is a linear absorption coefficient.

The UV-vis wavelength range lies between 10 nm to 780 nm. In UV-vis spectrophotometry, the effect of interaction between UV-vis light and matter is studied that involves three processes, transmission, absorption and reflection. Absorbance (or optical density), the logarithmic damping of light is mathematically expressed as,

$$A = log_{10}\left(\frac{1}{T}\right), \tag{3.27}$$

where transmittance T is the ratio of transmitted intensity to incident intensity i.e.,

$$T = {}^{I}\!/_{I_o}. \tag{3.28}$$

The major components of UV-vis spectrophotometer are light sources, wavelength selection components, polarizers and detectors. A double beam spectrophotometer is generally used. It consists of two light sources i.e., deuterium lamp and halogen lamp so that the light can have both UV and visible wavelengths respectively. Stray light is eliminated using monochromator. Monochromators allow the selection of bandwidth and wavelength of transmitted light. A rotating mirror is used to select the light source. A filter is used to stop the propagation of heat as it cuts-off certain wavelengths like IR wavelengths etc. A perforated rotating mirror splits the incident light into two beams, reference beam and sample beam. The beams are then made to fall on sample in a sample chamber, and later photomultiplier tubes. Incident light is absorbed by a sample and a signal is then detected by a detector. A detector with high signal to noise ratio is preferred. Photodiodes or photomultiplier's tubes are used as detectors. The signal is then converted to give transmittance or absorbance value. Figure 3. 21 describes the components of a UV-vis spectrophotometer.

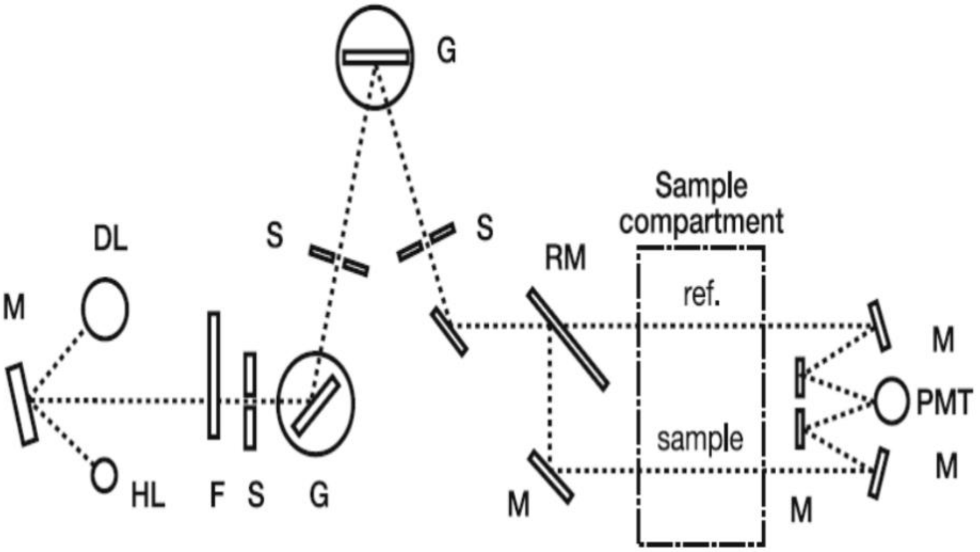

Figure 3. 21 A double beam UV-vis spectrophotometer. HL=halogen lamp, DL= deuterium lamp, M=mirror, RM= rotating mirror, F=filter, S=slit, G=grating, and PM=photomultiplier tube. The dotted lines show the optical path.[208]

3.11.2 Shimadzu Pharmaspec-1700 UV-vis Spectrophotometer

The optical study and absorbance data of aqueous solutions of dye was recorded using Shimadzu Pharmaspec-1700 and Perkin Elmer (Lambda 25 UV) UV-vis spectrophotometers (300 nm-1000 nm) placed at Department of Chemistry, Quaid-i-Azam University, Islamabad, Pakistan. (Figure 3. 22)

Figure 3. 22 Shimadzu Pharmaspec-1700 UV-vis spectrophotometer at Quaid i Azam University, Islamabad.

For optical study, the samples were prepared by sonicating some quantity of powdered samples in deionized water for some time so that the aqueous solution remains nearly transparent. Glass cuvette ($d = 1\ cm$) was used as sample holder to record absorbance. The absorbance of solvent (deionized water in this case) was recorded first. It was used to subtract the baseline from sample's absorbance data. For photocatalytic study, the absorbance of dye solutions was recorded and their concentration was calculated using Beer Lambert law. For low concentration dye solutions, absolute absorbance was recorded, however, concentrated solutions were diluted before recording their absorbance and relative absorbance data was obtained.

3.11.3 UV-vis Scanning Spectrophotometer (UVD-2950)

To monitor growth profiles of bacteria at different time intervals i.e., from 2 h to 24 h, a double beam UV-vis scanning spectrophotometer (UVD-2950) placed at Institute of Biomedical and Genetic Engineering, Islamabad, Pakistan, was used. It is a double beam spectrophotometer that has two light sources, deuterium lamp and halogen tungsten lamp.

Growth profiles of bacteria were obtained by recording optical density OD of bacterial culture at 600 nm. Optical density is basically logarithmic transmittance which can be expressed mathematically as,

$$OD = log_{10}\left(\frac{1}{T}\right) \tag{3.29}$$

Chapter No. 04

4. Synthesis, Characterization and Applications of MgO/Graphene Nanoplatelets Nanocomposites

Overview:

In this chapter the physio-chemical characterizations, photocatalytic and antibacterial properties of MgO nanohexagons and graphene nanoplatelets (GNPs) nanocomposites are presented. The crystallinity, phase, morphology, chemical bonding, and vibrational modes of prepared nanomaterials are studied. The conducting nature of GNPs is tailored via photocatalysis and enhanced antibacterial activity. MgO/GNPs 25% nanocomposite may have potential applications in waste water treatment and nanomedicine due to its multifunctionality.

4.1 Introduction

Due to rapid industrial growth, there is constant confrontation of contaminated natural resources like water. At the same time health risks posed by pathogenic bacteria need to be controlled by novel methods other than traditional antibiotics. Material scientists are in continuous effort to present solutions to health hazards created by synthetic dyes and bacterial contaminated water. Multifunctional nanomaterials are therefore, of extreme importance in the modern era of industrialization. Recently metal oxides (with or without chemical modification) are vastly researched for the photocatalytic applications i.e., to address water splitting and dye contaminated water remediation.[209-213] Magnesium oxide (MgO) has been focus of research both from theoretical and experimental point of view since decades.[214-218] Different nanoscale morphology based applications of MgO make it an important ceramic material. It has been used as a nanothermometer (Ga filled MgO nanotubes),[219] antibacterial agent,[220-222] substrate for high T_c superconducting materials (HTSC), passive layer for high mobility transistors[223] and an excellent dielectric material.[224] The bandgap energy of nanoscale MgO, being an insulator is high i.e., ≥ 5eV which drags attention towards making it optically active for applications like photo catalysis. Its surface modification is highly desirable to make its efficient use in adsorption of dyes, photo-oxidation catalysis (for waste water cleaning) and solar cells.[225-227] Interestingly the same material MgO, being biosafe for healthy human cells and toxic for bacteria[221, 228] provides a platform to further investigate its toxicity to pathogenic bacteria. The bare MgO shows negligibly low photocatalytic activity due to its large bandgap energy and the quick recombination of charge carriers. This problem can be addressed by introducing an electron acceptor material with MgO. In this regard carbon nanostructures are an attractive choice. To tailor above mentioned features and applications in single material, we have combined MgO with graphene nanoplatelets (GNPs) (i.e., an insulating and a conducting phase) in this work.

MgO, $Mg(OH)_2$ and graphene family nanocomposites have been of very recent interest for researchers. There have been recent reports depicting nanocomposites as heat transfer efficient materials and adsorbents of organic dyes etc.[229, 230] These few reports have covered only limited physical and chemical aspects of MgO and graphene family nanocomposites. There is much potential in the area for the future work. There is need to ponder over various aspects of MgO/GNPs nanocomposites to further throw light on those properties which haven't been researched yet. This work is focused to achieve high photocatalytic activity of MgO/GNPs as compared to MgO. In parallel, this study presents a comprehensive analysis of antibacterial efficiency of MgO/GNPs nanocomposites. To the best of our knowledge, here we report for the first time, the impact of MgO/GNPs nanocomposites on photodegradation of methyl orange. Moreover, the present report is the first article on GNPs loading dependent antibacterial properties of MgO/GNPs nanocomposites.

4.2 Results and Discussion

4.2.1 Structural and Morphological Analysis

The crystalline nature and phase purity of pristine MgO and MgO/GNPs nanocomposites were analysed in the range of $20^o – 80^o$ using XRD. The diffractograms are depicted in Figure 4. 1. The sample MgO, showed peaks located at 36.9^o (111), 42.7^o (200), 61.9^o (220), 74.5^o (311), 78.5^o (222). All these peaks can be indexed to single phase cubic crystalline MgO structure and perfectly match with JCPDS-00-043-1022, with lattice parameters $a = b = c = 4.2130$ Å, and $\alpha = \beta = \gamma = 90^o$. No peak related to $Mg(OH)_2$ phase is observed. The X-ray diffractograms of

MgO/GNPs with two different concentrations of GNPs shows all the peaks of cubic MgO phase along with the small diffraction peak at 2θ = 26.4°. This peak is the manifestation of C (002) plane contributed by the graphitic matrix. Thus, X-ray diffractograms confirm the formation of multiphase MgO/GNPs nanocomposites. The X-ray diffractograms agree with previous reports.[231, 232] The crystallite sizes were calculated using Scherrer's formula. The crystallite size of MgO, MgO/GNPs 12% nanocomposite, and MgO/GNPs 25% nanocomposite is 32 ± 1.3 nm, 30 ± 0.3 nm, and 31 ± 0.5 nm respectively. The peak broadening in MgO/GNP 12% is associated with larger crystallite size due to presence of graphene.

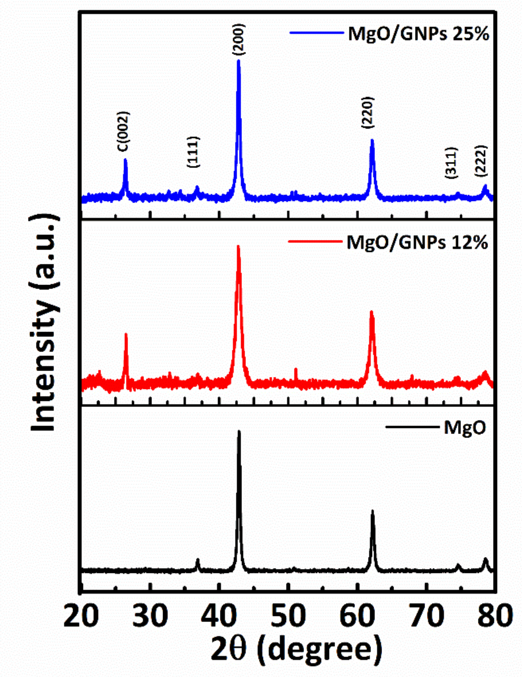

Figure 4. 1 X-ray diffractograms describing the crystalline phase of MgO and MgO/GNPs nanocomposites

To investigate the morphology of MgO/GNPs nanocomposites FE-SEM and TEM analysis was conducted. The images reveal the multiphase nature of material by formation of MgO nanohexagons on graphene nanoplatelets. The Figure 4. 2(a) establishes that MgO is mainly composed of MgO units which have the morphology of lamellar to hexagons with variable edge lengths as labelled in Figure 4. 2(a). Figure 4. 2(b) and (c) represent the microstructure of MgO/GNPs nanocomposite with 25% GNPs loading. MgO nanohexagons seem to be embedded on GNPs. MgO nanohexagons with the edge lengths in the range of 121 nm-190 nm can be

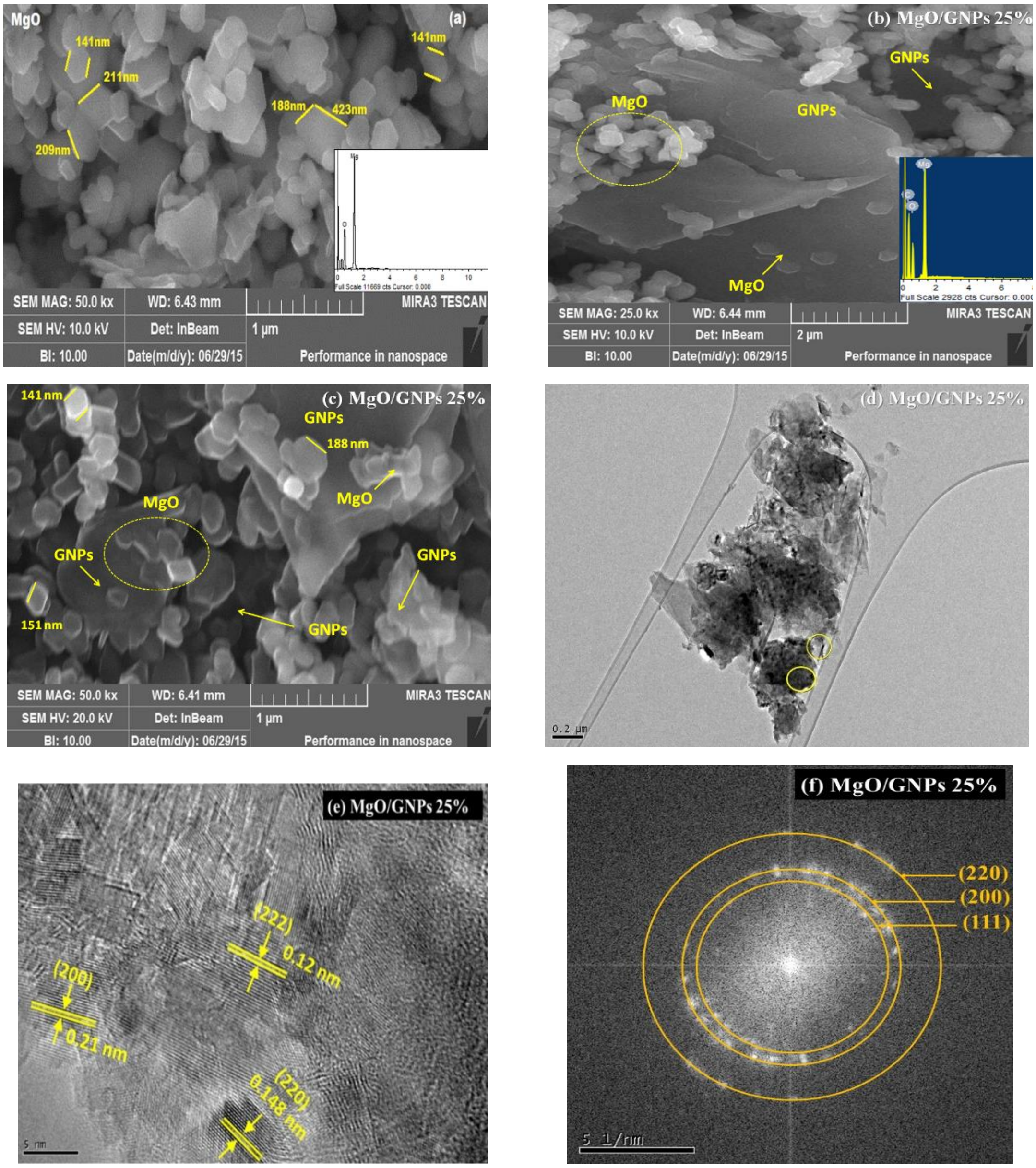

Figure 4. 2(a)-(h) SEM micrographs of (a) MgO, (b), (c) MgO/GNPs 25% nanocomposites. Insets are the EDX spectra. (d)TEM image of MgO/GNPs 25%, (e) HR-TEM image of MgO/GNPs 25%, and (f) SAED pattern of MgO/GNPs 25% nanocomposite.

observed on graphene nanoplatelets. This assembly confirms the multiphase nature of nanocomposites material. It is very interesting to note that on the inclusion of graphene nanoplatelets the edge length of MgO nanohexagons reduces significantly as compared to pristine MgO. The insets in Figure 4. 2 present the EDX spectra of MgO and MgO/GNPs 25% nanocomposites and confirm the elemental composition of prepared samples. The presence of Mg, O and C confirms the formation of MgO/GNPs nanocomposite. The TEM image shown in the Figure 4. 2(d) further verifies the multiphase nature of MgO/GNPs 25% nanocomposite, as both nanohexagons and graphene are visible in the TEM image. The HRTEM images are presented in the Figure 4. 2(e). These images show the crystalline nature of MgO and agree with the results obtained from X-ray diffraction patterns. The crystallite size is 31 nm, which is in close agreement with the XRD results. The HR-TEM image presented in the Figure 4. 2(e) clearly shows the interface between graphene sheets and MgO. It confirms the successful coupling between MgO and graphene sheets. A SAED pattern of MgO/GNPs 25% nanocomposite is demonstrated in Figure 4. 2(f).

4.2.2 Raman Spectroscopic Analysis

Raman analysis is of utmost importance for the analysis of graphene based systems as it gives information about quality of graphene and direct evidence of formation of its nanocomposites with the other species. The Raman spectra of MgO/GNPs nanocomposites are presented in the range of 1200 cm^{-1} to 1700 cm^{-1} as shown in Figure 4. 3. The characteristic bands of graphene nanoplatelets are first order scattering bands i.e., defect band (D-band) and G-band. The D-band is induced by the disorder present on sp^2 hybridized planar structure of graphene. It is primarily activated in the presence of lattice defects, doping and covalent attachments in the form of functionalization or other atoms.[233] The doubly degenerate E_{2g} mode (G-band) appears due to first order scattering at ~ 1587 cm^{-1}. The D-band of GNPs is located at ~ 1350 cm^{-1}. In MgO/GNPs 12% and 25% nanocomposites, the G-band exhibits shift to higher value by 19 cm^{-1}, i.e., to 1606 cm^{-1}. This shift is associated with charge transfer between MgO and GNPs, and is responsible for the formation of nanocomposites.[234] The D-band in MgO/GNPs 12% and 25% have become broader and an increase in its intensity is observed as compared to bare GNPs. This is due to the incorporation of MgO on the surface of GNPs. The intensity ratio between D-band and G-band i.e., I_D/I_G for GNPs is 0.73. It is increased to 0.941, and 0.953 for MgO/GNPs 12% and MgO/GNPs 25% nanocomposites respectively. The D band is broadened due to incorporation of MgO nanohexagons on the surface of GNPs.

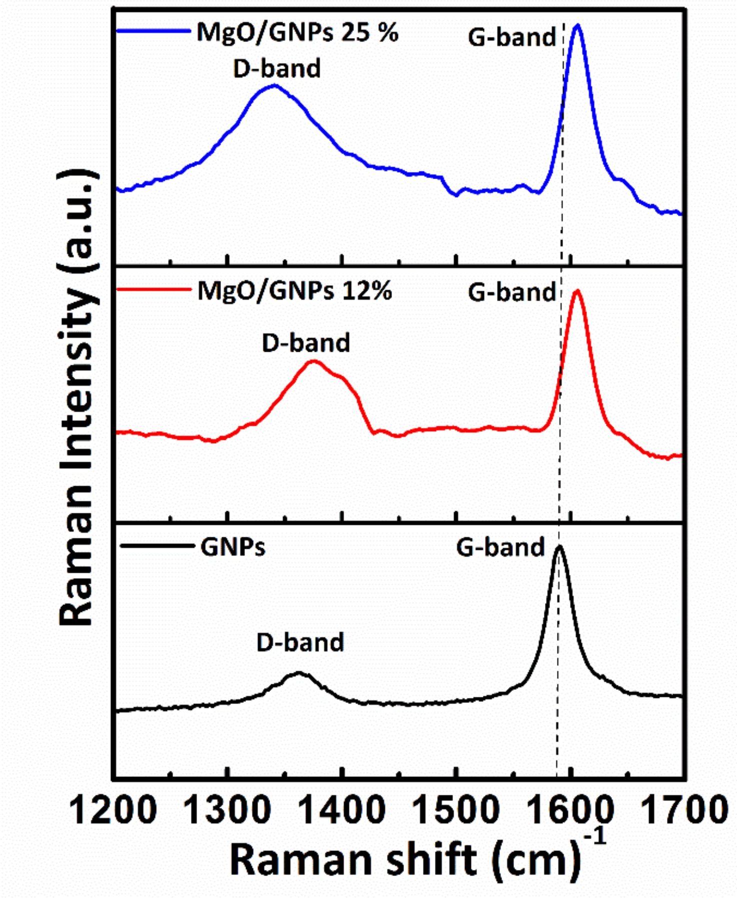

Figure 4. 3 Raman analysis of GNPs, MgO/GNPs 12%, and MgO/GNPs 25%

On the basis of Raman analysis, the incorporation of MgO with GNPs in the form of nanocomposites material can be speculated. The G-band shift and the increased I_D/I_G values indicate the formation of nanocomposites.

4.2.3 Photocatalytic Activity

The photocatalytic activity of the synthesized samples, i.e., MgO/GNPs nanocomposites and bare MgO is investigated for an industrial dye methyl orange as water contaminant. All the samples were stirred in dark for 120 minutes and adsorption-desorption equilibrium was achieved in 30 minutes as presented in Figure S 4. 2.

The UV-visible absorption spectra for methyl orange solution under UV light irradiation in the presence of photocatalysts are shown in Figure 4. 4(a)-(c). The absorbance of methyl orange showed decreasing trend with the increase in irradiation time. The photocatalysts MgO and MgO/GNPs 12% nanocomposite photodegrade 43% and 44% dye respectively in 120 minutes. The methyl orange is degraded to 97.23% in the presence of MgO/GNPs 25% nanocomposite in the same time.

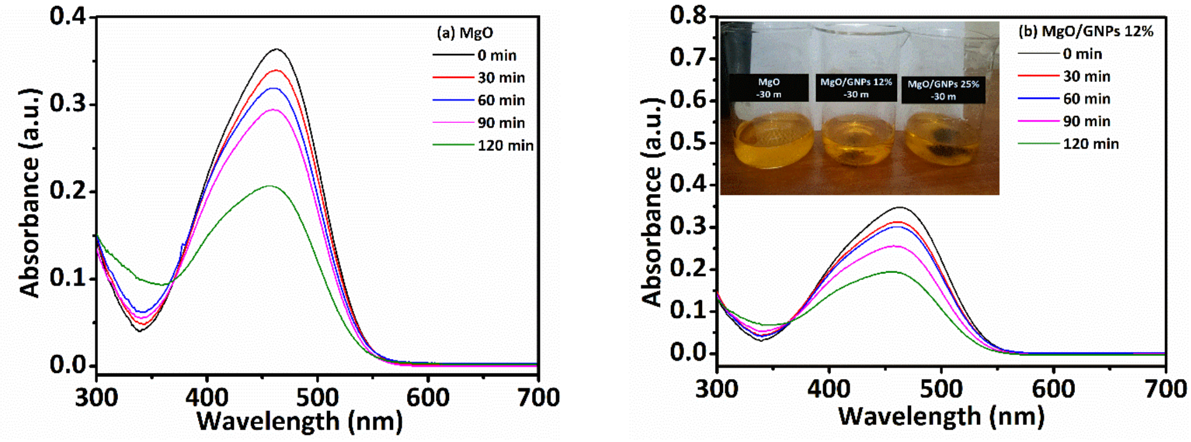

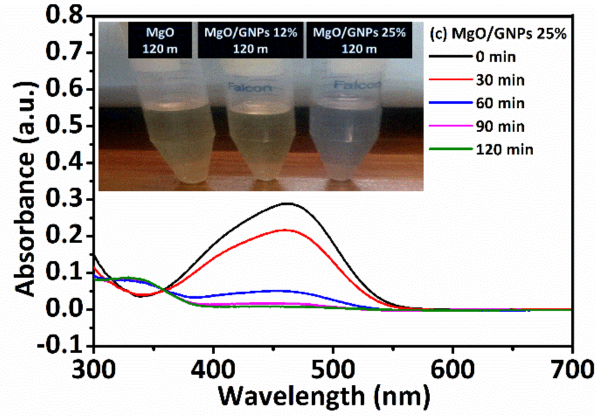

Figure 4. 4 Time evolution of absorbance spectra of methyl orange in the presence of various photocatalysts.

The % degradation efficiencies are calculated using the expression,

$$\%\ degradation\ efficiency = 1 - \left(\frac{C_t}{C_o}\right) \times 100, \tag{4.1}$$

Where C_o is the initial concentration of aqueous solution of methyl orange and C_t is its concentration at different time intervals and C_t and C_o are determined by using Beer-Lambert's law. The photocatalytic degradation of methyl orange in the presence of MgO and MgO/GNPs nanocomposites under UV light irradiation is shown in Figure 4. 5.

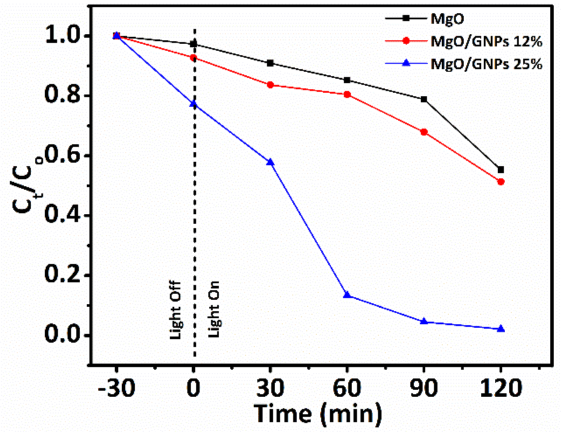

Figure 4. 5 Photodegradation curves of MgO and MgO/GNPs nanocomposites.

The mechanism for the degradation of methyl orange is proposed in Figure 4. 6. The molecules of methyl orange can be transferred to the surface of the photocatalysts (i.e., by adsorption process). After the UV light illumination, the valence electrons of MgO may be excited to its conduction band. As graphene family materials possess excellent electrical conductivity, therefore these electrons are ultimately accepted by adjacent GNPs network. Parallel to this an increase in the number of holes is also observed. As GNPs are the good acceptors of electrons, so the conductive network of GNPs retains the charge carriers ultimately delaying the recombination of e^-_{CB} - h^+_{VB} pairs. The increase in the number of holes and electrons initiate the generation of reactive oxygen species (ROS). It is well established in the previous literature that the holes produced in the valence band react with chemisorbed water to produce ·OH radicals.[235-237] These radicals successively attack the methyl orange. It results into the oxidation of adsorbed dye by producing various intermediates.

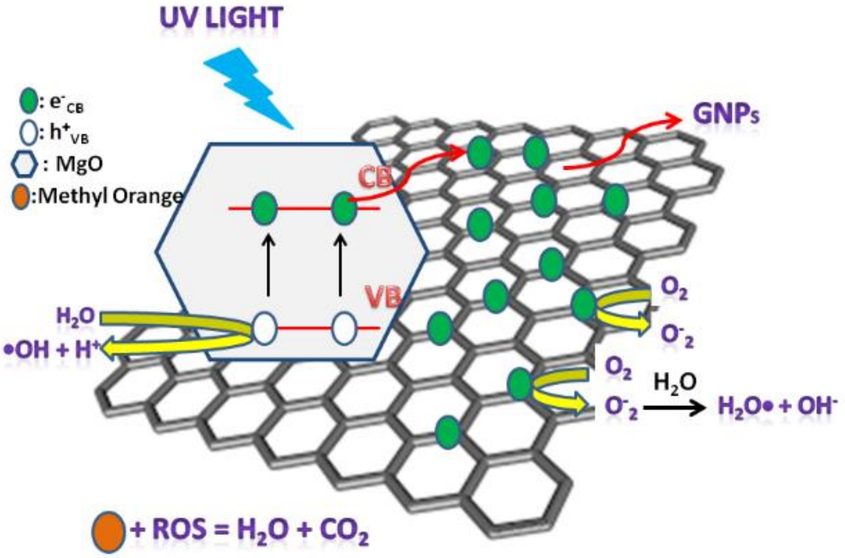

Figure 4. 6 Schematic presentation of the photocatalytic activity of MgO/GNPs nanocomposites.

The intermediates are then converted to CO_2, H_2O as explained step by step in Figure 4. 7. It leads to the complete degradation of methyl orange. The suggested mechanism depicting the formation of intermediates is already proven with evidences in previous studies.[238, 239] The MgO/GNPs nanocomposites show better photocatalytic activity than bare MgO. The importance of optimum percentage of GNPs in nanocomposite is exhibited by the excellent enhancement in photocatalytic activity of MgO/GNPs 25% nanocomposite. From these observations, the highest photocatalytic activity associated with maximum GNPs content is attributed to the effective electron transfer from the conduction band of MgO to GNPs. This transfer reduces the recombination of photo-generated e^-_{CB} - h^+_{VB} pairs. The steady state photoluminescence analysis was conducted for MgO and MgO/GNPs 25% nanocomposite to examine the charge carrier trapping and recombination process. The generation and separation of the charge carriers is the key factor that influences the photocatalytic response of MgO and MgO/GNPs nanocomposite. The photoluminescence intensity indicates the recombination of charge carriers.

The photocatalytic process can be explained by following reactions.

$$MgO - GNPs \ + \ h\nu \rightarrow MgO(h^+_{VB}) - GNPs(e^-_{CB}) \tag{4.2}$$

$$MgO(h^+_{VB}) + (H_2O \rightarrow H^+ + OH^-) \rightarrow MgO + H^+ + \cdot OH \tag{4.3}$$

$$GNPs(e^-_{CB}) + O_2 \rightarrow GNPs + \ O_2^- \tag{4.4}$$

$$O_2^- + (H^+ + OH^-) \rightarrow H_2O \cdot + OH^- \tag{4.5}$$

$$ROS + Methyl\ orange \rightarrow \ H_2O + CO_2 \tag{4.6}$$

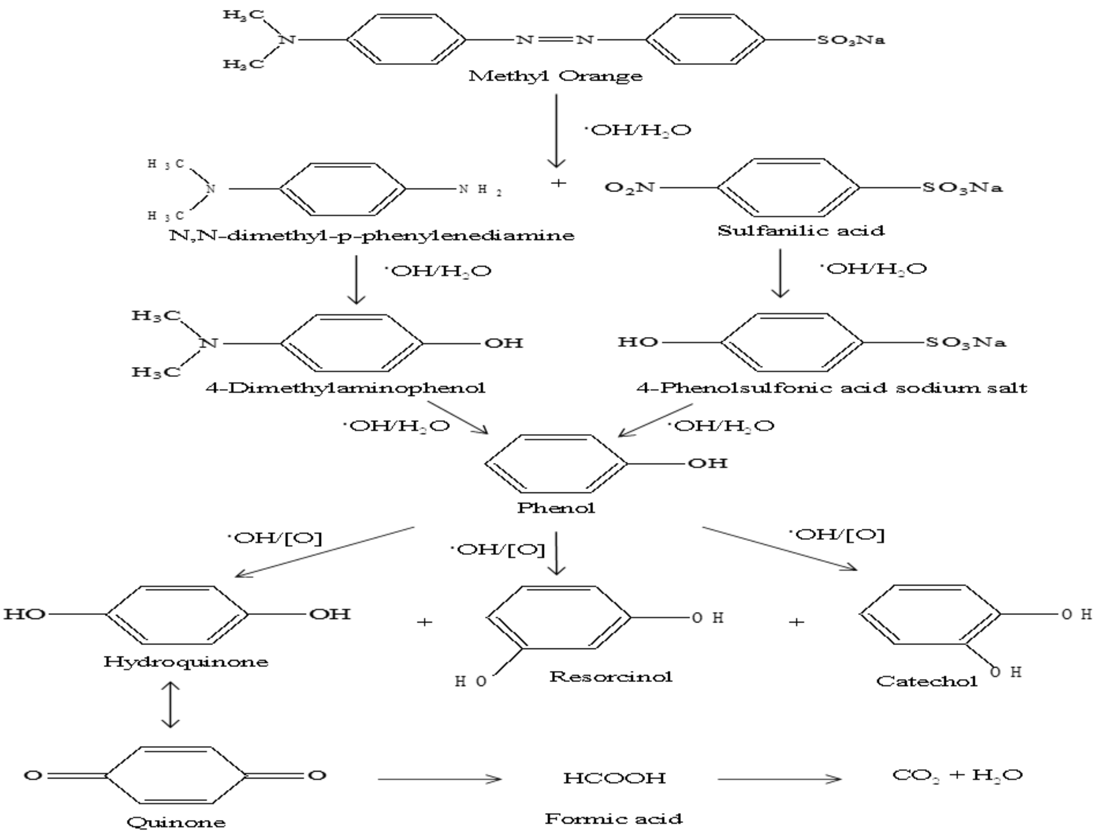

Figure 4. 7 Schematic illustration of the conversion of methyl orange to intermediates in the presence of ROS.

Figure 4. 8 depicts that MgO possess much stronger intensity which is an indication of fast recombination of photo-generated e^-_{CB} - h^+_{VB} pairs. Whereas the inclusion of graphene nanoplatelets significantly reduces PL intensity. The charge trapping induced by GNPs provides clue for an excellent photocatalytic activity of MgO/GNPs 25% nanocomposite.

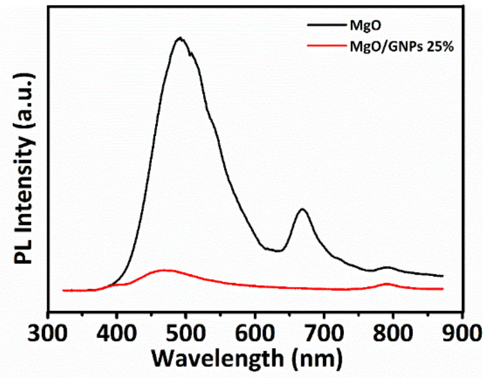

Figure 4. 8 Photoluminescence spectra of MgO and MgO/GNPs 25% nanocomposite.

This behaviour is reported previously as well.[240, 241] Moreover, the remarkable increase of photocatalytic activity of MgO/GNPs nanocomposites can also be attributed to the strong interaction between MgO and defect sites of GNPs and MgO nanocomposite. To thoroughly investigate the photocatalysis process the apparent rate constants of the reactions are determined by applying pseudo first order kinetics. The rate constants are determined by using expression

$$ln\left(\frac{C_o}{C_t}\right) = kt, \qquad (4.7)$$

where k is the apparent rate constant and is obtained by linear fitting of the data as presented in Figure 4. 9. The apparent rate constant increases significantly for MgO/GNPs 25% (0.02 m^{-1}) where as it is 0.003 m^{-1} and 0.004 m^{-1} for MgO and MgO/GNPs 12% respectively. The photocatalytic findings suggest a way for the fast and efficient degradation of methyl orange by modification of MgO. These results are extremely better than previous study where methyl orange was degraded up to 92% and 96% in 270 m and 210 m respectively.[242] It is essentially important to study the stability and durability of the photocatalysts for practical benefits. The recyclability performance of MgO/GNPs 25% nanocomposite was studied under similar conditions.

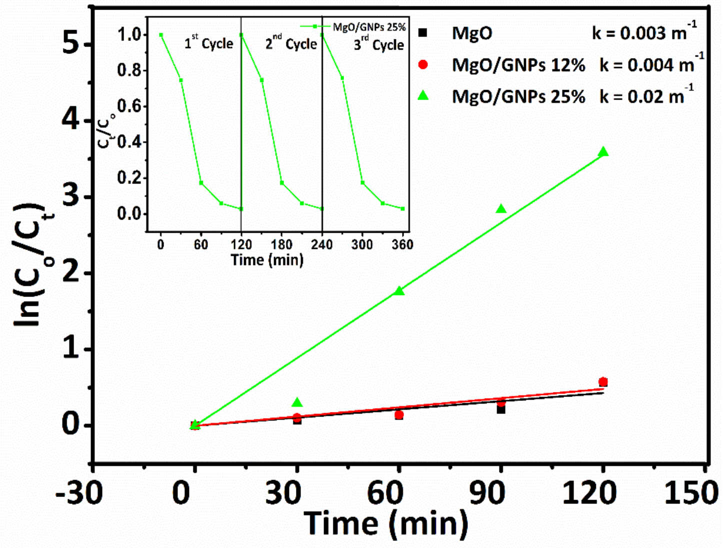

Figure 4. 9 Pseudo first order kinetics of degradation of methyl orange in the presence of MgO and MgO/GNPs nanocomposites. Inset is the recyclability performance of MgO/GNPs 25% nanocomposite.

The inset in Figure 4. 9 shows that the MgO/GNPs 25% nanocomposite shows no significant loss of photocatalytic activity during three successive UV activated degradation experiments. The results indicate that MgO/GNPs 25% nanocomposite is an excellent photocatalyst under the UV light irradiation for practical benefits. Here results clearly show that methyl orange could be removed up to 97.23% by the photocatalyst MgO/GNPs 25% nanocomposite in much less time i.e., 120 m with high apparent rate constant.

4.2.4 Antibacterial Activity

MgO is considered as nontoxic material for human and animal tissue as it is used as anti-laxative and relieving agent of stomach burn. It has well known antibacterial activity.[182, 221, 228] In this study, the effect of increased amount of GNPs on the antibacterial activity of MgO/GNPs nanocomposites is comprehensively investigated. The antibacterial activity of MgO/GNPs nanocomposites is evaluated against both Gram positive (*S. aureus*) and Gram negative bacterial strains (*P. aeruginosa*, and *E. coli*). The results are obtained by analysing the bacterial strains in the absence and presence of aqueous colloidal suspensions of MgO/GNPs nanocomposites for an incubation time of 24 h. Absorbance at 600 nm was recorded up to 24 h to monitor the growth profile of the bacteria in the presence and absence of the test samples. The results of time kill assay are presented by growth inhibition curves in Figure 4. 10. The control sample represents the untreated bacterial strains. The nanocomposites show antibacterial activity towards all the three bacterial strains. It is found that growth of *S. aureus* is significantly inhibited in the presence of MgO/GNPs 25% nanocomposites as compared to MgO/GNPs 12% as presented in inset of Figure 4. 10 (49% and 25% respectively). For *E. coli*, the MgO/GNPs 12% and MgO/GNPs 25% nanocomposites inhibit 33% and 44.5% growth rate respectively. The findings further reveal that

22% and 22.38% growth of *P. aeruginosa* is inhibited by MgO/GNPs 12% and MgO/GNPs 25% nanocomposites respectively. Thus, the time kill assay suggests that MgO/GNPs 25% nanocomposites have been found more effective as compared to MgO/GNPs 12% nanocomposites in controlling the bacterial growth.

The increased quantity of GNPs in the nanocomposites results into higher inhibition of growth, i.e., MgO/GNPs 25% has highest inhibition growth rate for *S. aureus* i.e., 49% inhibition of bacterial growth is achieved. So, it is slightly more effective to inhibit the growth rates for Gram positive bacterial strains.

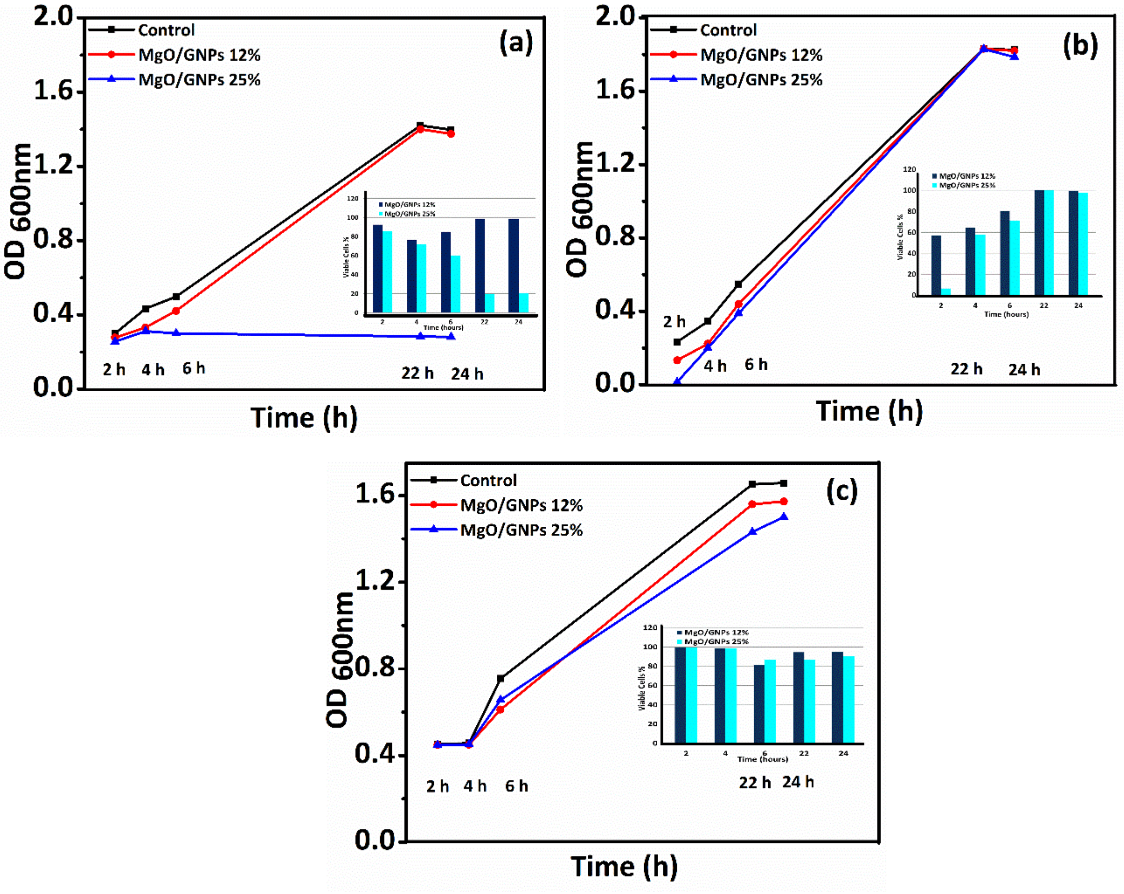

Figure 4. 10(a)-(c) Effect of MgO/GNPs nanocomposites on the growth of different bacterial strains (a) *S. aureus*, (b) *E. Coli*, and (c) *P. aeruginosa*. Insets depict the cell viability analysis in the presence of MgO/GNPs nanocomposites.

The exact mechanism responsible for loss of bacterial integrity is still under debate. In previous studies, various mechanisms have been proposed to account for reduction in the growth rate of pathogenic bacteria. The MgO decorated sheets like structure of GNPs (as confirmed by FE-SEM and TEM images in Fig. 2 (b) and (d)) demonstrates that bacterial strains may develop an intimate contact with the rough surface of MgO loaded GNPs. The edges of GNPs exert stress on the bacterial cell wall, leading to rupturing of the cell membranes with ultimate leakage of the bacterial cytoplasmic content. These edges play the role of cutters for cell membranes. It results into bacterial cell death.[153, 243] Similar antibacterial mechanism involving physical contact of tubes with bacteria and internalization of small tubes has been suggested for SWCNTs, MWCNTs and fullerenes as well. All these species are chemically like graphene.[244-247] It may be further suggested that wrapping of sheet like nanocomposites around bacteria provides higher concentration of metal oxide nanostructures (MgO in our case) on bacterial surface. It is elucidated by Raman spectra in Fig. 4, that nanocomposites are rich in defects. The rough surface of MgO decorated GNPs envelops the bacteria. The loss of bacterial membrane integrity is the consequence of accumulations of MgO nanohexagons.[248]

Another plausible mechanism is suggested recently for graphene induced cell death. In few recent researches, it has been additionally reasoned that charge imbalance on cell membrane leads to membrane collapse. As the cell membrane of bacteria are negatively charged. Graphene family nanostructures are considered as good electron acceptors due to their exceptionally high electrical conductivity. The contact between bacteria and nanocomposite may result in flow of negative charge from bacterial membrane to the GNPs which provide a conductive network enveloping the cell membranes. This leads to charge imbalance on the bacterial cell membrane, thus inducing the bacterial death.[95] Some studies on other metal oxide/graphene based nanocomposites have suggested that the release of positive metal ions (Mg^{2+} ions from MgO nanohexagons in present study) followed by penetration of ions into the cell membranes eventually induces bacterial death.[92]

In the light of above discussion, it is suggested that superior antibacterial performance of MgO/GNPs nanocomposites is the synergistic effect of edge stress created by GNPs, Mg^{2+} ions internalization by bacteria and charge imbalance created on bacterial cell boundary (due to flow of negative charge from membrane to GNPs). Gram negative bacteria have been found to be relatively more resistant as compared to Gram positive *S. aureus* bacteria.

S. aureus is antibiotic resistant and is potentially harmful. It spreads very easily on direct contact with the infected person or contaminated objects. *E. coli* are generally found in intestine and can be transferred from unsafe drinking water and food. They may cause intestinal infections. Therefore, it is essential to develop cheap, easy to produce and effective antibacterial agents giving control over growth of pathogenic bacteria. In this regard MgO/GNPs 25% nanocomposite is an effective antibacterial agent. We envision that antibacterial performance of MgO/GNPs nanocomposites can further be tailored by variation of dose rates during incubation and by changing the quantity of GNPs in the nanocomposites.

4.3 Summary

The MgO/GNPs nanocomposites with different concentrations of GNPs have been synthesized successfully by a simple solvothermal route. The electron accepting nature of GNPs plays the vital role for making MgO/GNPs 25% nanocomposite bifunctional. The assembly of GNPs and MgO provides an efficient route to enhance the photocatalytic properties of MgO nanohexagons up to 97.23% in 120 min under UV light irradiation. The investigation of GNPs amount dependent antibacterial activity reveals that MgO/GNPs 25% nanocomposite shows a higher toxicity towards S. aureus and E. coli with 49% and 44.5% inhibition of growth, respectively. Therefore, the prepared nanocomposite MgO/GNPs 25% can be used as a multifunctional material for cleaning of waste water and antibacterial agent.

Chapter No. 5

5. Synthesis, Characterization and Applications of Graphene/SiO_2 Nanocomposites

Overview:

This chapter presents the physio-chemical characterizations, photocatalytic and antibacterial applications of graphene/SiO_2 nanocomposites. X-ray diffraction, morphological analysis, HR-TEM, SAED and Raman spectroscopic results are included to demonstrate the physio-chemical properties of prepared materials. The addition of graphene nanoplatelets with SiO_2 nanoparticles enhances the photocatalytic efficiency from 46% to 99%. For biomedical applications, it is found that 75% of Gram positive and 50% of Gram negative bacteria have been killed.

5.1 Introduction

Metal and non-metal oxides have been extensively studied for photocatalysis and biomedical applications.[249-252] Among them, SiO_2 has the prime importance as it is the promising candidate for future development of catalysts, adsorbents, nano drug carriers, and biomolecular transport agents.[253-259] However, some demerits of SiO_2 restrict its efficiency in photocatalysis and biomedicine, which are the wide bandgap (ca. 5 eV), aggregation of NPs, quick charge carrier's recombination, and low surface area. These factors contribute to its inert behaviour towards many catalytic processes, and it shows only a slight catalytic activity under UV irradiation.[236, 258] To improve its photocatalytic performance, it is highly desirable to combine carbonaceous materials with SiO_2, as various studies indeed describe their efficacy for remediation of contaminated water.[260, 261] As mentioned in previous chapter that harnessing good electronic transport and other physical properties of graphene with those of ceramics (e.g., MgO) can significantly enhance the performance of materials in photocatalysis and biomedical applications,[262] but a significant antibacterial activity was not achieved in case of MgO/GNPs nanocomposites.

SiO_2 was opted with an aim to improve the results that were previously obtained. SiO_2 NPs decorated graphene nanoplatelets (GNPs) have hybrid properties of both nanomaterials, e.g., improved interfacial contact (leading to large surface area), development of conducting pathways, and suppression of charge recombination. Incorporating these features via formation of graphene/SiO_2 nanocomposites provides a superior channel for enhancement of the photocatalytic performance as compared to other carbonaceous nanocomposites or SiO_2 alone.[109] Thus, these merits make graphene/SiO_2 nanocomposites potentially new candidates for averting the ever-growing health and environmental risks associated with contaminated water. Graphene family based nanocomposites with SiO_2 have recently been studied in detail for various applications, e.g., liquid chromatography, fluorescence enhancement, and super hydrophilic coatings.[263-268] Despite these few reports, there is still a lot of room to probe the various aspects of graphene/SiO_2 nanocomposites. For example, health and environmental impacts of graphene/SiO_2 nanocomposites need to be thoroughly evaluated before employing it for potential applications. In this work, the photocatalytic activity under UV light illumination for an organic dye methyl orange, and antibacterial features of graphene/SiO_2 nanocomposites for three model bacteria have been evaluated. To the best of our knowledge, it is the first time, this study explores the impact of graphene on the role of SiO_2 in the fast photodegradation of methyl orange and inhibition of the bacterial growth.

5.2 Results and Discussion

5.2.1 Structural and Morphological Analysis

The crystallinity of prepared samples is analysed from 20^o to 80^o using XRD as depicted in Figure 5. 1. The presence of diffraction peak at 26.4^o corresponds to C (002) of the graphitic host matrix and agrees with JCPDS-NO: 75–1621. The X-ray diffractograms show a broad halo in the region $2\theta = 20^o – 30^o$. This obtuse peak indicates the amorphous nature of SiO_2. The X-ray diffractograms agree with the previous study.[269]

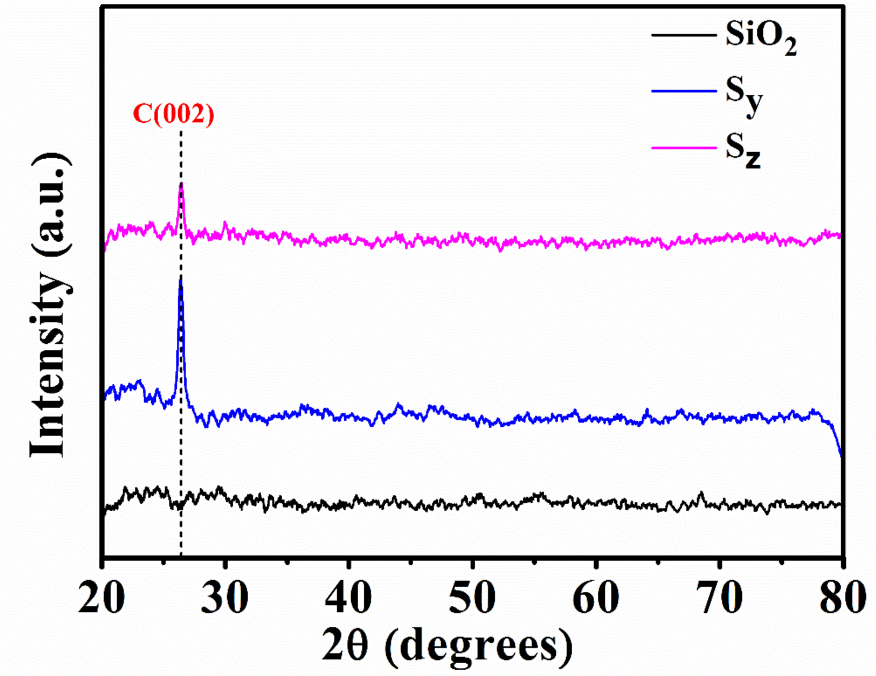

Figure 5. 1 X-ray diffractograms of SiO$_2$ and graphene-SiO$_2$ nanocomposites. S$_y$ and S$_z$ nanocomposite contain 8% and 12% graphene respectively.

Morphological investigations have been carried out to understand the shape and attachment between the constituent species. Figure 5. 2(a) illustrates that SiO$_2$ sample shows spherical shape, monodispersed particles with the diameter ranging from 230 nm to 260 nm. Figure 5. 2(b) and (c) reveal the microstructure of graphene/SiO$_2$ nanocomposites. The semi-transparent graphene sheets with anchored SiO$_2$ NPs are clearly visible in Figure 5. 2(b) and (c), thereby confirming the intercalation of GNPs into few layers of graphene sheets. The insertion of SiO$_2$ NPs has thus served to reduce the van der Waal’s interaction between the stacked GNPs. It is interesting to note that the particle size of SiO$_2$ has been greatly reduced during nanocomposite formation, which is logical and expected as well. This is due to the confinement effect of graphene sheets, and has been observed in previous reports on graphene/metal oxide’s nanocomposites.[186] Moreover, the large surface area provided by graphene during the growth process serves to reduce the excessive aggregation of primary nuclei.

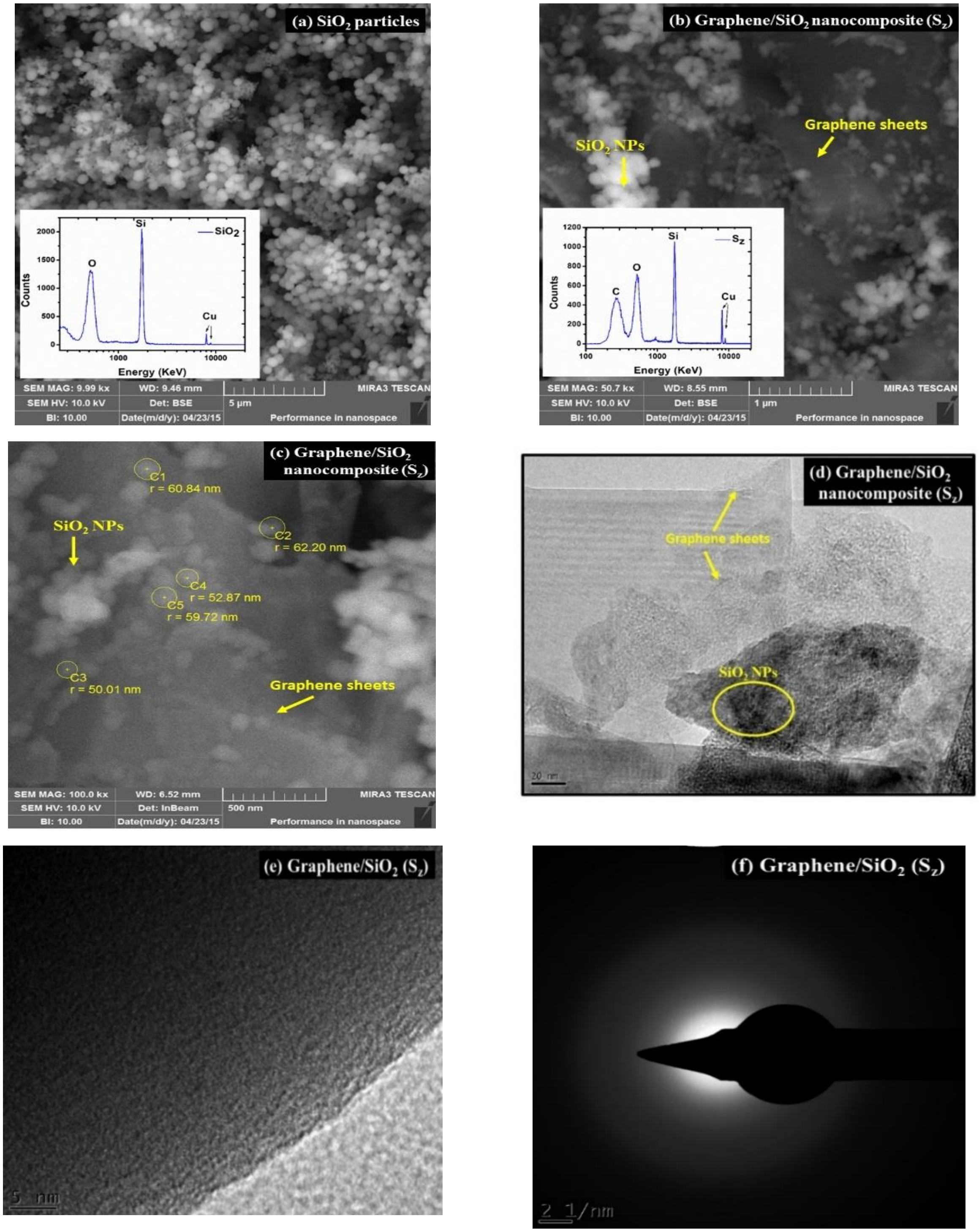

Figure 5. 2 (a) SEM micrograph of monodispersed SiO_2 particles; the inset shows the EDX spectrum of SiO_2, (b) and (c) Graphene/SiO_2 nanocomposite; the inset shows the EDX spectrum. (d) TEM image of the graphene/SiO_2 nanocomposite (S_z), (e) HR-TEM image of SiO_2 NP attached on graphene sheet, and (f) SAED pattern of SiO_2 NPs attached to the graphene sheet.

An energy dispersive X-ray spectroscopy (EDX) coupled with FE-SEM was used to investigate the composition of pristine SiO_2 and graphene/SiO_2 nanocomposites. The presence of carbon, silicon, and oxygen is confirmed by peaks [see insets in the left bottom of Figure 5. 2(a) and (b)]. To further investigate the nature of SiO_2 and nanocomposites, TEM, high resolution TEM and selected area electron diffraction (SAED) patterns are presented in Figure 5. 2 (d)-(f). TEM image demonstrates that the SiO_2 NPs are attached to graphene sheets. A high resolution TEM image in Figure 5. 2 (e) shows no lattice spacing. It clearly displays the amorphous nature of SiO_2 NPs that are attached to graphene. The SAED pattern supports the observation from X-ray diffractograms. The image illustrates the polycrystalline nature of graphene/SiO_2 nanocomposite.

5.2.2 Raman Spectroscopic Analysis

Raman spectroscopy is the basic characterization tool to identify graphene and its nanocomposites. The Raman spectra obtained from 1000 cm^{-1} to 2100 cm^{-1} are presented in Figure 5. 3. All samples show the D band, associated with defects, located around 1350 cm^{-1}. The defect band arises due to termination of the sheet at the edges and attachment of particles on graphene. The intensity of D band increases after the inclusion of SiO_2 nanoparticles on the surface of graphene. Moreover, it also broadens, which indicates that successful incorporation of nanoparticles. The E_{2g} mode arises due to first order scattering and is manifested as the G band, located at 1587 cm^{-1} in the case of GNPs. These observations agree with the previous reports on graphene's Raman spectra.[192, 270] The nanocomposites S_y, and S_z have the G-band located at 1599 cm^{-1}, and 1602 cm^{-1}, respectively. An overall shift towards a higher wavenumber of the G-band is observed in all the nanocomposites as compared to GNPs. This shift is due to the charge transfer between GNPs and SiO_2 NPs and is an indicator of the electrostatic interaction between the two-constituent species. This large shift illustrates the strong attraction between the two constituent phases of nanocomposites. The Raman results confirm the formation of GNPs and SiO_2 nanocomposites.

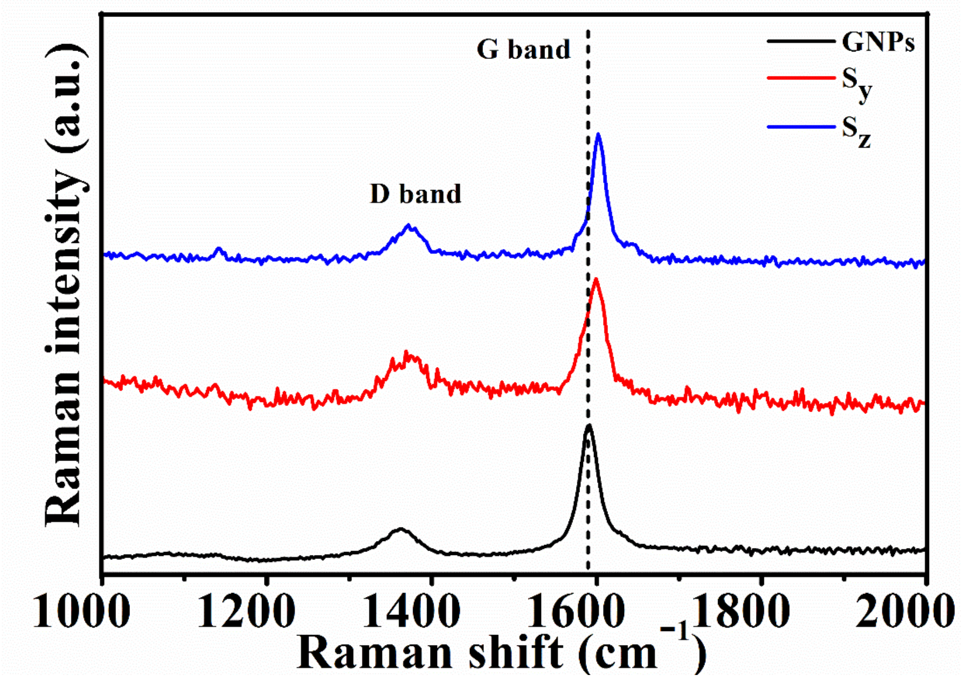

Figure 5. 3 Raman spectra depicting the formation of graphene/SiO_2 nanocomposites

5.2.3 Photoluminescence Analysis

The incomplete Si-O-Si tetrahedral network formation on the surface of graphene may lead to several structural defects. The SiO_2 nanoparticles show emission peaks in the visible light region. A weak band near the UV region, 355.6 nm (3.48 eV) is contributed by silanol groups (–OH related groups). Green emission at 512 nm (2.43 eV) is observed. A very prominent band at 409 nm (3.04 eV) is observed related to violet emission.[271, 272] All these peaks are observed by nanocomposites as well but the intensity is relatively weak. The comparison of the PL results of graphene/SiO_2 nanocomposites and SiO_2 indicates that the intensity of all the emission peaks quenches significantly. This suppression is attributed to the presence of graphene, which acts as an acceptor of electrons in the nanocomposite.[241] Graphene sheets provide an additional path for the conduction electrons of SiO_2. The suppression of PL intensity indicates the decrease in carriers' recombination. This quenching behaviour agrees with the previous reports and suggests the potential photocatalytic use of prepared nanocomposites. The spikes seen in S_y and S_z are due to background noise.

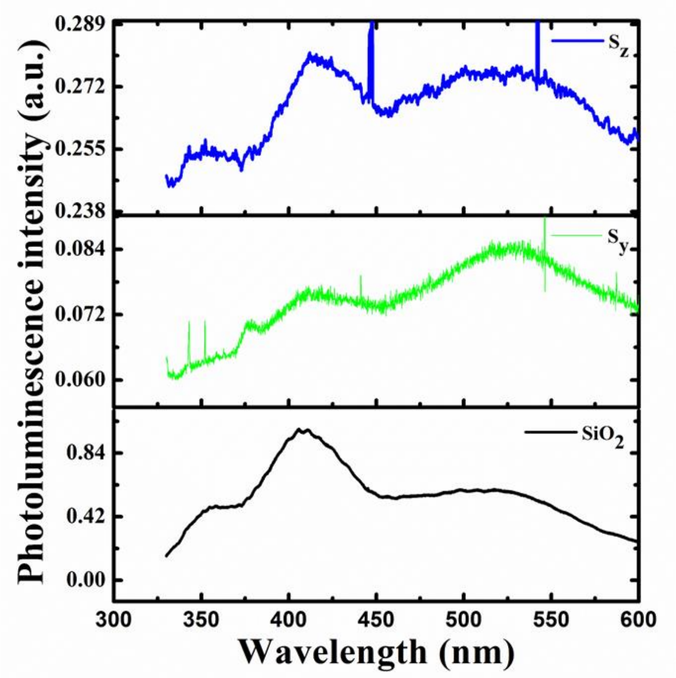

Figure 5. 4 PL spectra of SiO_2 and graphene/SiO_2 nanocomposites

5.2.4 Photocatalytic Activity

To evaluate the performance of graphene/SiO_2 nanocomposites, methyl orange was employed as a water contaminant in photoinduced dye-degradation experiments. To study the impact of graphene concentration on methyl orange degradation, three experiments were conducted using catalysts SiO_2, S_y, and S_z. The adsorption process (in the dark) degrades the dye molecules slightly. Figure 5. 5(a)–(c) show the absorption spectra showing the degradation of methyl orange. The photodegradation efficiencies of methyl orange are presented in Figure 5. 6

using different photocatalysts. In the presence of SiO_2, 46% photodegradation is achieved in 160 min. The catalyst S_y has shown 92% photodegradation of methyl orange in the 160 min. The photocatalytic efficiency of graphene/SiO_2 nanocomposite is found to be maximum at the optimal graphene content in the photocatalyst S_z, which shows 99% photodegradation in considerably reduced time. The spectrum becomes flat only in 100 min. The photocatalytic efficiency obtained in the present case is much better than the previous report on the photocatalytic activity of SiO_2 NPs with Au/Ag doping.[236, 258]

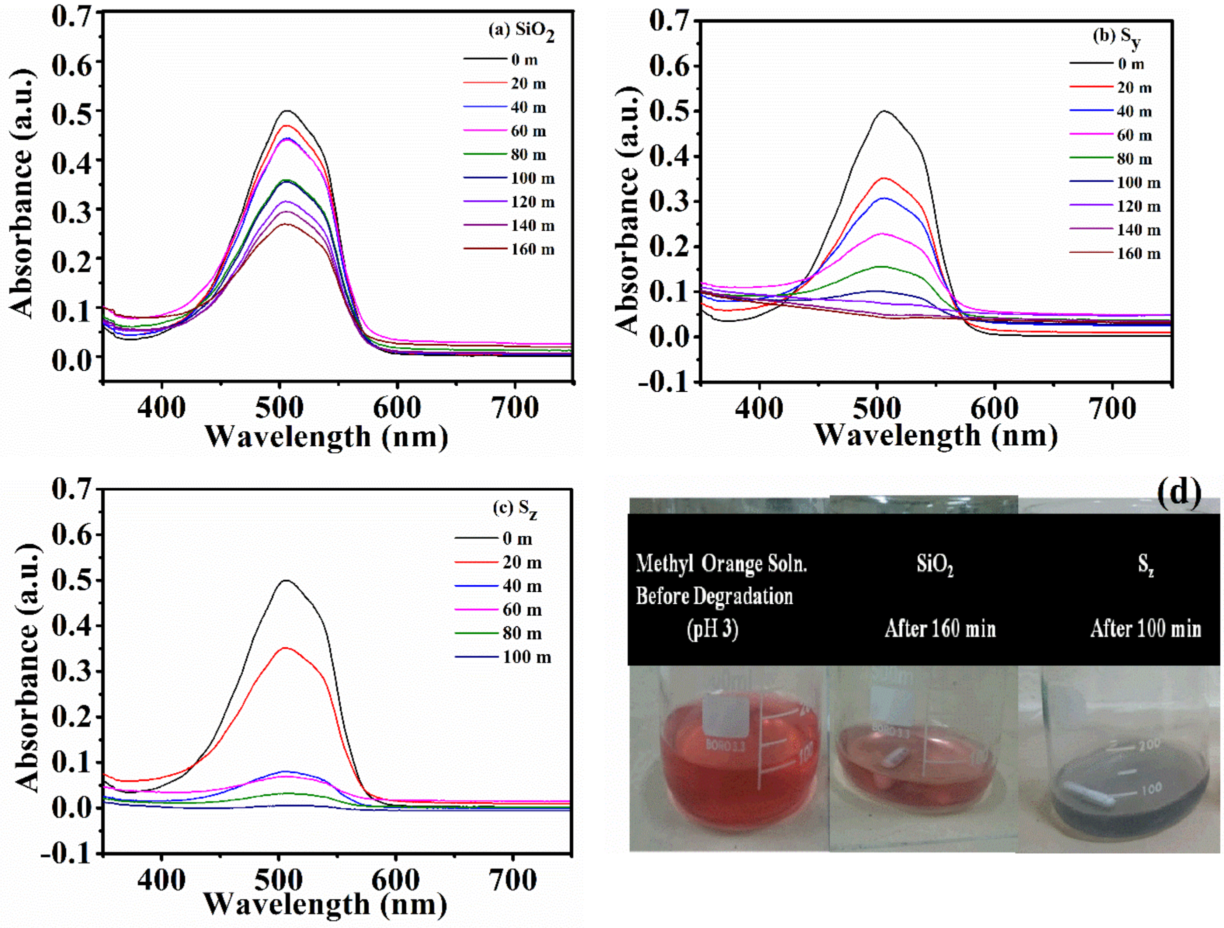

Figure 5. 5 UV-Vis absorbance spectra of methyl orange in the presence of different photocatalysts, i.e., SiO_2, S_y, and S_z

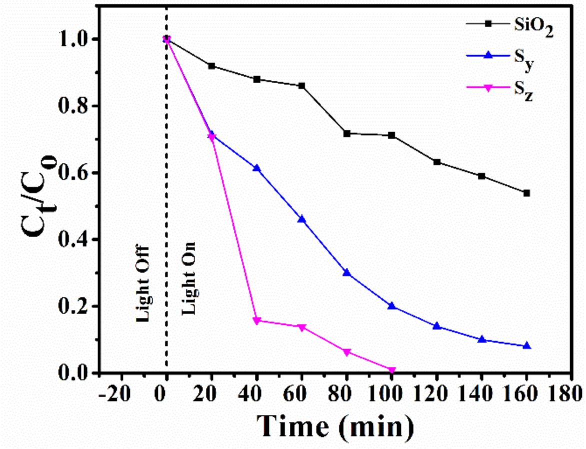

Figure 5. 6 Photodegradation of methyl orange by SiO_2 and graphene/SiO_2 nanocomposites

The mechanism of photocatalytic activity is explained below. The photons of UV light falling on the SiO_2 NPs excite its valence band electrons to the conduction band and produce e^-_{CB} - h^+_{VB} pairs. The number of e^-_{CB} - h^+_{VB} pairs increases gradually with time. The graphene attached to SiO_2 NPs, being a good acceptor of electrons, provides trapping sites for e^-_{CB}. This delays the recombination of e^-_{CB} - h^+_{VB} pairs. Meanwhile, the e^-_{CB} may also interact with the dissolved O_2 to produce O^{2-} species, which may further produce several reactive oxygen species (ROS). The holes in the valence band of SiO_2 contribute to the generation of •OH radicals.[236]

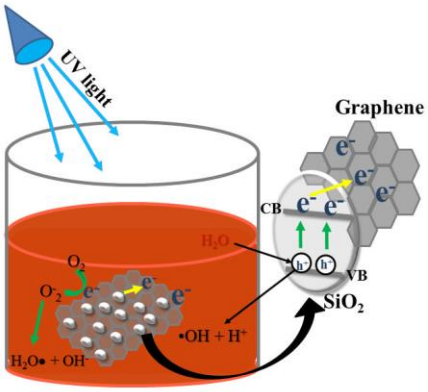

Figure 5. 7 Proposed mechanism for UV light induced catalysis of MO using graphene/SiO_2 nanocomposite

These species attack the ring of the azo dye, methyl orange, by completely opening its ring structure. This ultimately results in the mineralization of dye.[262] The mechanism is schematically illustrated in Figure 5. 7.

In the case of bare SiO_2 particles, the e^-_{CB} - h^+_{VB} pairs formed on the surface of SiO_2 recombine quickly. Only very few carriers can be trapped on the surface states of SiO_2 particles, which may further initiate the dye degradation. The amount of ROS generated in the process strictly controls the dye degradation. Fewer ROS can react with adsorbed dye molecules. In this case, the absence of graphene leads to quick recombination of e^-_{CB} - h^+_{VB} pairs. That is why SiO_2 particles have shown low photocatalytic activity as compared to graphene/SiO_2 nanocomposites. Notably, all the nanocomposites have not shown similar photoactivity for the degradation of methyl orange. It indicates that the importance of the optimum addition ratio of graphene in nanocomposites. The explanation for the graphene content dependence on the photocatalytic performance of the nanocomposites is elucidated below.

Incorporating graphene in nanocomposites seems to promote electron trapping. This is due to the exceptional conductivity of graphene. The retardation in recombination of UV light generated charge carriers in SiO_2 by introducing graphene nanoplatelets gets support from photoluminescence spectra in Figure 5. 4. PL findings suggest that the quenching of intensity is due to the inhibition of charge carrier’s recombination in nanocomposites, as electrons are accepted by the graphene lying adjacent to the SiO_2 NPs. This inhibition ultimately results in the efficient photocatalytic performance of nanocomposites as compared to SiO_2 alone. The highest quenching is observed in S_z, which supports the photocatalytic results. The nanocomposite having the highest quenching has shown most efficient photocatalytic activity by 99% degradation of methyl orange in 100 min. Hence, the synergistic effect created by conducting graphene and high surface area of nanocomposite is helpful towards fast and efficient degradation of dye.[251, 260]

The reaction kinetics of the experiment provide a better insight into the photocatalytic activity. The reaction kinetics for photocatalysis can be described based on the Langmuir-Hinshelwood model[273] as presented in Figure 5. 8.

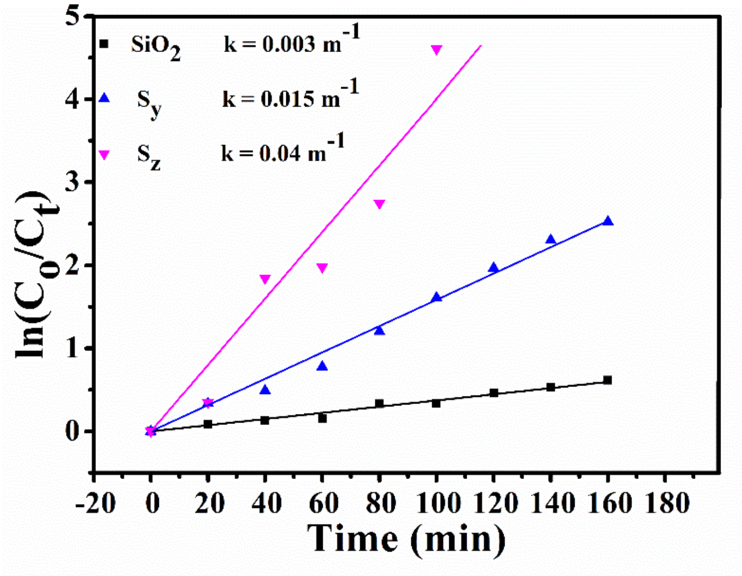

Figure 5. 8 Pseudo first order rate kinetics for photocatalytic reactions by SiO_2 and graphene/SiO_2 nanocomposites.

The UV light induced degradation of MO can be well ascribed by pseudo-first order kinetics. The rate equation that describes the reaction is $\ln(C_o/C_t) = kt$, where k = apparent rate constant. The apparent rate constants for different catalysts are 0.003 min^{-1} (SiO_2), 0.5 min^{-1} (S_y), and 0.04 min^{-1}(S_z). These results show that the rate constant has been increased significantly by increasing graphene content. The graphene/SiO_2 nanocomposite with maximum graphene loading has the highest apparent rate constant (an order of magnitude higher than that of bare SiO_2 particles), and therefore, it exhibits excellent photocatalytic activity. Hence, it can be concluded that the S_z nanocomposite is photocatalytically most active than pristine SiO_2 and graphene/SiO_2 nanocomposites with a low graphene content for the degradation of methyl orange.

The recyclability tests are very important for the practical use of photocatalysts. The recycling performance of S_z was evaluated for three consecutive cycles. It is illustrated in the Figure 5. 9 that there is a negligible loss in photocatalytic activity of S_z. The S_z nanocomposite shows excellent performance even after three continuous cycles of activity. Therefore, it may be recommended as an efficient alternative of traditional photocatalysts.

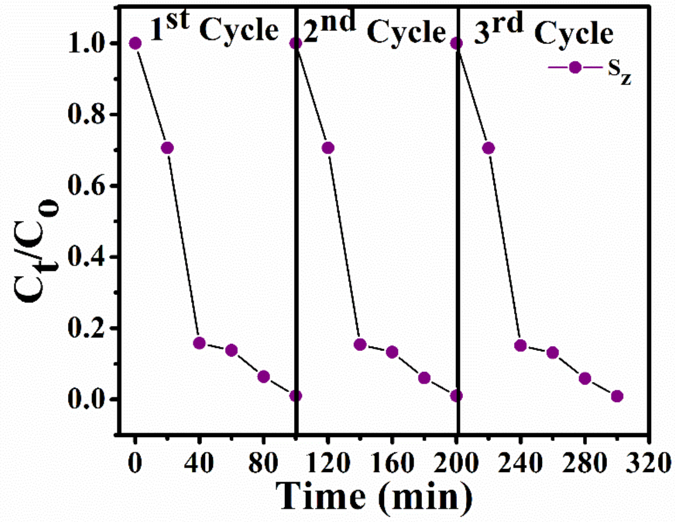

Figure 5. 9 Recyclability curves of the graphene/SiO_2 nanocomposite (S_z), depicting its excellent performance in the three consecutive cycles of photocatalysis.

5.2.5 Antibacterial Activity

To investigate the effect of graphene/SiO_2 nanocomposites on Gram negative and Gram positive bacteria, the time kill assay was conducted for three model bacterial strains, i.e., *E. coli*, *P. aeruginosa*, and *S. aureus* in the absence and presence of all samples. The growth inhibition rate was determined by observing the optical density (600 nm) at different intervals in the total incubation time (24 h). The results obtained from the experiment are presented by the bacterial growth inhibition curves in Figure 5. 10(a)-(c). The control sample in Figure 5. 10(a)–(c) presents the untreated bacterial strains under observation for comparison purposes. The experimental findings suggest the inhibition of bacterial growth to a significant extent. It is observed that bacterial growth inhibition is a strong function of graphene loading in the nanocomposites. The growth of *S. aureus* has been inhibited up to 26.32%, 50.30%, and 75.40% by SiO_2, S_y, and S_z, respectively. For *E. coli*, the growth inhibition rates are 17.00%, 32.23%, and 51.80% for SiO_2, S_y, and S_z respectively. The growth of *P. aeruginosa* has been inhibited up to 17.75%, 40.77%, and 48.97% by SiO_2, S_y, and S_z, respectively.

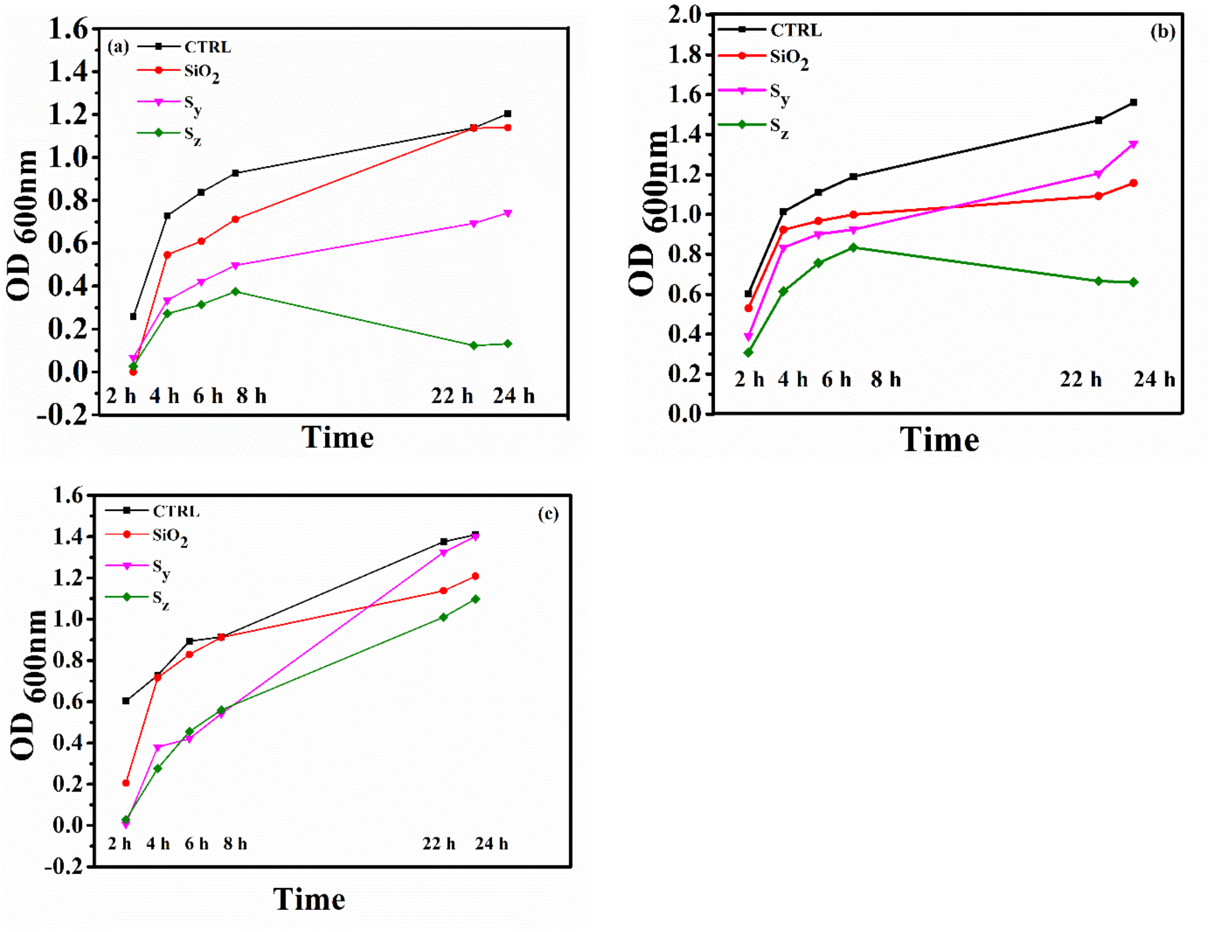

Figure 5. 10 Bacterial growth inhibition curves obtained via MTT assay for (a) Methicillin resistant *S. aureus*, (b) *E. coli*, and (c) *P. aeruginosa*.

The sample with no graphene contents, i.e., SiO_2, shows the minimum inhibition of bacterial growth for all the bacterial strains. The increase of graphene loading decreases the number of viable cells. The maximum growth inhibition rate is achieved in a nanocomposite with a maximum graphene content. The sample with maximum graphene loading (S_z) is found to possess excellent antibacterial properties for the growth inhibition of *S. aureus*. Graphene/SiO_2nanocomposites have stopped around 50% growth of Gram negative bacterial strains. These results are much better than the previous reports, where growth inhibition of 47% and 49.5% 64.8% for *E. coli* and 34% for *S. aureus* was achieved by rGO and graphene films.[153, 274]

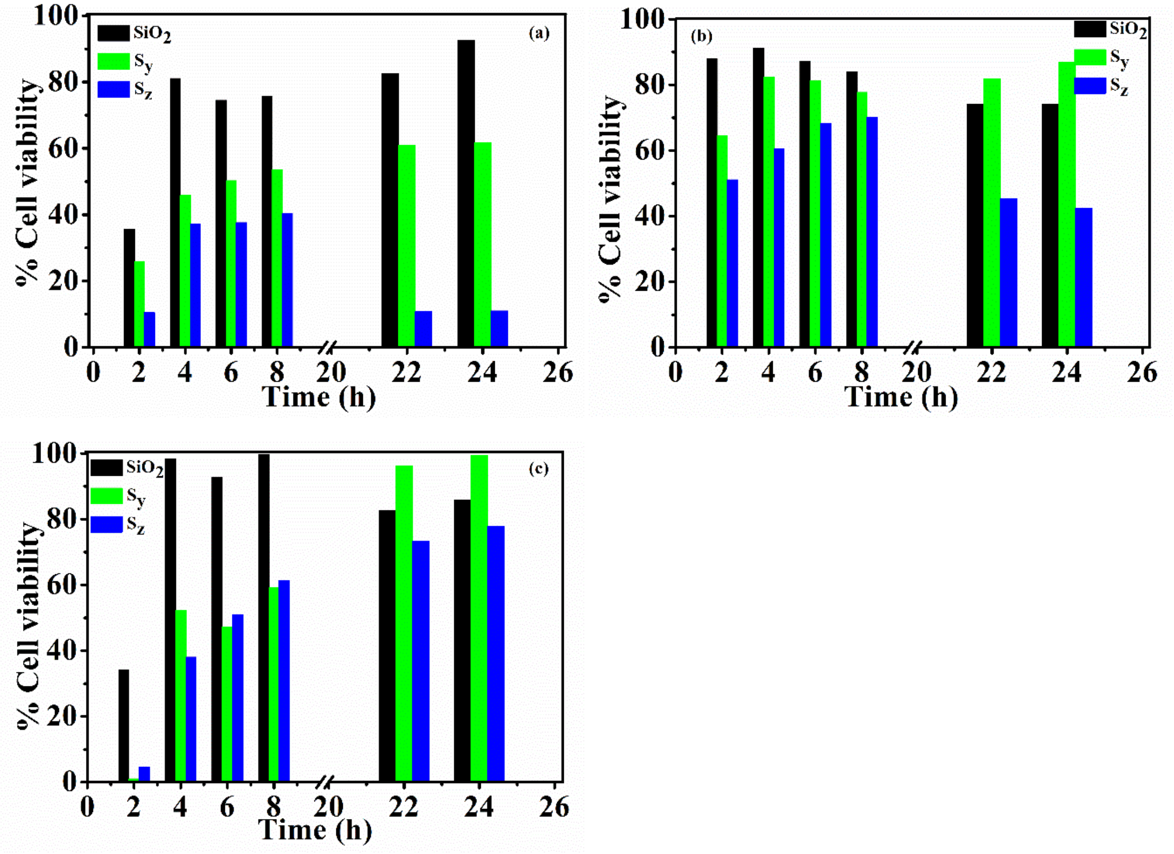

Figure 5. 11 % cell viability of bacterial strains (a) Methicillin resistant *S. aureus*, (b) *E. coli*, and (c) *P. aeruginosa*.

Several research reports are available, documenting the possible mechanisms for growth inhibition of bacterial strains by carbon nanotubes, fullerenes, and graphene family nanostructures.[243, 275-277] However, the exact mechanism explaining the loss of bacterial viability is still a researchable topic. One of the suggested mechanism is the destruction of the bacterial membrane induced by the direct contact between the sheet like structures of graphene based materials and bacteria. This mechanism has been proposed previously for GO, rGO, and CNTs.[153] In the present case, the intermingling of bacteria and planar graphene may be thought to induce irreversible destruction of the bacterial membrane. The planes and sharp edges of graphene nanosheets produce significant stress on cell membranes. These edges serve as cutters for rupturing the bacterial cell membranes which induce cell death by leakage of the cytoplasmic content. Additionally, the normal respiratory functioning of bacteria is strongly dependent on electronic charge transport between the cell and mitochondrial membranes in respiratory chain reactions. The physical contact between bacteria and graphene/SiO_2nanocomposites may result in Schottky barrier formation, as previously reported for graphene on a SiO_2 substrate.[92] As graphene is an excellent electron acceptor, it can be speculated that the cell membranes may lose their electrons, which are eventually transported to graphene. In this manner, a charge imbalance is created in the bacterial cells, which leads to cell death.[92, 278] However, the differential toxicity of samples towards Gram positive and Gram negative bacteria can be explained based on their outer membrane's composition. The Gram-negative bacteria have a complex double membrane's structure which is less penetrable as compared to the single membrane of Gram positive bacteria. This difference, mainly arising due to the chemical composition of membranes of the two classes of bacteria, develops their differential resistance.[180, 244] Hence, this feature makes *S. aureus* an easy target for graphene/SiO_2 nanocomposites.

5.3 Summary

High surface area graphene/SiO_2 nanocomposites are synthesized successfully by a simple chemical route. The composite developed with retention of the exceptional intrinsic properties of graphene leads to achieve the outstanding photocatalytic performance with 99% degradation of methyl orange under UV light illumination. Graphene loaded with SiO_2 shows excellent antibacterial activities, i.e., 75% growth inhibition of *S. aureus* and *ca.* 50% loss of *E. coli* and *P. aeruginosa*. Our experimental findings greatly recognize graphene/SiO_2 nanocomposites for their utilization towards wastewater treatment and biomedical applications.

Chapter No. 6

6. Synthesis, Characterization and Applications of Graphene/Fe_3O_4 Nanocomposites

Overview:

Magnetic graphene/Fe_3O_4 nanocomposites obtained via soft chemical method are characterized for their crystallinity, morphology, microstructure, vibrational modes and magnetic properties. Graphene sheets decorated with magnetite nanoparticles are investigated for their photocatalytic response against methyl orange. The magnetically separable photocatalyst F_z, presented in this chapter, offers great prospects for fast and economical decontamination of dye polluted water. In addition, this chapter also presents the performance of control sample Fe_3O_4 and graphene/Fe_3O_4 nanocomposites against the bacterial strains under consideration. A moderate antibacterial activity is achieved.

6.1 Introduction

It has been shown in last two chapters that ceramic nanostructures loaded on carbon exhibit improved physical and photocatalytic properties as compared to carbon or ceramic nanostructures alone. The enhanced properties of nanohybrids, and nanocomposites arise because of the combination of carbon nanostructures and ceramics in a novel fashion.[279] Graphene derived materials are used as support matrix to anchor ceramic nanostructures, with an aim to prepare band engineered, high surface area multifunctional nanomaterials, that could exhibit a combination of the both components, i.e., inherent outstanding properties of graphene as well as nanoscale features of ceramics as presented in last two chapters.

However, anchoring ceramic nanoparticles onto graphene without attaching oxygen containing moieties (e.g., as the opposite is in the case of graphene oxide (GO) or reduced graphene oxide (rGO)) is more attractive. This is due to the underlying fact that, it helps in retaining the purity of graphene, as oxygen containing functional groups act as impurity atoms and significantly increase sp^2-sp^3 bonds. Therefore, their presence modifies the conductivity of graphene.[51] Which in turn reduces the nanocomposite's efficiency in those applications which are majorly governed by carrier's transport, e.g., photocatalysis. Keeping these factors in view, we envisage that intercalation of graphene nanoplatelets (GNPs) by ceramic nanoparticles gives advantage of carbon purity. Carbon purity, in turn, facilitates the longevity of carrier's lifetime. In addition, high surface area and tuned bandgap energy provide advantage of high adsorption of dye molecules, and fast photo-excitation of carriers respectively.[262, 280-282]

Among ceramics, nanoscale magnetite is widely studied for waste water treatment.[283, 284] The choice of magnetite (Fe_3O_4) nanoparticles gives additional benefit of easy magnetic separation of catalyst from water. Above all, the selection of Fe_3O_4 and graphene makes it possible to utilize photo-Fenton type reaction to present a nontoxic, cost effective and environment friendly way to depollute industrial grade dyes. Fe_3O_4 attached to GO and rGO have been extensively researched to achieve effective degradation of several organic pollutants,[120, 121, 285-290] but the degradation of methyl orange, particularly, by high purity graphene and magnetite's nanocomposite is not reported yet. Herein, we present an easy method to prepare highly stable and magnetically separable graphene/Fe_3O_4 photocatalyst, that retains high carbon purity and possess efficiency to completely remove methyl orange, which otherwise can be removed only 43% by Fe_3O_4 alone.

6.2 Results and Discussion

6.2.1 Structural and Morphological Analysis

The phase purity and crystallinity of prepared nanocomposites was analysed in the range of 10^o – 80^o as presented in Figure 6. 1. A small diffraction peak at 26^o is associated with C (002) of the graphitic host matrix, and agrees with JCPDS-NO: 75-1621. This peak, however, is absent in Fe_3O_4 NPs. No diffraction peak at 10^o is present, which is a strong manifestation of carbon purity and absence of oxygen containing moieties. This indicates that graphene oxide is not present in the nanocomposites. It eliminates the presence of graphene oxide (GO). The diffraction peaks located at 30.48^o (220), 35.6^o (311), 43.02^o (400), 50.3^o (422), 59.1^o (511), 62.9^o (440), and 73.4^o (220) are assigned to the inverse spinel structure of cubic Fe_3O_4, and get verification from JCPDS-NO: 24-0072. No peaks related to hematite or maghemite are observed which confirm the phase purity of prepared samples. The X-ray diffractograms corroborate well with a previous study[291] which provide evidence of formation of nanocomposite.

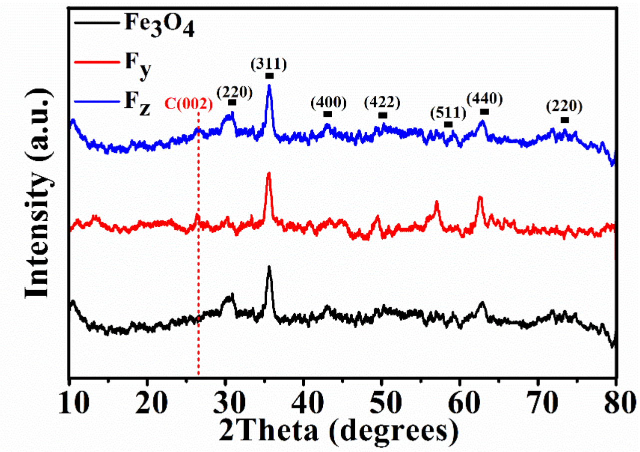

Figure 6. 1 X-ray diffraction patterns of Fe_3O_4 and graphene/Fe_3O_4 nanocomposites

The morphology and surface analysis reveals information about the distribution and anchoring of nanoparticles on graphene's surface. The SEM and TEM images of Fe_3O_4 is presented in Figure 6. 2(a)-(b), which show that they have a spherical morphology. The particle sizes range from 6 nm – 20 nm. A high resolution TEM image shows that the adjacent fringe spacing is found to be 0.253 nm which corresponds to (311) plane of Fe_3O_4 NPs. This observation obtained by HRTEM image of Fe_3O_4 NPs is shown in Figure 6. 2(c) and affirms the XRD results. Figure 6. 2(d) depicts the SAED pattern of graphene/Fe_3O_4 nanocomposite (F_z). The diffraction spots are assigned to C(002) plane of carbon and some planes of Fe_3O_4. These results corroborate with XRD results. A TEM image of graphene/Fe3O4 nanocomposite is given in Figure 6. 2(e). The Fe_3O_4 NPs seem to be anchored on few layers graphene. The magnetic nature of Fe_3O_4 NPs makes them aggregate as apparent in Figure 6. 2(a), (b) and (e). The selected portion of Figure 6. 2(e) is further investigated in HRTEM image (Figure 6. 2(f)), that describes the hybrid nature of nanocomposite. The intercalation of GNPs by Fe_3O_4 NPs is clearly visible in Figure 6. 2(f), and the interface that elaborates the bi-phase nature of nanocomposite, is marked. The morphological investigation indeed confirms the formation of graphene/Fe_3O_4 nanocomposite. The elemental analysis obtained by EDX spectroscopy is presented in Figure 6. 2(g)-(h). The presence of Fe, and

O in Fe_3O_4 and Fe, O, and C in graphene/Fe_3O_4 nanocomposite further verifies the elemental purity of samples.

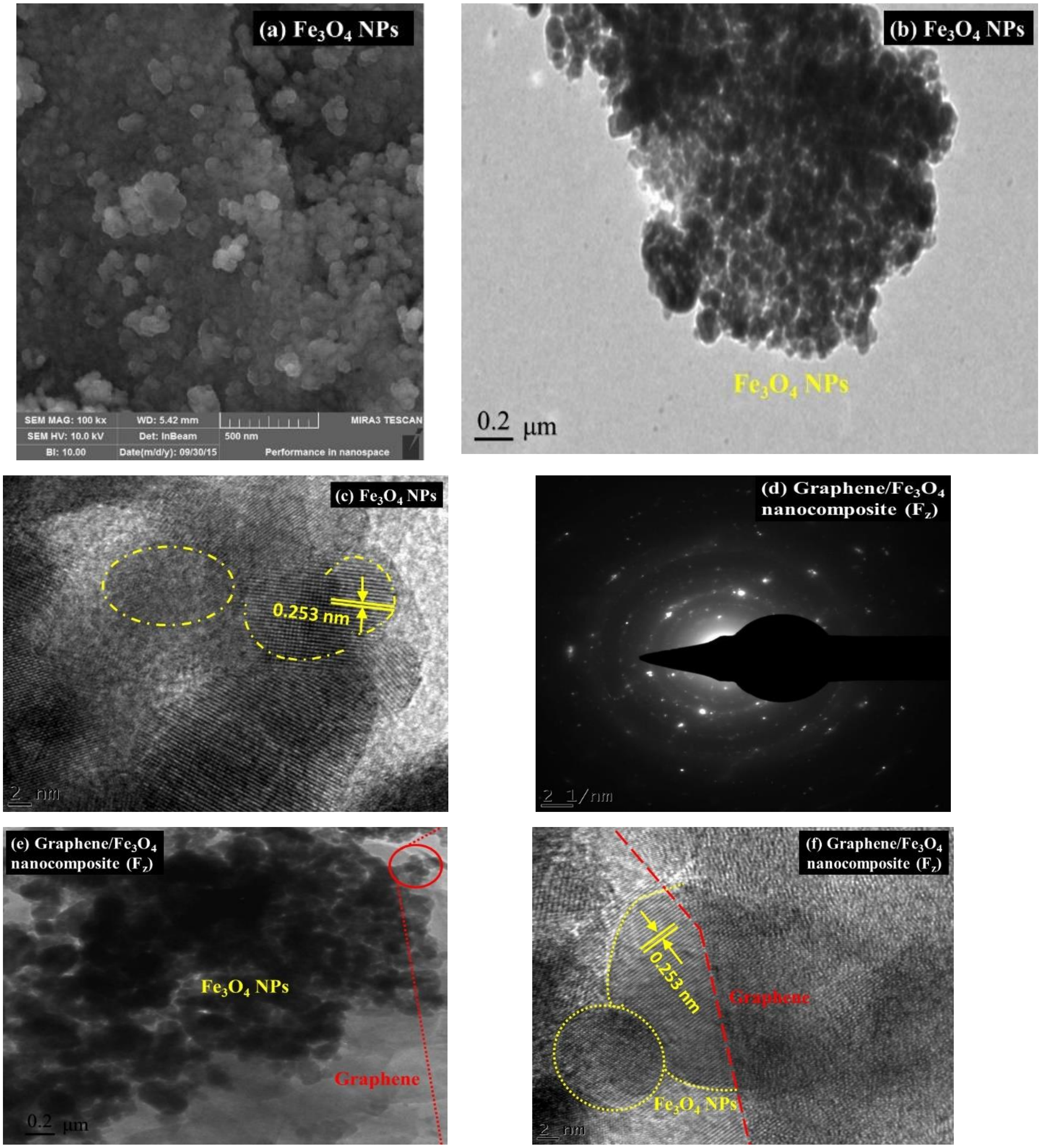

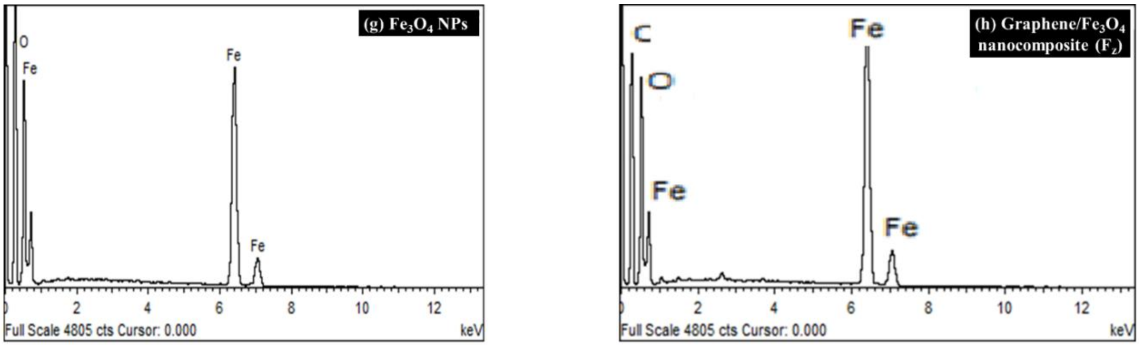

Figure 6. 2(a)-(h) SEM image of neat Fe_3O_4 NPs; scale bar is 500 nm, (b) TEM image of neat Fe_3O_4 NPs, (c) a high resolution TEM image of Fe_3O_4 NPs. The fringe spacing corresponds to (311) plane of Fe_3O_4 NPs; the scale bar is 2 nm, (d) SAED pattern of graphene/ Fe_3O_4 nanocpmposite (F_z), (e) A TEM image of graphene/ Fe_3O_4 nanocpmposite (F_z) that shows NPs on sheet, (f) a high resolution TEM image of selected portion that shows interface between graphene and Fe_3O_4 NPs, scale bar is 2 nm, (e) an EDX spectrum of Fe_3O_4 NPs, and (f) an EDX spectrum of graphene/ Fe_3O_4 nanocomposite.

6.2.2 Raman Spectroscopic Analysis

Raman spectroscopy is considered as the finger print tool for carbon nanosystems. A comparison of Raman active modes of GNPs and graphene/Fe_3O_4 nanocomposites is established in Figure 6. 3 in the range 1200 cm^{-1} to 2200 cm^{-1}. The GNPs possess two Raman active modes in this range. A weak feature (arising due to second order Raman scattering), present around 1350 cm^{-1} is disorder induced band (D-band). This low intensity band demonstrates the absence of oxygen containing functional groups thus affirming the results from XRD that the material has the high carbon purity. Whereas, in the case of graphene/Fe_3O_4 nanocomposites, the D-band becomes a prominent feature. This is ascribed to the fact that, attachment of Fe_3O_4 NPs on the sp^2 hybridized planar carbon, increases the disorder. The doubly degenerate phonon mode (E_{2g}) in GNPs expresses itself as G-band at 1587 cm^{-1}. This mode arises due to first order Raman scattering. The G-band appears at 1598 cm^{-1} and 1601 cm^{-1} in graphene/Fe_3O_4 nanocomposites, F_y and F_z respectively. The shift is associated with the charge transfer between Fe_3O_4 NPs and graphene sheets and indicates the electrostatic interaction between anchored particles and graphene. These observations state emphatically the successful attachment of magnetite NPs on graphene sheets.

The Raman spectroscopic results are coherent with the observations obtained from X-ray diffractograms.

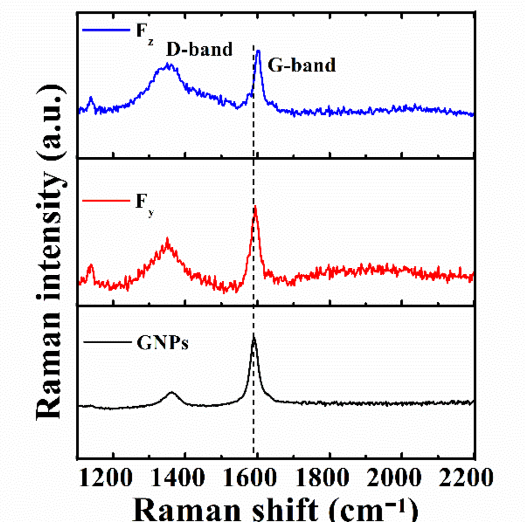

Figure 6. 3 **Raman spectra of neat GNPs and graphene/Fe_3O_4 nanocomposites**

6.2.3 Photocatalytic Activity-Photo Fenton Type Reaction

To shed light on photocatalytic performance of prepared nanomaterials, the time evolution spectra of aqueous methyl orange are presented in Figure 6. 4(a)-(c). The photo-induced dye degradation using magnetic graphene photocatalyst can be made most effective by concurrent adsorption and photo-Fenton type reaction at photocatalyst-dye solution interface. The adsorption of methyl orange on graphene/Fe_3O_4 nanocomposite is achieved by development of π-π interactions between graphene basal planes and aromatic moieties present in methyl orange. Fe_3O_4 NPs show 43% degradation efficiency, whereas the graphene/Fe_3O_4 nanocomposite F_y and F_z show 66.43% and 99.24% photodegradation of methyl orange in 30 min respectively. The digital image demonstrates the magnetic separation of catalyst after wastewater treatment. The reaction kinetics are depicted in Figure 6. 5(a) and (b). The fast and complete degradation of methyl orange is achieved by F_z nanocomposite. The rate constants are calculated using pseudo first order rate kinetics.

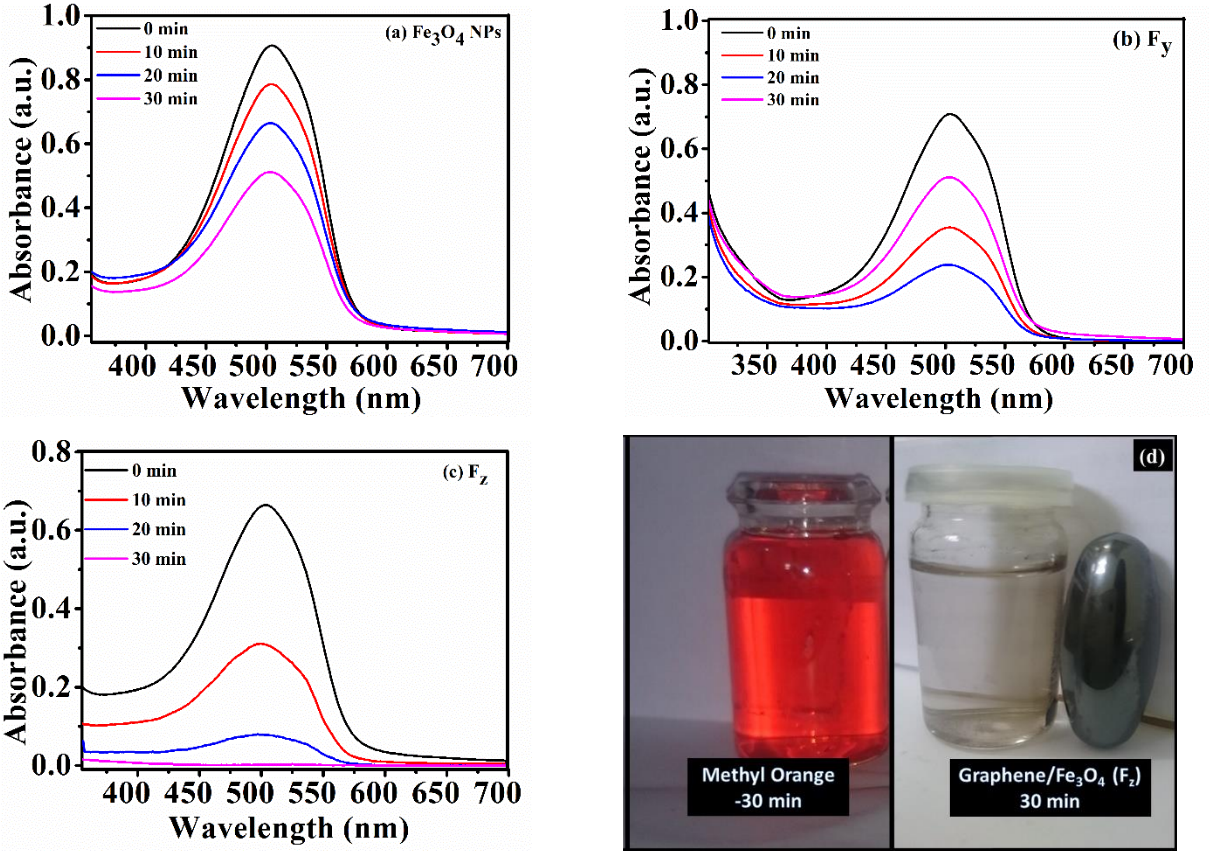

Figure 6. 4 (a)-(d) Absorbance spectra of Fe_3O_4 NPs (a), F_y (b), F_z (c), and digital image of contaminated water at the start and end of experiment for F_z nanocomposite (d)

The rate constant for Fe_3O_4 NPs ($k = 0.02\ min^{-1}$) increases significantly to $0.16\ min^{-1}$on addition of graphene in F_z nanocomposite. The photo-Fenton type reaction based mechanism is schematically outlined in Figure 6. 6. The valence band electrons are photoexcited to conduction band of Fe_3O_4 NPs. These photoexcited carriers are readily accepted by graphene layers, which provides an easy transportation channel to them. The graphene provides the active sites for adsorption of H_2O_2. The accepted electrons facilitate the conversion of adsorbed H_2O_2 to hydroxyls ($^{\bullet}OH$) and hydroperoxyls radicals ($^{\bullet}OOH$).[133, 292] Moreover, Fe^{3+}/Fe^{2+} redox iron pairs interconvert to each other in the presence of H_2O_2 molecules with the generation of hydroxyls ($^{\bullet}OH$) and hydroperoxyls radicals ($^{\bullet}OOH$).

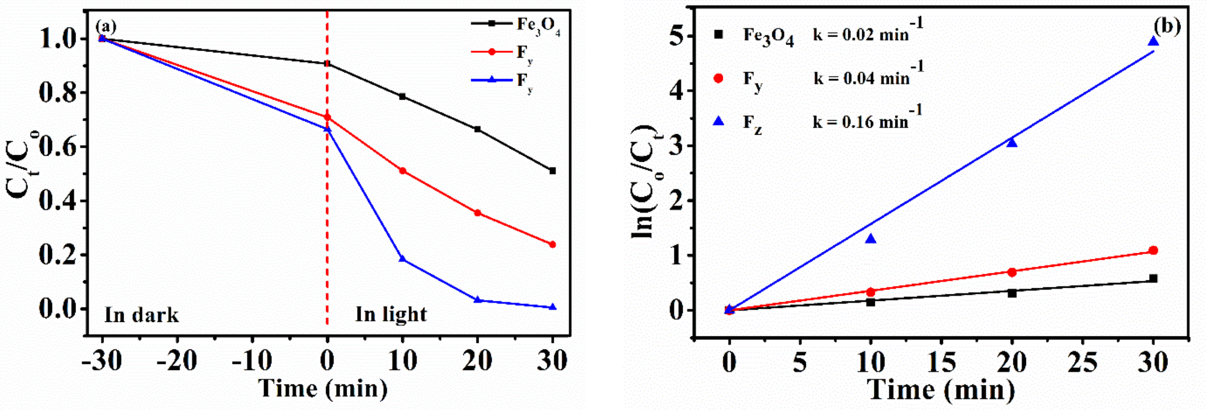

Figure 6. 5 (a)-(b) Time evolution of concentration of methyl orange solution for different samples (a), and linear fitting to data using pseudo first rate kinetics (b)

The •OH radicals possess high oxidative potentials and are excessively generated. They oxidize methyl orange with generation of H_2O and CO_2 as the final products as explained step by step in previous reports.[262, 293, 294] The chemical reactions that take place at the solid liquid interface are written mention in the Figure 6. 6.

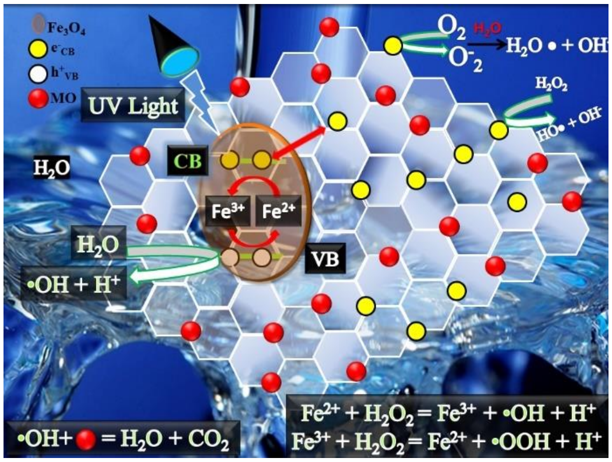

Figure 6. 6 Schematic description of methyl orange removal based on photo-Fenton type reaction

The other factors that govern the photocatalysis are further discussed in the following paragraphs. The passivation effect in Fe_3O_4 NPs is due to low number of adsorption sites and fast recombination of charge carriers. The enhancement in graphene/Fe_3O_4 nanocomposites is attributed to the synergistic effect created by both species. Firstly, graphene provides adsorption sites for dye and H_2O_2, whereas Fe_3O_4 NPs offer limited adsorption sites due to less surface area, which is one of the reason of its low degradation efficiency. The low surface area is consequence of aggregation of Fe_3O_4 NPs arising due to magnetic interactions, and can be clearly observed from Figure 6. 2(a). Secondly, graphene, being universal donor and acceptor of electrons provides conducting channels. As it is lying adjacent to Fe_3O_4 NPs, therefore the photo-excited $e^-_{CB} – h^+_{VB}$ pairs suffer a delay in their recombination. The longevity of carrier's separation favours the degradation efficiency. On the other hand, absence of graphene in Fe_3O_4 NPs leads to quick recombination, henceforth, low degradation efficiency results. Thirdly, the highly-enhanced performance of photocatalyst is also attributed to carbon purity. Photoexcited electrons' transport goes unhindered due to the absence of functional groups at the basal plane or edges of graphene as the functional groups play the role of impurity atoms.[51] This feature, endowed by graphene, makes graphene/Fe_3O_4 nanocomposite a superior material as compared to GO/Fe_3O_4 nanocomposite reported previously.[120, 133] The graphene/Fe_3O_4 nanocomposite shows much improved photo Fenton type discoloration of methyl orange with less amount (0.2 g/l) in comparison with Fe_3O_4/carbon nanotube composite where methyl orange was completely removed by much larger amount (2.9 g/l) of photocatalyst, in a previous study.[295]

The stringent economic demands make the reuse of photocatalyst inevitable. The reusability tests are therefore essential for the regular use of photocatalyst. The recyclability performance of both Fe_3O_4 NPs and graphene/Fe_3O_4 nanocomposite was tested for consecutive five cycles. It is demonstrated in Figure 6. 7 that there is negligible loss in photocatalytic activity of graphene/Fe_3O_4 nanocomposite (F_z). The graphene/Fe_3O_4 nanocomposite shows excellent stability even after five continuous cycles of activity, whereas the photodegradation efficiency of Fe_3O_4 NPs is greatly reduced after five cycles of reusability.

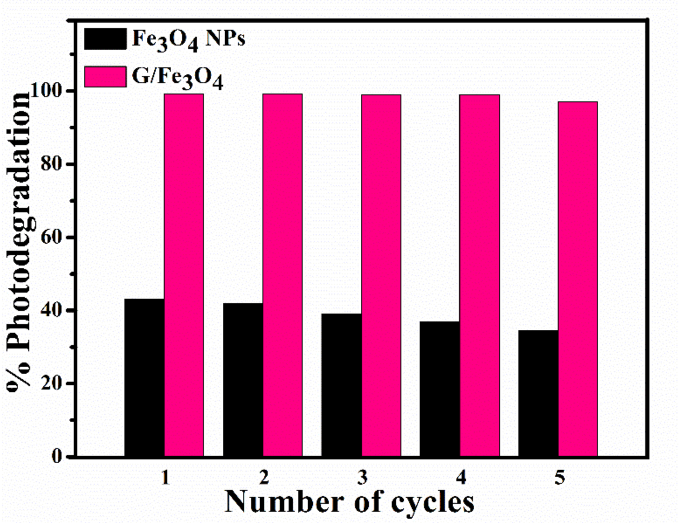

Figure 6. 7 A comparison of recyclability performance of Fe_3O_4 NPs and F_z nanocomposite

6.2.4 Magnetic Properties and Inexpensive Separation

The economic constraints make it inevitable to design a photocatalyst that can be separated from water in the fast and inexpensive way. Magnetic separation of photocatalyst offers the cost-effective solution to meet the economic requirements. To highlight the magnetic nature of Fe_3O_4 and graphene/Fe_3O_4 nanocomposite (F_z), we investigated the prepared materials using vibrating sample magnetometer (VSM). The variation of room temperature magnetization is studied as a function of applied magnetic field (M-H hysteresis loop), sweeping from -9500 Oe to 9500 Oe is presented in the Figure 6. 8. The saturation magnetization for Fe_3O_4 NPs and graphene/Fe_3O_4 are 34 emu/g and 29 emu/g respectively. The remanence of Fe_3O_4 NPs and graphene/Fe_3O_4 are 3.515 emu/g and 2.98 emu/g respectively. The coercivity is presented by the inset in Figure 6. 8. The obtained values are 89.62 Oe and 44.2 Oe for Fe_3O_4 NPs and graphene/Fe_3O_4 nanocomposite (F_z)

respectively. On addition of graphene, the saturation magnetization decreases, which agrees with the previous study [291]. Following the above discussion, it can be ensured that the magnetic separation of graphene/Fe_3O_4 nanocomposite (F_z) from water is an additional advantage of this photocatalyst.[296]

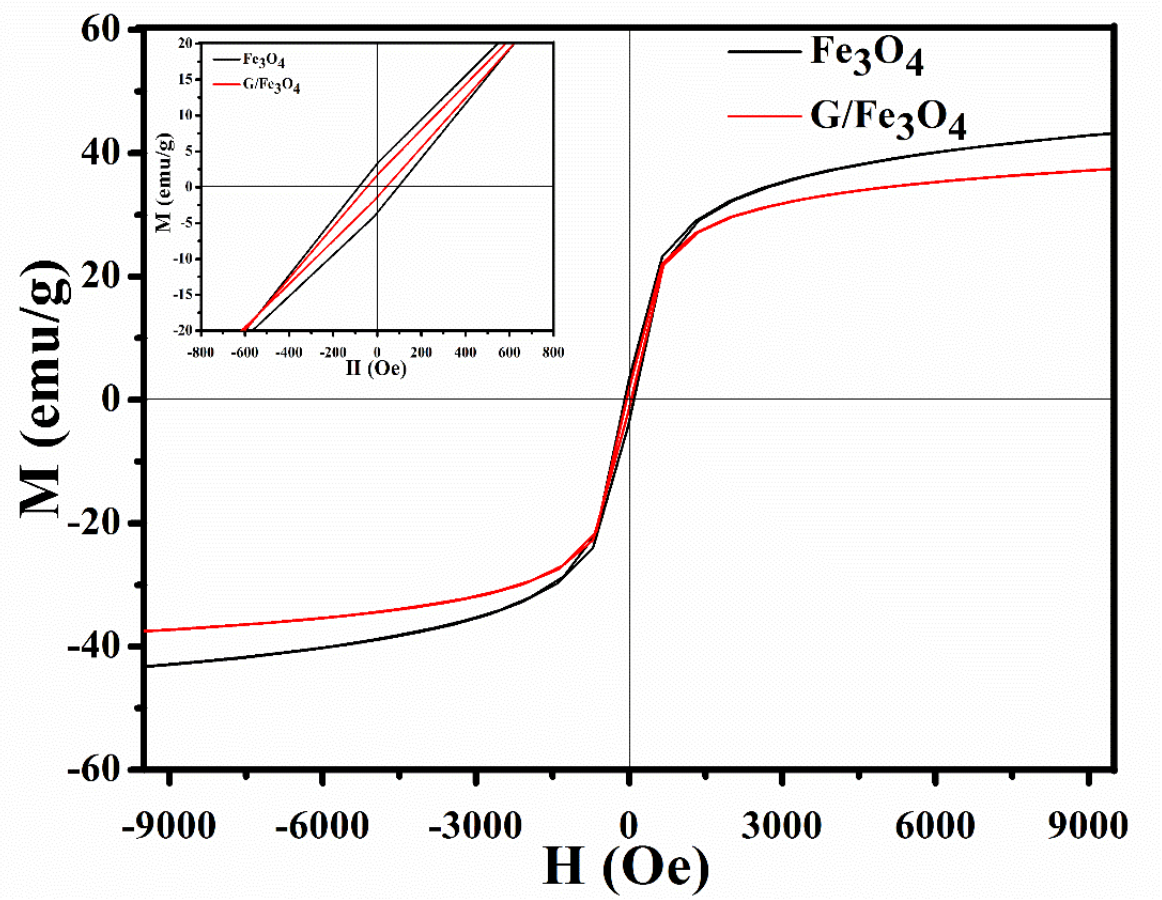

Figure 6. 8 Magnetic behaviour of graphene/Fe_3O_4 (F_z) nanocomposite

By the application of a small magnet, it takes 7 seconds only (in Figure 6. 4(d)), therefore, it can be inferred that magnetic separation of graphene/Fe_3O_4 nanocomposite can be easily executed in the fast and inexpensive way. In the light of obtained results, graphene/Fe_3O_4 nanocomposite meets the stringent economical requirements and may be recommended as an efficient and cost-saving alternative of traditional photocatalysts.

6.2.5 Antibacterial Activity

We have investigated antibacterial performance of prepared nanocomposites for *E. coli*, *P. aeruginosa*, and *S. aureus*. The optical density at 600 nm was obtained at different intervals during incubation period of 24 h. The cell viabilities and growth inhibition rates were obtained.

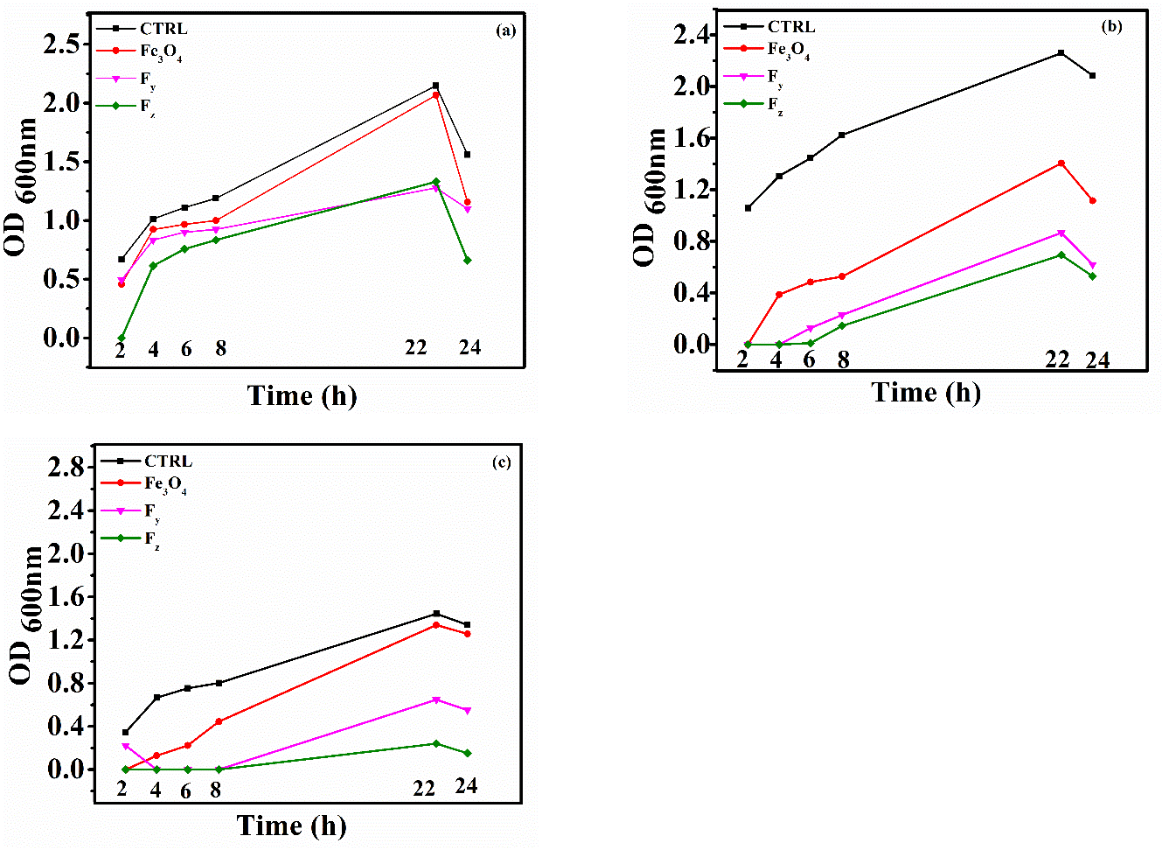

Figure 6. 9 Growth profiles of bacteria from 2 h-24 h in presence of prepared materials.

Figure 6. 9(a)-(c) elaborate the antibacterial performance of prepared nanocomposites against different bacterial strains.

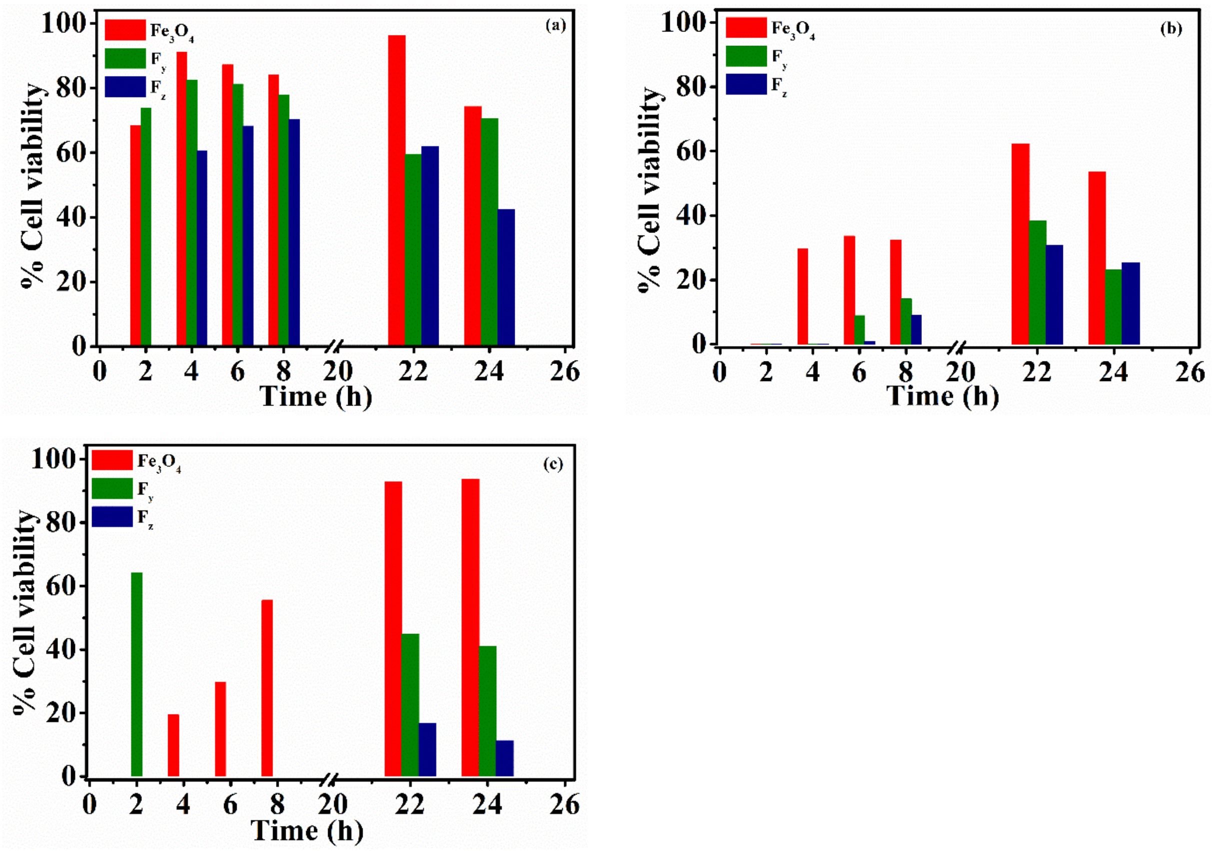

Figure 6. 10 Cell viabilities of different bacterial strains

The % growth inhibitions so obtained are tabulated in Table 6. 1.

Table 6. 1 Growth inhibition of *E. coli*, *P. aeruginosa*, and *S. aureus* obtained by Fe_3O_4, F_y and F_z

Bacteria	**Growth inhibition by Fe_3O_4 NPs**	**Growth inhibition by F_y nanocomposite**	**Growth inhibition by F_z nanocomposite**
E. coli	16.5 %	26%	49.5%
P. aeruginosa	64.8%	84%	89.02%
S. aureus	51.5%	75%	95.33%

These results show that the antibacterial performance of magnetite is significantly enhanced after the inclusion of graphene. Graphene based nanomaterials have been recently explored for their antimicrobial activity.[94, 297] Many of mechanisms have been suggested to explain the bactericidal and bacteriostatic properties of graphene nanocomposites that are oriented on the effects created by either one or the other or both components of the nanocomposites. However, a unified and exact mechanism is still lacking. Here, we briefly discuss to establish the underlying mechanism for antimicrobial activity of graphene/Fe_3O_4 nanocomposite.

The one of the evident mechanisms, that get support from SEM and TEM images obtained during exposure of bacteria to graphene based nanomaterials is the direct contact between the them. It was suggested that the sheet edges behave like cutters to rupture the outer layer of bacteria that subsequently leads to leakage of cytoplasmic content and ceases the normal cell function. The disintegration of bacterial outermost layer has been observed previously [97, 153]. The size dependent internalization of graphene nanostructures may also lead to cell damage [244, 298]. At the same time, metal oxide loaded graphene contribute to release metal ions around cell boundary. The increased localized concentration of these ions followed by their internalization (e.g., iron ions in our work) induces cell death.[95]

Further, the evaluation of biochemical changes that take place during bacterial inactivation reveal in a previous study that protein degradation brings drastic changes in bacterial viability. The cellular proteins (in case of *E. coli*) reduce significantly, when treated with graphene/Fe_3O_4 nanocomposite, as compared to neat graphene or magnetite. This study also showed explicitly that oxidative stress is also responsible for the considerable reduction in number of viable bacterial cells [97]. The oxidative stress originates due to individual or combined contribution of metal oxide and graphene. It is reported that excessive production of reactive oxygen molecules increases the oxidative stress inside cell, that subsequently impairs the normal bacterial activity.[96]

In the light of above discussion, we believe that graphene and Fe_3O_4, synergistically induce various features that are fatal to bacteria. However, the differential cytotoxicity as seen from Table 01, may be due to the two reasons. Firstly, the membrane's isoelectric points for Gram negative and Gram positive bacteria are different. The graphene based materials when meet the bacterial surface, a Schottky barrier is formed between membrane's respiratory proteins and conducting graphene's surface.[92] The difference of charge transfer between the two, may account, in part, for the differential cytotoxicity observed in our findings. Secondly, the difference in chemical composition of bacterial outermost boundaries may also be considered as a reason for difference in bacterial inhibitory activity.[299]

6.3 Summary

Ultra violet light driven photocatalyst graphene/Fe_3O_4 nanocomposites are synthesized and characterized. The nanocomposite (F_z) developed with intention to utilize synergistic effects created by graphene and Fenton type reaction in the presence of UV light, achieves the excellent photocatalytic performance with 99.24% degradation of methyl orange in 30 minutes. Graphene loaded with Fe_3O_4 NPs shows outstanding dye removal efficiency owing to good adsorption properties, donor acceptor nature of graphene, narrowed bandgap energy, H_2O_2 induced interconversion of ferrous and ferric ions, and delayed carriers' recombination. Our findings greatly recognize graphene/Fe_3O_4 nanocomposite for its utilization towards low cost waste water treatment. The nanocomposite (F_z) also shows significant control over bacterial growth and stops 89.02% and 95.33% growth of *P. aeruginosa* and *S. aureus*. The antibacterial performance is a consequence of interplay of properties of both Fe_3O_4 and graphene in a coherent way.

Chapter No. 7

7. Synthesis, Characterization, and Applications of NiO/Graphene Nanocomposites

Overview:

Graphene/NiO nanocomposite can be an innovative material to achieve complete pathogen control alongside being an economic solution for water treatment. In this chapter, characterization results, solar light induced dye removal and bactericidal properties of nickel oxide (NiO) and graphene nanoplatelets (GNPs) nanocomposites are presented.

7.1 Introduction

The wastewater discharge from textile dyeing industries is a source of 17-20% water pollution.[300] Therefore, this environmental challenge essentially demands the removal of dyes before the discharge of textile effluent into waterbodies. To this end, it is attractive to use solar light in cleaning process of water, due to its natural and unlimited availability. To address water pollution, the results presented in last few chapter are good to some extent. However, the importance of low cost water treatment cannot be denied. Also, health issues arising due to pathogenic bacteria raise the major concerns due to high mortality rate across the globe. The antibacterial results obtained in previous chapters show the bacteriostatic effect of nanocomposites only. It is highly desirable to prepare novel materials that have bactericidal effects. Keeping in view these findings, graphene/NiO nanocomposites were selected to study their photocatalytic and antibacterial properties.

The widely-studied material, NiO finds applications in lithium ion batteries,[301-303] and catalysis.[304-307] The photocatalytic application of NiO or modified NiO, opens new avenues to clean the contaminated water.[308-311] The photocatalytic performance of a nanomaterial is primarily determined by the interplay between its optical bandgap energy, its surface area, and trapping of photo generated charge carriers. Although, a low-cost nanomaterial, but neat NiO is not favoured as an efficient photocatalyst due to its wide bandgap, and quick recombination of photo-generated charge carriers. These shortfalls, generally observed in neat metal oxides, can ideally be addressed by inclusion of graphene based nanostructures, where properties of individual components play role for the enhancement in photocatalytic and medicinal activity.[83, 90, 98, 262, 312-315] This is due to following factors. First, the surface area of composite material is usually higher than neat metal oxide, and therefore, provides numerous sites for adsorption of photocatalyst. Second, introducing graphene in the composite material along with wide bandgap nanomaterials (like NiO) tailors the redshift in bandgap energy, which may favour efficient photocatalysis.[86, 280, 316] Third, an intrinsic feature of graphene e.g., its conductivity streamlines the flow of electrons from conduction band of metal oxide to graphene.[133] Nanocomposites with all these features are believed to display robust photocatalytic activity.[281, 282, 317]

Water contamination is also caused by multidrug resistant pathogenic microorganisms that are fatal for human beings. The high mortality rate around the globe worsts the situation and makes it essential to find alternate solutions to replace ineffective traditional antibiotics by development of novel methods to encounter antibiotic resistant bacteria.[93] The conventional water disinfectants results in formation of carcinogenic by-products, which is another disadvantage.[318] Keeping in view these harmful aspects, it is inevitable to design new strategies for a complete pathogen control. As discussed in previous chapters, antibacterial performance of graphene based nanocomposites may depend on various factors like morphology, ability to produce reactive oxygen species, conductivity, and their composition.[173, 175] But since a 100% eradication of bacteria was not achieved in our previous work, presented in last three chapters, therefore, considering these factors, we envisage to design a bactericidal nanomaterial (constituted by NiO and graphene) with an aim to utilise the antibacterial features of both NiO and graphene in a combined fashion for bacterial growth inhibition.

This work aims to study the effect of graphene on photocatalytic properties of NiO nanoflakes to degrade methyl orange. This carcinogenic azo dye can be metabolized into potentially harmful products, if ingested.[319, 320] The work is targeted to find a cost-effective dye-removal method that meets the stringent economical requirements. Moreover, the complete growth inhibition of pathogenic microorganisms, *Escherichia coli* (*E. coli*), *staphylococcus aureus* (*S.*

aureus), and *Pseudomonas aeruginosa* (*P. aeruginosa*) using NiO and graphene nanocomposite is reported for the first time in this work.

7.2 Results and Discussions

7.2.1 Structural and Morphological Analysis

To discuss the crystallography of prepared samples, the X-ray diffractograms obtained between 10°-80° are analysed in Figure 7. 1. The peaks located at 37.14°, 43.32°, 62.9°, 75.4°, and 79.34° are assigned to reflections from (111), (200), (220), (311), and (222) planes of NiO respectively. These results indicate the presence single phase NiO (cubic, a = b = c = 4.1769 Å, α = β = γ = 90°). The absence of impurity peaks eliminates the presence of $Ni(OH)_2$ and other crystalline phases. These results agree well with JCPDS No. 00-004-0835. All the nanocomposites show an additional peak at 26.4° (002), which depicts the presence of graphene. The absence of peak at 10° manifests the carbon purity in the samples. The (200) peak of NiO broadens in graphene/NiO nanocomposites. This is associated with smaller crystallite sizes. The crystallite size for NiO, N_y and N_z nanocomposites are 25 ± 0.3 nm, 18.2 ± 0.25 nm, and 14.1 ± 0.05 nm respectively. These results corroborate with previous studies.[321-323]

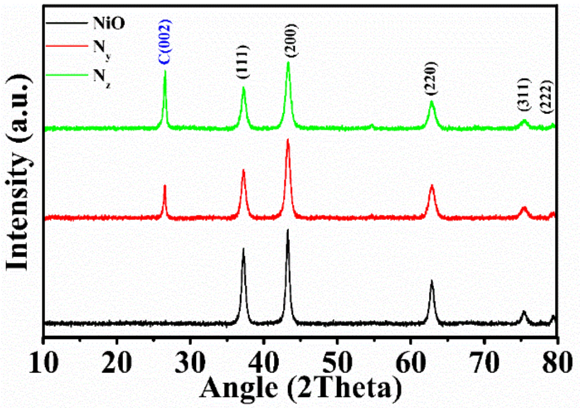

Figure 7. 1 The X-ray diffractograms depict the presence of graphene and (or) NiO in the samples

The investigations on morphology and microstructure are presented in Figure 7. 2.

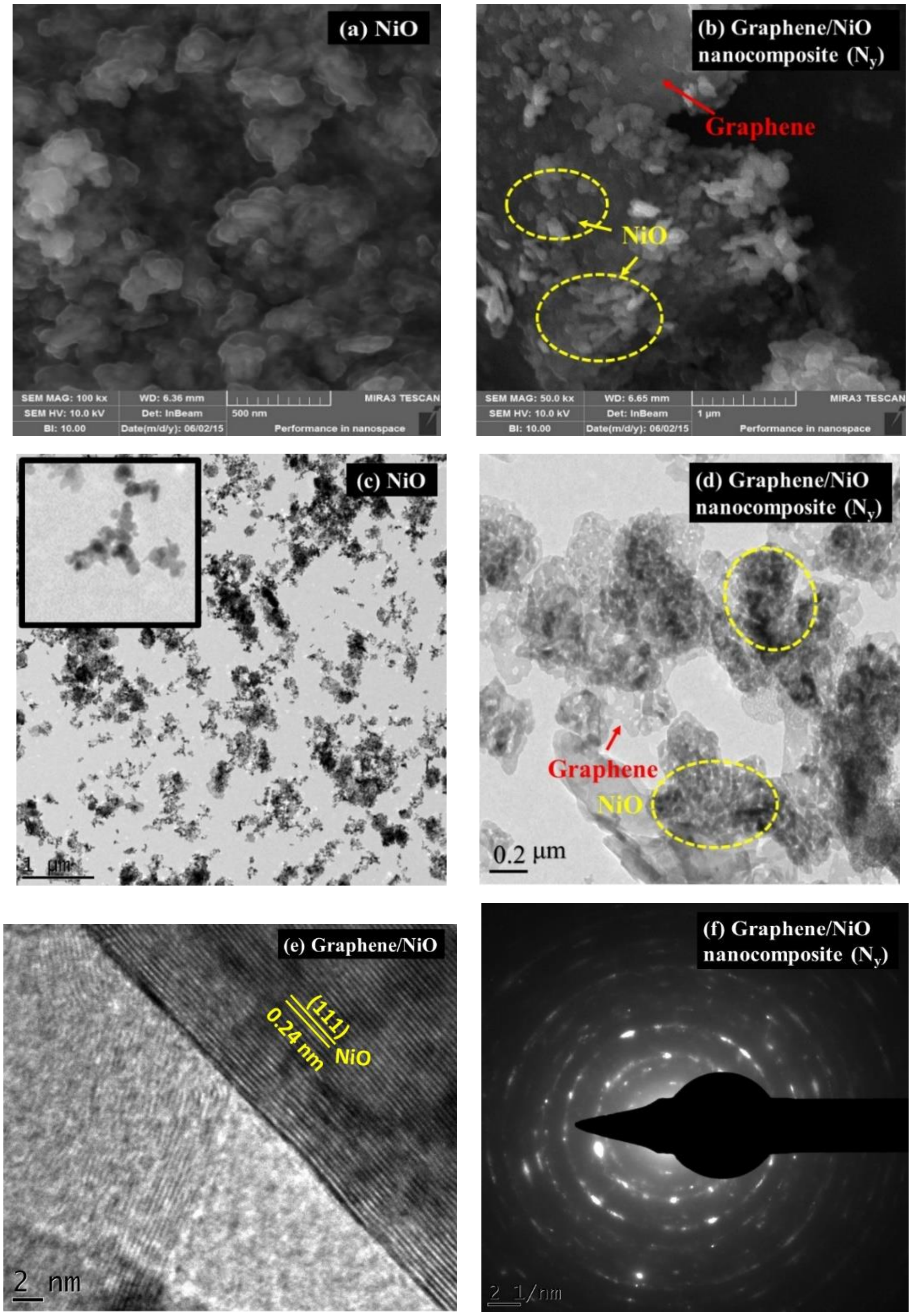

Figure 7. 2 (a)-(f) (a) The SEM micrograph of NiO nanoflakes; scale bar is 500 nm, (b) NiO nanoflakes grafted graphene obtained from SEM, shows the two distinct components of nanocomposite; scale bar is 1 µm, (c) TEM image of NiO nanoflakes. The inset is the enlarged view of NiO; scale bar is 1 µm, (d) TEM image shows sheet like structure of graphene with distributed NiO nanoflakes (marked as yellow region) over the entire surface; scale bar is 0.2 µm, (e) HR-TEM image of NiO nanoflake attached to graphene, and (f) SAED image of graphene/NiO nanocomposite (N_y).

NiO shows flakes like morphology shown in Figure 7. 2(a) and Figure 7. 2(c). The flakes like structures of NiO seems to be composed of many primary particles.

In nanocomposite form, the presence of graphene affects the growth of NiO on it. The well-defined nanoflakes are observed in Figure 7. 2(b). However, the primary particles are not seen in graphene NiO nanocomposite. The flakes like structures of NiO attached on graphene sheets have densely covered the graphene sheets. The TEM image is presented in Figure 7. 2(d). The graphene sheets with embedded NiO nanoflakes on its surface are shown. The graphene sheets have homogeneous distribution of NiO nanoflakes. The morphological details confirm the bi-phase nature of prepared nanocomposites. A high resolution TEM image in Figure 7. 2(e) reveals the distance between two adjacent planes of NiO nanocrystal. The marked distance corresponds to (111) plane of NiO. The X-ray diffraction results show an excellent coherence with SAED pattern presented in Figure 7. 2(f). The presence of carbon and NiO in nanocomposite is demonstrated by the designation of diffraction rings to respective planes (see Figure 7. 2(f)).

7.2.2 Raman Spectroscopic Analysis

To further investigate NiO and graphene/NiO nanocomposites, the samples are characterized by Raman spectroscopy. Raman spectroscopy is an informative tool to probe carbon nanostructures. It provides deep insight to distinguish between different species of nano-carbon. The two prominent features that play role in the identification of formation of graphene nanocomposites are the G-band and D-band. The doubly degenerate (LO and iTO) phonon modes originate as G-band due to first order Raman scattering in graphene as seen in Figure 7. 3. The D-band appears due to second order Raman scattering process.[190] The variation in these features gives the direct evidence of the formation of nanocomposites by a previous study. [324, 325]

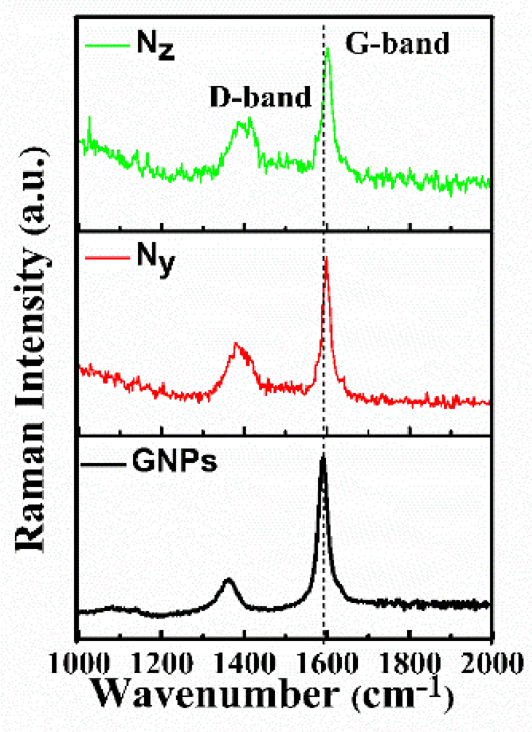

Figure 7. 3 Raman active modes of graphene nanoplatelets (GNPs) and NiO grafted graphene nanocomposites.

The primary feature that indicates formation of nanocomposite is G-band, which shifts up to 16 cm^{-1} with new peak position at 1602 cm^{-1}, whereas, this band is located at 1586 cm^{-1} in graphene nanoplatelets. This shows that the electrical charge transfer between the graphene sheets and NiO nanoflakes has taken place, which contributes towards attachment effect between the two species. It is also noteworthy that the D-band (located ≈ 1357 cm^{-1}) has become broader and its intensity in NiO/graphene nanocomposites is higher than that of graphene nanoplatelets. This proves the presence of significant number of defects in graphene nanocomposites. These defects arise due to attachment of NiO nanoflakes to graphene sheets. The Raman spectroscopic measurements are supported by a previous study.[324, 325]

This proves the presence of significant number of defects in graphene nanocomposites. These defects arise due to attachment of NiO nanoflakes to graphene sheets. The Raman spectroscopic measurements obtained here are supported by a previous study. [324, 325]

7.2.3 Photocatalytic Activity

In this study, all samples are subjected to solar light initiated catalytic process for photo-induced degradation of methyl orange.

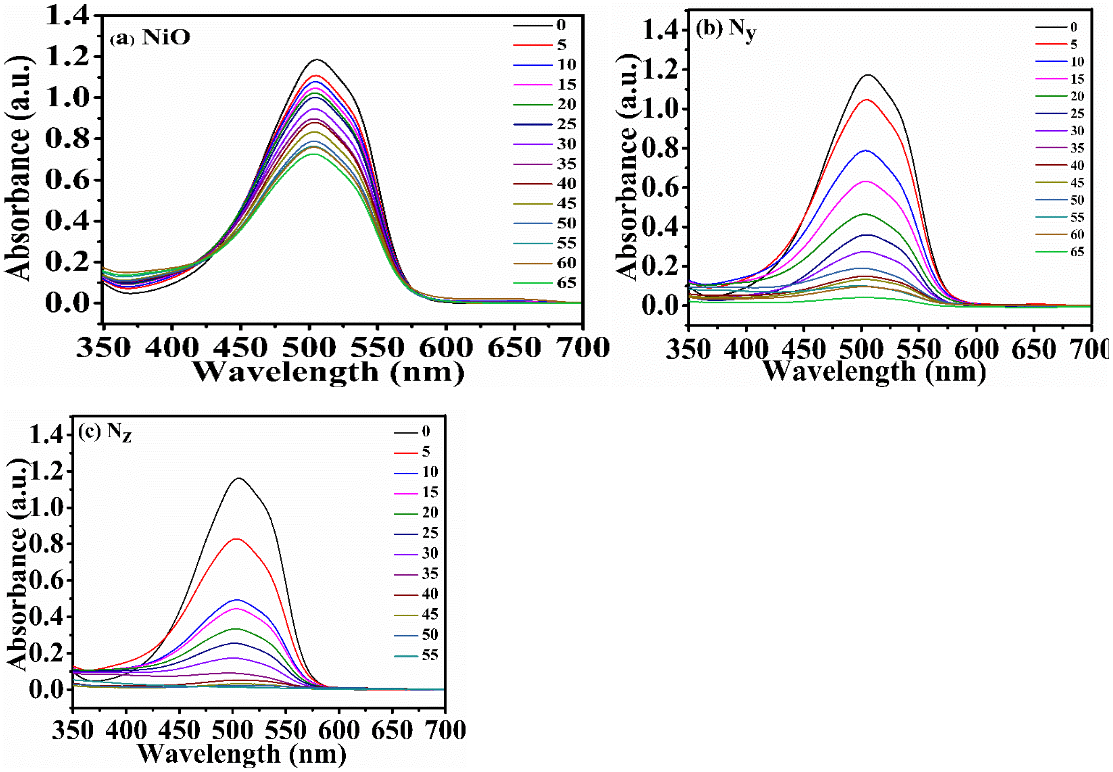

Figure 7. 4 (a)-(c) Time evolution of absorbance spectra of methyl orange for (a) NiO, (b) graphene/NiO nanocomposite (N_y), and (c) graphene/NiO nanocomposite (N_z). The time is recorded in minutes

The time evolution of absorbance spectra of methyl orange solution in the presence of NiO and graphene NiO nanocomposite show that it goes nearly to zero for N_z in 55 min only, whereas zero absorbance is not achieved even after 65 minutes for NiO and N_y (see Figure 7. 4(a)-(c)). The detailed analysis of experimental findings is shown graphically in Figure 7. 5(a)-(d). The variation in concentration as a function of time, plotted in Figure 7. 5(a), shows degradation of dye. To investigate the rate kinetics of the reactions, pseudo first order kinetics were used. The following expression is used to determine the apparent rate constants, $\ln (C_o/C_t) = kt$. Here C_o and C_t are concentrations of aliquots at $t = 0$ and other times, and k is the apparent rate constant. The apparent rate constants for reactions are determined by linearly fitting the quantity $\ln(C_o/C_t)$ as a function of time. The fitting parameters so obtained show that apparent rate constant varies significantly with increase in GNPs content. The apparent rate constant shows the increase of an order of magnitude, on addition of GNPs. The values of k are detailed in the Figure 7. 5(b). The NiO and N_y degrade upto 36% and 91.8% methyl orange in 55 min, whereas N_z exhibits highest degradation efficiency and removes 99% methyl orange with highest apparent rate constant ($k = 0.08 \text{ min}^{-1}$). The excellent photocatalytic performance of graphene NiO nanocomposite N_z is due to appropriate graphene content in the nanocomposite.

To obtain the deeper insight of process, the mechanism is presented in the schematic layout as shown in Figure 7. 6. A higher surface area of nanocomposite N_z (see Table S 7. 1) promotes the higher adsorption of dye molecules on its surface. The incident sunlight excites the valence electrons of attached NiO nanoflakes. These electrons populate the conduction band leaving behind holes. The excited electrons are readily accepted by graphene sheets that lie adjacent to NiO nanoflakes. The high electrical conductivity of graphene provides a conducting network and endows the delay to charge carriers’ recombination in NiO. Consequently, charge carriers are used for oxidation of dye. The electrons and holes are used to generate reactive oxygen species. The reactive oxygen species play the vital role to alter the ring structure of methyl orange. The production of various intermediates[238] ultimately results into complete mineralization of methyl orange as explained previously in one of our work.[262] The result is dye-free solution with end products H_2O and CO_2.

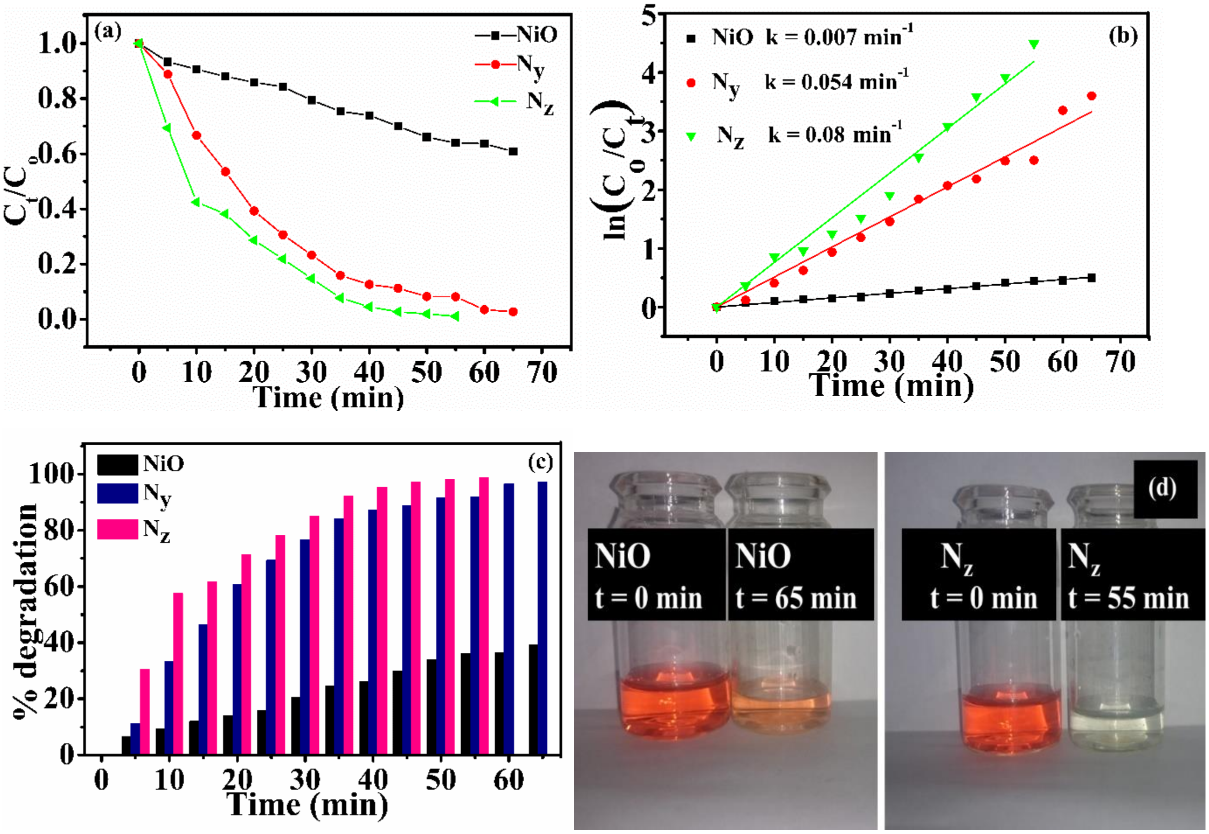

Figure 7. 5 (a)-(d). (a) and (b) pseudo first order kinetics of photocatalytic reaction, (c) the photodegradation efficiencies of NiO, N_y and N_z, and (d) an optical image of methyl orange degradation using NiO and N_z.

The exceptionally high photocatalytic activity of N_z nanocomposite is due to synergistic effects created by lowest bandgap energy, highest BET surface area, and conducting graphene network. It is noteworthy that NiO nanoflakes show very low photocatalytic activity, due to rapid deexcitation of electrons into valence bands. Electronic trap in the form of graphene is not available in this case. Only a few electrons can get trapped in defect states of NiO. This makes electrons and holes unavailable for generation of sufficient number of reactive oxygen species. Other factors that accounts for low photo-degradation performance of NiO are its comparatively higher bandgap energy and low surface area. A higher optical bandgap energy of NiO is responsible for slower photoexcitation of carriers as compared to N_z. A low surface area of NiO results in less adsorption of methyl orange during the process. Subsequently, neat NiO gives much lower photodegradation efficiency. The chemical reactions that take place at the solid-liquid interface are depicted below.

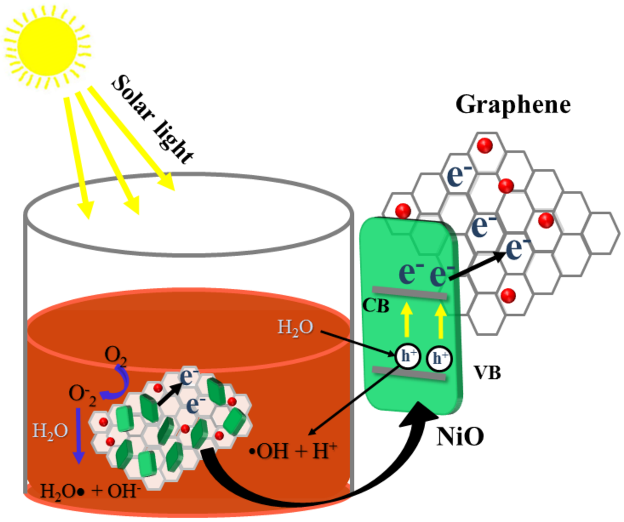

Figure 7. 6 The schematic layout of reaction taking place at nanocomposite and methyl orange interface. The adsorbed methyl orange is presented by orange spheres.

$$NiO - graphene + h\nu \rightarrow NiO(h_{VB}^{+}) + graphene(e_{CB}^{-}) \tag{7.1}$$

$$NiO(h_{VB}^{+}) + (H_2O \rightarrow H^{+} + OH^{-}) \rightarrow NiO + H^{+} + \bullet\, OH \tag{7.2}$$

$$graphene(e_{CB}^{-}) + O_2 \rightarrow graphene + O_2^{-} \tag{7.3}$$

$$O_2^{-} + 2(H^{+} + OH^{-}) \rightarrow H_2O^{\bullet} + 2OH^{-} \tag{7.4}$$

$$\bullet\, OH + methyl\ orange \rightarrow intermediates \rightarrow H_2O + CO_2 \tag{7.5}$$

The formation of intermediate chemical compounds during photodegradation of methyl orange is presented step by step in Figure 7. 7.

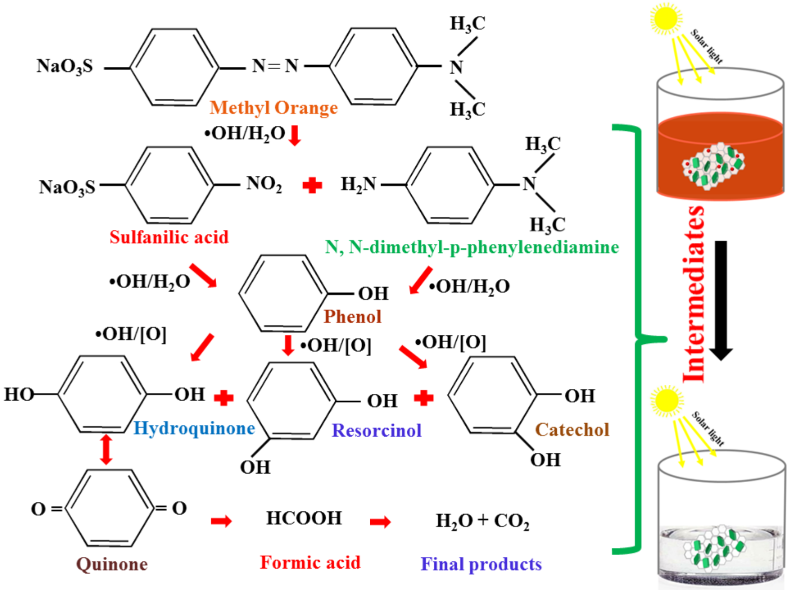

Figure 7. 7 A detailed description of formation of chemical intermediates during photodegradation of methyl orange.

It is hydroxyl species that attack the ring structure of azo dye. The intermediates that are formed include sulfanilic acid, N, N-dimethyl-p-phenylenediamine which are subsequently converted to 4-phenolsulfonic acid sodium salt and 4-dimethylaminophenol respectively (not shown). Later, their conversion to phenol results into water and CO_2 in presence of reactive oxygen species.[238, 239] This results complete degradation of dye.

A photocatalyst can be used practically if it meets the economical requirements. The prepared nanocatalysts can be activated in solar light, which reduces the cost of water cleaning process. The cost can further be controlled if photocatalyst is recyclable. We, therefore, conducted re-usability experiments using sample N_Z. It was repeatedly washed and reused to test its cleaning performance for four cycles. It is found that N_Z remains extraordinarily stable for four cycles. A negligible decrease in the photodegradation efficiency is observed. The results are presented in Figure 7. 8.

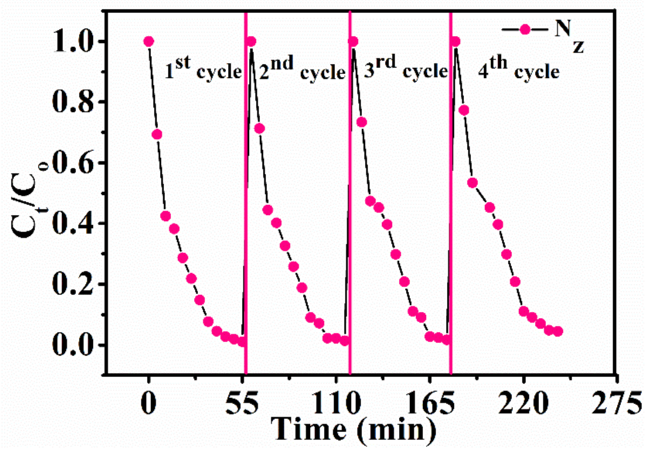

Figure 7. 8 Recyclability performance of N_z nanocomposite. The photocatalyst shows good stability for 4 cycles

It can be concluded that NiO nanoflakes grafted graphene nanocomposite with appropriate ratio of graphene and NiO, i.e., N_z is the ideal candidate for cleaning dye-polluted water. This nanocomposite provides an economic solution to decontaminate water due to its ultra-high performance in the presence of sunlight and outstanding re-usability.

7.2.4 Bactericidal Properties

To study the impact of graphene NiO nanocomposites on growth inhibition of Gram positive and Gram-negative bacteria, the antibacterial properties were evaluated using a series of nanocomposites with varying graphene content. The growth profiles of bacteria in the presence and absence of NiO and its nanocomposites with graphene are presented in Figure 7. 9(a)-(c). The results show that antimicrobial activity of NiO increases with the addition of graphene content. The growth of *E. coli* was inhibited 39.93% and 92.9% by NiO and N_y respectively whereas N_z showed bactericidal effect and completely stopped the bacterial growth from 2–24 h. The response of prepared samples was also tested against *P. aeruginosa*.

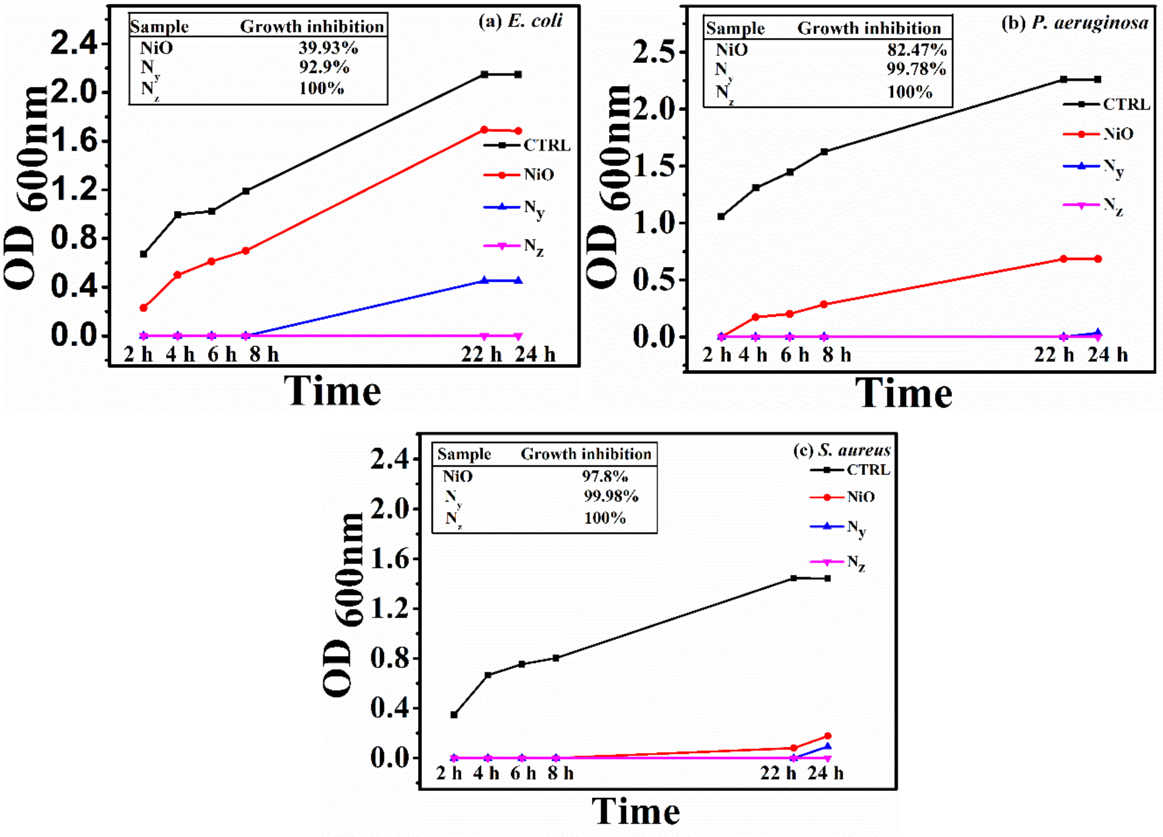

Sample	Growth inhibition
NiO	39.93%
N_y	92.9%
N_z	100%

Sample	Growth inhibition
NiO	82.47%
N_y	99.78%
N_z	100%

Sample	Growth inhibition
NiO	97.8%
N_y	99.98%
N_z	100%

Figure 7. 9 (a)-(c). The growth profiles of (a) *E. coli*, (b) *P. aeruginosa*, and (c) *S. aureus*. Complete pathogen control is achieved by N_z nanocomposite.

It was observed that NiO and N_y stopped 82.47% and 99.78% growth. The growth of *P. aeruginosa* was completely inhibited by sample N_z. The antibacterial response of samples NiO and N_y against Gram positive bacteria, *S. aureus* is 97.8% and 99.98% growth inhibition. Sample N_z showed complete growth inhibition and *S. aureus* showed no growth during experiment. The cell viabilities are presented by bar graphs in Figure 7. 10. These results show that the NiO and graphene nanocomposite with optimum graphene content, shows bactericidal effect and 100% pathogen control is achieved.

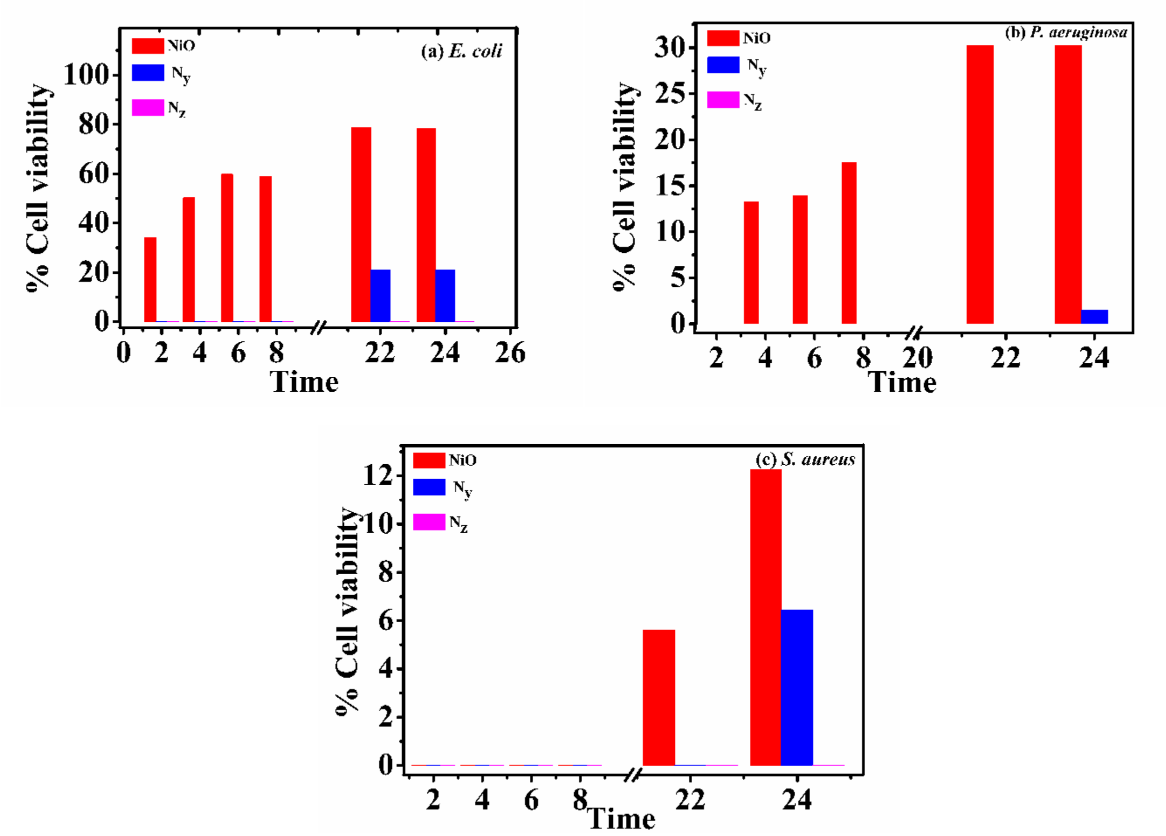

Figure 7. 10 (a)-(c). A comparison of bacterial cell viabilities on treatment with NiO and graphene/NiO nanocomposites.

The exact mechanism of antibacterial properties of graphene nanocomposite is controversial and not yet established. A number of mechanism have been proposed that account for toxicity of graphene or its nanocomposites, however an exact explanation is still unknown.[93, 297]

Here, a brief overview of possible mechanisms is given. For metal oxides and graphene nanocomposites, it is proposed that impairment of proteins caused by either metal oxides alone or metal oxides/graphene combinedly leads to bacterial inactivity. As in the case of graphene Fe_3O_4 nanocomposite, it was proved with evidence (Ellman's assay) that proteins agglomeration leads to its dysfunction. Consequently, the bacteria lose their activity. The effect is augmented for graphene

Fe_3O_4 nanocomposite as compared to Fe_3O_4 alone.[97] In our case, we believe that NiO attached graphene can have a similar activity against the bacteria.

Another mechanism, that was established using computational modelling (by first principles)[326] and experiments, asserts that membrane rupture results the cell death when graphene sheets encounter bacterial surface.[162, 176] The edges of graphene act as sharp cutters. However, it was established that the membrane disruption is dependent on size of graphene sheets.[162] Membranes disintegration can also be followed by internalization of nanostructures, which causes damage to bacteria. The wrapping of wrinkled sheets is another reason that can isolate bacteria from nutrients and it proves to be fatal for them.[159] In addition, metal oxides are also known to damage the cell membranes and so their composites with graphene. It has been proposed that the release of metal ions (M^+) by metal oxide results in increased localized concentration, which may cause pitting on bacterial surface, with subsequent leakage of cytoplasmic content from cell.[95] Intimate contact between graphene sheets and metal ions synergistically induce bacterial apoptosis.

Many of recent experiments substantiate generation of reactive oxygen species which may be the consequence of aforementioned mechanisms.[153] However, it is suggested in another work that graphene establishes conductivity dependent cytotoxicity. The charge transfer between graphene and bacterial membranes leads to charge imbalance on bacterial surface with subsequent generation of reactive oxygen species.[92] The induced oxidative stress leads to bacterial apoptosis.

In the light of discussion presented above, we believe that synergistic effect created by edge stress of graphene, accumulation of Ni^{2+} ions on bacterial surface and protein impairment leads to bactericidal activity observed in our findings.[96]

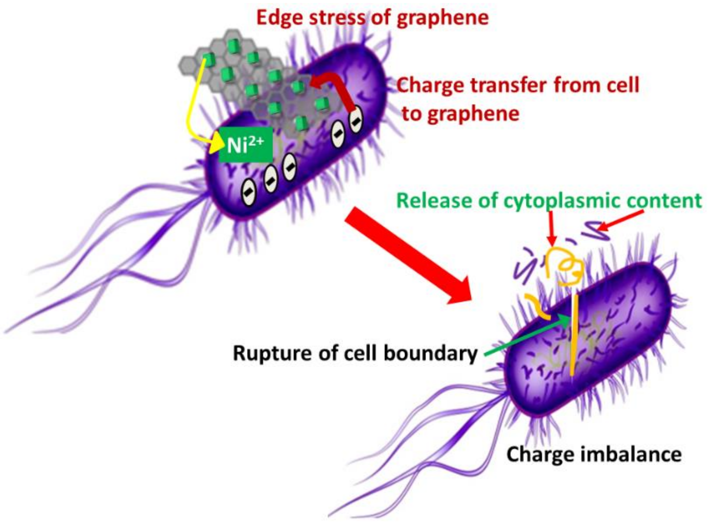

Figure 7. 11 A schematic presentation of bacterial death induced by graphene NiO nanocomposite.

A schematic layout describes the various possible ways to destruct cell in Figure 7. 11. The nanocomposite prepared with definite composition of graphene and NiO (N_z) has shown 100% growth inhibition of both Gram positive and Gram negative bacteria during incubation time. The bacteria were unable to grow in experimental time that ranges from 2h – 24h. Our experimental findings recognize NiO nanoflakes grafted graphene as a novel nanomaterial for complete pathogenic control. This however remains a question for the future to investigate its toxicity for normal cell lines. After, its bio-compatibility is known, it can find safe application as bactericidal material in water and bacterial disinfection units.

7.3 Summary

In summary, NiO and graphene nanocomposites synthesized by solvothermal method are tested for their performance against an industrial dye, methyl orange. N_z nanocomposite efficiently cleans water by photodegrading 99% methyl orange, which otherwise, can be removed up to 34% only, by NiO alone. The interplay between solar excitations, charge trapping by graphene, and carbon purity enable the photocatalyst to perform in an excellent manner. NiO and graphene nanocomposite also meets the economic requirements by being solar-light active and recyclable. Moreover, we find that NiO and graphene nanocomposite is a promising bactericidal material. The growth profiles revealed that N_z nanocomposite is toxic towards Gram positive and Gram-negative bacteria. A 100% bacterial growth inhibition is achieved. The material exhibits bactericidal effects by inducing apoptosis based on complex interplay of properties of both, NiO and graphene.

Chapter No. 8

8. Summary, Conclusions and Recommendations

Overview:

The work presented in the previous chapters is summarized in this chapter. Important results are concluded. In the light of findings, potential future work is also suggested.

8.1 Summary

Although graphene displays many of outstanding physical and chemical properties as discussed in Chapter 1, it is recognized that modification of graphene is vital for altering its performance in a desirable fashion. This was achieved by formation of nanocomposites, constituted by two components, graphene and metal/non-metal oxides. Different nanocomposites synthesized by chemical routes were characterized using XRD, Raman spectroscopy, EDX spectroscopy, SEM, and TEM. SAED patterns and HR-TEM images were also analyzed. These nanocomposites were tested for removal of methyl orange from water, and growth inhibition of *E. coli*, *P. aeruginosa*, and *S. aureus*.

The key points of presented work are summarized in the following table.

Table 8. 1 A summary of the experimental findings

Reaction conditions or findings	MgO/GNPs nanocomposite	Graphene/SiO_2 nanocomposite	Graphene/Fe_3O_4 nanocomposite	Graphene/NiO nanocomposite
Crystallinity	Crystalline, Cubic/hexagonal	Amorphous Hexagonal/-	Crystalline Hexagonal/inverse spinel	Crystalline Hexagonal/FCC
Morphology	Nanohexagons on sheet	Nanoparticles on sheet	Nanoparticles on sheet	Nanoflakes on sheet
EDX	Mg, O, C	Si, O, C	Fe, O, C	Ni, O, C
HR-TEM	(222) 0.12 nm, (220) 0.148 nm, (200)	No planes	(311) 0.253 nm	(111) 0.24 nm
SAED	Verifies XRD	Verifies XRD	Verifies XRD	Verifies XRD
Raman spectroscopy	G band (ca. 1606 cm^{-1})	G band (ca. 1602 cm^{-1})	G band (ca. 1601cm^{-1})	G-band (ca. 1602 cm^{-1})
Conc. of dye	5 ppm	5ppm	20 ppm	20 ppm

Conc. of catalyst	0.4 gL^{-1}	0.3 gL^{-1}	0.2 gL^{-1}	0.2 gL^{-1}
Light source	UV light	UV light	UV light	Sunlight
Degradation efficiency	97.23%	99%	99.24%	99%
Degradation time	120 min	100 min	30 min	55 min
Recyclability	3 cycles	3 cycles	5 cycles	4 cycles
Growth inhibition of *E. coli*	44.5%	51.8%	49.5%	100%
Growth inhibition of *P. aeruginosa*	22.38%	48.97%	89.02%	100%
Growth inhibition of *S. aureus*	49%	75.4%	95.33%	100%

8.2 Conclusions

This thesis was focused on synthesis, and characterization of graphene and metal/non-metal oxides nanocomposites. This thesis was also endeavoured to investigate the application of prepared nanocomposites in photocatalysis based wastewater remediation, particularly, the removal of methyl orange. Another aim of the thesis was to evaluate bacterial disinfection efficiency of nanomaterials under consideration. To this end, the effect of systematic loading of GNPs on physiochemical properties of resultant nanocomposites is studied. In addition, MgO/GNPs, graphene/SiO_2, graphene/Fe_3O_4 and graphene/NiO nanocomposites were comprehensively evaluated for their photocatalytic and antibacterial properties and their performance was also compared under similar conditions with conventional MgO, SiO_2, Fe_3O_4 and NiO. The effect of graphene content for an optimum efficiency of nanocomposites was also evaluated in this thesis.

The first key finding of this thesis was that GNPs provide an effective support for the growth of nanomaterials. GNPs, the multi-layered graphene sheets were intercalated using nanomaterials like MgO, SiO_2, Fe_3O_4 and NiO. GNPs proved to be an efficient platform for their immobilization on Raman spectroscopic results confirmed that these ceramic nanostructures that have different morphologies are anchored on graphene sheets via an electrostatic interaction.

The second important finding was that the synergistic effect created by metal/non-metal oxides and graphene led towards formation of structures that had two distinct photocatalytic activities. A comparison of these structures with control photocatalyst (neat metal/non-metal oxides) showed that graphene contributed positively towards increasing the photocatalytic efficiency. However, the maximum photocatalytic efficiency depended on an optimal graphene concentration. The performance was based on few crucial factors. It was the increased surface area and enhanced conductivity that contributed essentially to provide excess adsorption sites for the dye and longevity of charge carriers' recombination lifetime. The reaction kinetics were well ascribed by Langmuir-Hinshelwood model (pseudo-first order).

The third significant advancement of this work was to achieve an economic solution for complete degradation of dye. To this end, graphene/Fe_3O_4 nanocomposite and graphene/NiO nanocomposite proved to be excellent photocatalysts. MgO/GNPs and graphene/SiO_2 were however, comparatively less efficient catalysts. UV light active, graphene/Fe_3O_4 nanocomposite was magnetically separable from treated water and could be used 5 times without a significant loss in its catalytic activity. Graphene/NiO nanocomposite was solar light active. The infinite availability of sunlight is helpful towards reducing the cost of water treatment. This nanocomposite also meets the stringent economic requirements by being stable for four consecutive catalytic cycles.

A fourth key contribution of this work was based on further investigation on bacterial growth inhibition using graphene and metal/non-metal oxides nanocomposites. It was found that both components of nanocomposites, in a synergistic fashion, played their role to stop bacterial proliferation. The integrated activity of graphene and metal/non-metal oxides served to restrict growth of antibiotic resistant bacteria. It was found that graphene/NiO nanocomposite possessed bactericidal features and bacteria were unable to grow in the entire time of experiment i.e., from 2 h to 24 h. Graphene/Fe_3O_4 nanocomposite also exhibited significant antibacterial activity. Graphene/SiO_2 and MgO/GNPs nanocomposites were however less effective in controlling the bacterial growth.

8.3 Future Perspectives

The research shows the potential of graphene/NiO nanocomposite through sunlight and that of graphene/Fe_3O_4, graphene/SiO_2, MgO/GNPs nanocomposite through UV-light driven photocatalytic activity. The recommendations for future work are detailed below.

There are large number of hazardous industrial pollutants that waste the water and their removal is difficult. For example, bisphenol A, caffeine, sulfamethoxazole, sulfamethoxazole, codeine, carbamazepine, diclofenac, and carcinogenic metals like arsenic etc. Hence, there is opportunity to investigate graphene based nanocomposites for the removal of these hazardous materials from water.

Graphene/NiO nanocomposite showed bactericidal effect with 100% growth inhibition. The number of multi-drug resistant pathogenic microorganisms is rapidly increasing. Therefore, there is a window of opportunity to investigate its effect on the growth of other pathogenic microbes like *Naegleria fowleri*, *Klebsiella Pneumoniae, Candida albicans* etc. The further opportunities are testing the effect of MgO/GNPs, graphene/SiO_2, and graphene/Fe_3O_4 nanocomposite on other untreated pathogens. The magnetic nanocomposite, graphene/Fe_3O_4 can also be tested for its performance against hyperthermia applications. Graphene/SiO_2 nanocomposite are potential platform for attachment of cancer therapeutic drugs, therefore, there is an exciting opportunity to study drug attachment and its effects on cancer treatment.

Appendix

Appendix A - Supplementary Information (Chapter 4)

To verify the chemical bond formation in the pristine MgO and nanocomposites the FTIR spectroscopy was used to obtain the data in the range 400 cm^{-1} to 4000 cm^{-1}. The FTIR spectroscopic response is elaborated in the Figure S 4. 1. MgO nanostructures possess bands below 1000 cm^{-1}. In case of pristine MgO nanohexagons four bands are observed. A band at 424 cm^{-1} can be attributed to the Mg-O stretching vibrations. The other bands associated with Mg-O vibrations are 538 cm^{-1}, 683 cm^{-1}, and 881 cm^{-1}. The adsorbed water molecules and surface hydroxyl groups manifest their presence by a band around 1442 cm^{-1} and 1630 cm^{-1}. These strong bands appear due to hygroscopic nature of MgO. The chemical bond Mg-OH has established the vibrations by a band around 3470 cm^{-1}. The MgO/GNPs nanocomposites with 12% and 25% loaded GNPs show a slight shift in 538 cm^{-1}band to higher wavenumbers. This shift is due to the incorporation of GNPs matrix in the nanocomposite material. Thus, FTIR results are in agreement with the previous report.[327]

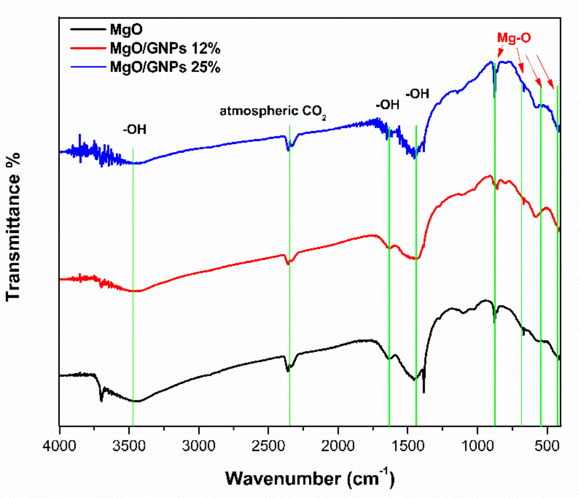

Figure S 4. 1 FTIR spectra of MgO, MgO/GNPs 12% and MgO/GNPs 25% nanocomposites

The absorbance spectra of methyl orange in dark are presented below.

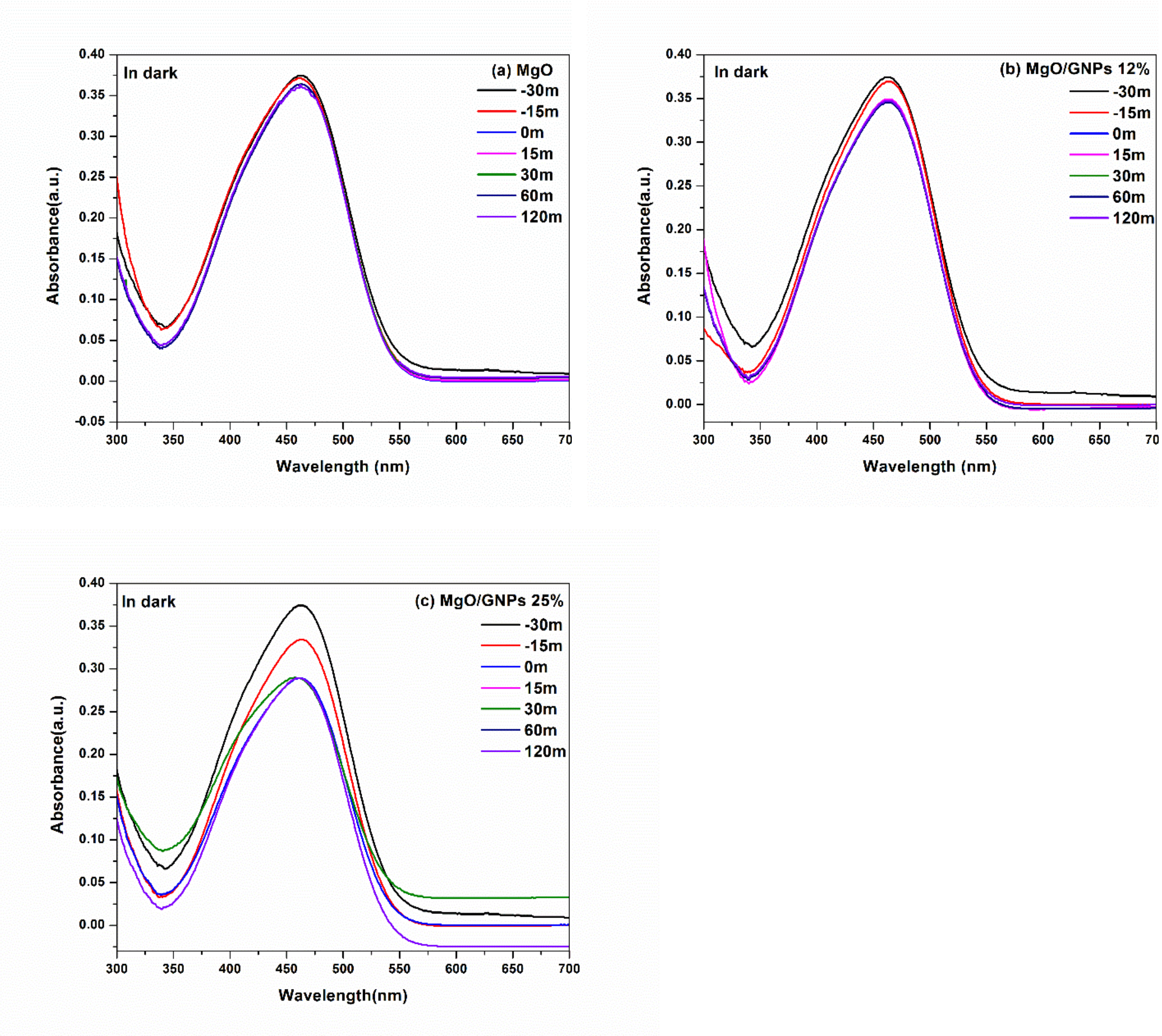

Figure S 4. 2 Adsorption process in MgO, MgO/GNPs 12% and MgO/GNPs 25% nanocomposite in dark

Appendix B - Supplementary Information (Chapter 5)

The FTIR spectroscopic curves are shown in Figure S 5. 1. A band at 460 cm^{-1}can be assigned to the Si-O-Si bending vibrations. The band at 812 cm^{-1}originates due to Si-O symmetric bending vibrations, where –O vibrations are perpendicular to the Si-Si bond line. However, the band in the range of 1045–1107 cm^{-1} is due to parallel vibrations of the oxygen atom in either direction in the Si-O-Si linkage. Thus, it manifests the asymmetric mode of the Si-O-Si bond. The adsorbed water molecules manifest themselves by a band around 1615 cm^{-1}. The chemical bond Si-OH appears as a band around 957 $cm^{-1}$and 3458 cm^{-1}. The graphene/SiO_2 nanocomposites show a significant difference by possessing the presence of a broad band in the range of 1014–1303 cm^{-1}. The C-Si bond manifests itself in this region around 1260 cm^{-1}. Thus, it can be concluded that SiO_2 modified the surface of graphene in nanocomposites. The FTIR results accord well with previous studies.[269, 328]

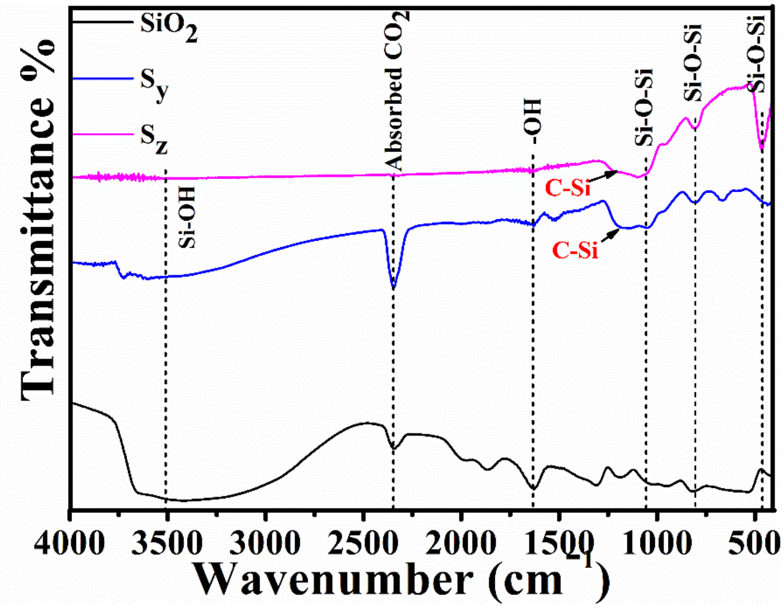

Figure S 5. 1 FTIR spectra of SiO_2 and graphene/SiO_2 nanocomposites

The surface area obtained by N_2 adsorption isotherms are tabulated below.

Table S 5. 1 Surface area analysis of SiO_2, S_y and S_z using N_2 adsorption isotherms

Sample	BET Surface area (m^2g^{-1})	Pore volume (cm^3g^{-1})	Average pore size (Å)
SiO_2	6.3547	0.019405	55.157
S_y	30.2417	0.040561	35.904
S_z	146.5199	0.393357	33.021

Appendix C - Supplementary Information (Chapter 6)

The bandgap energies of neat magnetite and graphene/Fe_3O_4 nanocomposite (F_z) is presented in the following Figure S 6. 1.

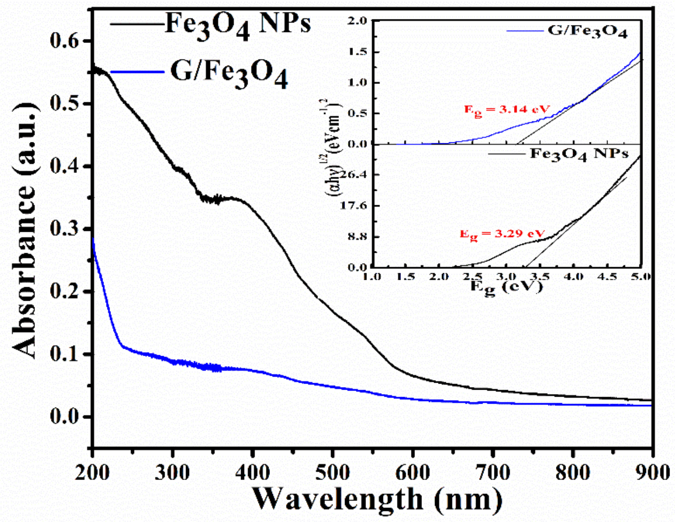

Figure S 6. 1 Bandgap energies of neat magnetite and F_z nanocomposite

Appendix D - Supplementary Information (Chapter 7)

The absorption properties and bandgaps of NiO and graphene/NiO are determined using UV-vis spectroscopy. The absorbance of prepared nanomaterials was obtained for wavelengths from 350 nm – 900 nm (Figure S 7. 1(a)). Following mathematical relation is used to calculate the bandgap energies of NiO, N_y, and N_z nanocomposites.

$$(\boldsymbol{\alpha h\nu})^{\boldsymbol{n}} = \boldsymbol{A}(\boldsymbol{h\nu} - \boldsymbol{E_g}),$$

Here, $\alpha, A, n, h\nu$ and E_g are absorption coefficient, constant, integer, photon energy, and bandgap energy respectively. The bandgap energies are calculated using n = 2 for allowed direct transitions. Tauc's plots presented in Figure S 7. 1(b) show that the bandgap of neat NiO is *ca*. 3.01 ± 0.03 eV. The addition of GNP slightly reduces this value. N_y and N_z possess a bandgap energies equal to 2.85 ± 0.02 eV and 2.83± 0.01 eV respectively. The decrease in bandgap energy is possibly associated with presence of defects states between conduction band and valence band of NiO, which may arise due to interaction of graphene and NiO.[329] The decrease in optical bandgap energy after inclusion of graphene indicates the potential of nanocomposites as photocatalysts under visible light irradiation.

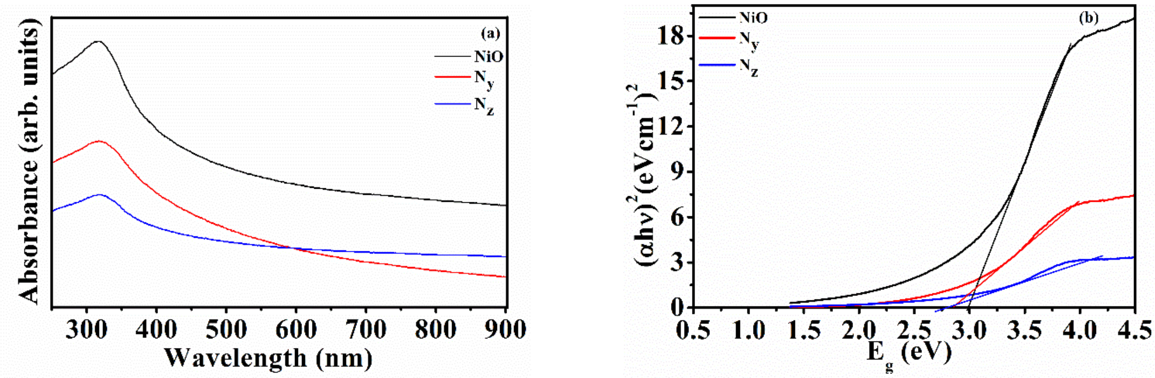

Figure S 7. 1 (a) Absorbance versus wavelength of NiO, N_y, and N_z, and (b) Tauc's plots of NiO, N_y and N_z.

The surface areas were obtained using N_2 adsorption isotherms, such that p/p_o varies from 0-1. The results reveal that the samples that contain both NiO and graphene possess a higher surface area. The average Brunauer-Emmett-Teller (BET) surface area increases in the following order i.e., NiO < N_y < N_z. The findings are summarized in Table S 7. 1. The highest surface area of N_z is attributed to the combined contribution of NiO and graphene in nanocomposite form.

Table S 7. 1 Parameters obtained from N_2 adsorption isotherms

Sample	**BET surface area (m^2g^{-1})**	**Langmuir surface area (m^2g^{-1})**	**Average pore size (Å)**
NiO	44	628	154
N_y	134	731	141
N_z	137	712	131

Appendix E - Graphene Nanoplatelets (GNPs)

The XRD pattern of GNPs is given below.

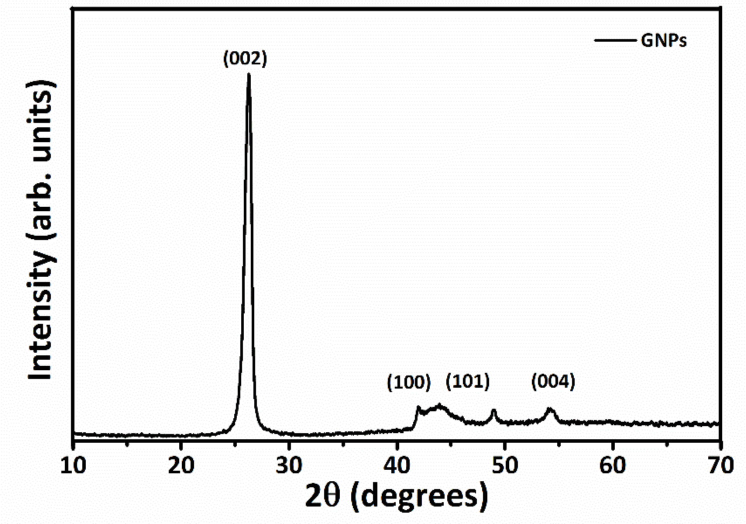

S 8. 1 XRD pattern of GNPs

The SEM image of GNPs are given below.

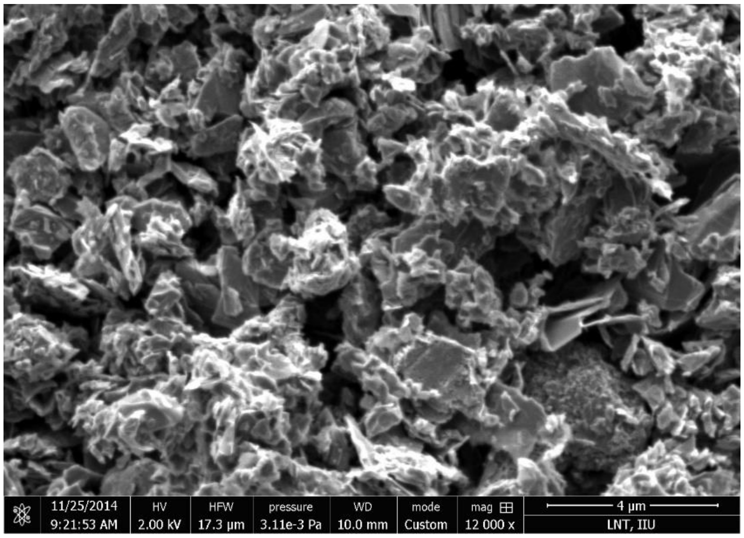

S 8. 2 SEM image of GNPs

References

1. H. W. Kroto, J. R. Heath, S. C. O'Brien, R. F. Curl and R. E. Smalley, *Nature*, 1985, **318**, 162-163.
2. W. Krätschmer, L. D. Lamb, K. Fostiropoulos and D. R. Huffman, *Nature*, 1990, **347**, 27.
3. S. Iijima, *Nature*, 1991, **354**, 56.
4. M. F. L. De Volder, S. H. Tawfick, R. H. Baughman and A. J. Hart, *Science*, 2013, **339**, 535.
5. O. Breuer and U. Sundararaj, *Polymer composites*, 2004, **25**, 630-645.
6. S. R. Shin, S. M. Jung, M. Zalabany, K. Kim, P. Zorlutuna, S. B. Kim, M. Nikkhah, M. Khabiry, M. Azize and J. Kong, *Acs Nano*, 2013, **7**, 2369-2380.
7. Y. Zhang, S. F. Ali, E. Dervishi, Y. Xu, Z. Li, D. Casciano and A. S. Biris, *Acs Nano*, 2010, **4**, 3181-3186.
8. Z. Liu, X. Sun, N. Nakayama-Ratchford and H. Dai, *Acs Nano*, 2007, **1**, 50-56.
9. A. A. Bhirde, V. Patel, J. Gavard, G. Zhang, A. A. Sousa, A. Masedunskas, R. D. Leapman, R. Weigert, J. S. Gutkind and J. F. Rusling, *Acs Nano*, 2009, **3**, 307-316.
10. K. S. Novoselov, A. K. Geim, S. V. Morozov, D. Jiang, Y. Zhang, S. V. Dubonos, I. V. Grigorieva and A. A. Firsov, *Science*, 2004, **306**, 666-669.
11. P. R. Wallace, *Physical Review*, 1947, **71**, 622.
12. A. H. Castro Neto, F. Guinea, N. M. R. Peres, K. S. Novoselov and A. K. Geim, *Reviews of Modern Physics*, 2009, **81**, 109-162.
13. K. S. Novoselov, A. K. Geim, S. V. Morozov, D. Jiang, M. I. Katsnelson, I. V. Grigorieva, S. V. Dubonos and A. A. Firsov, *Nature*, 2005, **438**, 197-200.
14. J.-W. Jiang, B.-S. Wang, J.-S. Wang and H. S. Park, *Journal of Physics: Condensed Matter*, 2015, **27**, 083001.
15. S. Ghosh, W. Bao, D. L. Nika, S. Subrina, E. P. Pokatilov, C. N. Lau and A. A. Balandin, *Nature materials*, 2010, **9**, 555-558.
16. C. Lee, X. Wei, J. W. Kysar and J. Hone, *Science*, 2008, **321**, 385.
17. K. S. Novoselov, S. V. Morozov, T. M. G. Mohinddin, L. A. Ponomarenko, D. C. Elias, R. Yang, I. I. Barbolina, P. Blake, T. J. Booth, D. Jiang, J. Giesbers, E. W. Hill and A. K. Geim, *physica status solidi (b)*, 2007, **244**, 4106-4111.
18. Y. Zhang, Y.-W. Tan, H. L. Stormer and P. Kim, *Nature*, 2005, **438**, 201-204.
19. T. Ando, *Journal of the Physical Society of Japan*, 2006, **75**, 074716.
20. K. Nomura and A. MacDonald, *Physical Review Letters*, 2007, **98**, 076602.
21. A. Reina, X. Jia, J. Ho, D. Nezich, H. Son, V. Bulovic, M. S. Dresselhaus and J. Kong, *Nano letters*, 2008, **9**, 30-35.
22. X. Li, W. Cai, J. An, S. Kim, J. Nah, D. Yang, R. Piner, A. Velamakanni, I. Jung, E. Tutuc, S. K. Banerjee, L. Colombo and R. S. Ruoff, *Science*, 2009, **324**, 1312.
23. K. R. Paton, E. Varrla, C. Backes, R. J. Smith, U. Khan, A. O’Neill, C. Boland, M. Lotya, O. M. Istrate and P. King, *Nature materials*, 2014, **13**, 624-630.
24. X. Li, G. Zhang, X. Bai, X. Sun, X. Wang, E. Wang and H. Dai, *Nature nanotechnology*, 2008, **3**, 538-542.
25. Z.-S. Wu, W. Ren, L. Gao, J. Zhao, Z. Chen, B. Liu, D. Tang, B. Yu, C. Jiang and H.-M. Cheng, *Acs Nano*, 2009, **3**, 411-417.
26. S. Park and R. S. Ruoff, *Nature nanotechnology*, 2009, **4**, 217-224.
27. D. Li, M. B. Muller, S. Gilje, R. B. Kaner and G. G. Wallace, *Nat Nano*, 2008, **3**, 101-105.

28. D. C. Marcano, D. V. Kosynkin, J. M. Berlin, A. Sinitskii, Z. Sun, A. Slesarev, L. B. Alemany, W. Lu and J. M. Tour, *Acs Nano*, 2010, **4**, 4806-4814.
29. W. S. Hummers Jr and R. E. Offeman, *Journal of the American Chemical Society*, 1958, **80**, 1339-1339.
30. L. Staudenmaier, *European Journal of Inorganic Chemistry*, 1898, **31**, 1481-1487.
31. B. Brodie, *Ann. Chim. Phys*, 1860, **59**, e472.
32. S. Stankovich, R. D. Piner, X. Chen, N. Wu, S. T. Nguyen and R. S. Ruoff, *Journal of Materials Chemistry*, 2006, **16**, 155-158.
33. I. Jung, M. Pelton, R. Piner, D. A. Dikin, S. Stankovich, S. Watcharotone, M. Hausner and R. S. Ruoff, *Nano letters*, 2007, **7**, 3569-3575.
34. D. R. Dreyer, S. Park, C. W. Bielawski and R. S. Ruoff, *Chemical Society Reviews*, 2010, **39**, 228-240.
35. U. Khan, A. O'Neill, H. Porwal, P. May, K. Nawaz and J. N. Coleman, *Carbon*, 2012, **50**, 470-475.
36. C. Chung, Y.-K. Kim, D. Shin, S.-R. Ryoo, B. H. Hong and D.-H. Min, *Accounts of chemical research*, 2013, **46**, 2211-2224.
37. M. Pumera, *Energy & Environmental Science*, 2011, **4**, 668-674.
38. K. P. Loh, Q. Bao, G. Eda and M. Chhowalla, *Nature chemistry*, 2010, **2**, 1015-1024.
39. Y. Zhu, S. Murali, W. Cai, X. Li, J. W. Suk, J. R. Potts and R. S. Ruoff, *Advanced Materials*, 2010, **22**, 3906-3924.
40. V. Georgakilas, J. N. Tiwari, K. C. Kemp, J. A. Perman, A. B. Bourlinos, K. S. Kim and R. Zboril, *Chemical reviews*, 2016, **116**, 5464-5519.
41. M. Fang, K. Wang, H. Lu, Y. Yang and S. Nutt, *Journal of Materials Chemistry*, 2009, **19**, 7098-7105.
42. M. Fang, K. Wang, H. Lu, Y. Yang and S. Nutt, *Journal of Materials Chemistry*, 2010, **20**, 1982-1992.
43. S. H. Lee, D. R. Dreyer, J. An, A. Velamakanni, R. D. Piner, S. Park, Y. Zhu, S. O. Kim, C. W. Bielawski and R. S. Ruoff, *Macromolecular rapid communications*, 2010, **31**, 281-288.
44. M. J. McAllister, J.-L. Li, D. H. Adamson, H. C. Schniepp, A. A. Abdala, J. Liu, M. Herrera-Alonso, D. L. Milius, R. Car, R. K. Prud'homme and I. A. Aksay, *Chemistry of Materials*, 2007, **19**, 4396-4404.
45. M. T. H. Aunkor, I. M. Mahbubul, R. Saidur and H. S. C. Metselaar, *RSC Advances*, 2016, **6**, 27807-27828.
46. G. Williams, B. Seger and P. V. Kamat, *Acs Nano*, 2008, **2**, 1487-1491.
47. R. Muszynski, B. Seger and P. V. Kamat, *The Journal of Physical Chemistry C*, 2008, **112**, 5263-5266.
48. V. C. Tung, M. J. Allen, Y. Yang and R. B. Kaner, *Nat Nano*, 2009, **4**, 25-29.
49. G. Wang, J. Yang, J. Park, X. Gou, B. Wang, H. Liu and J. Yao, *The Journal of Physical Chemistry C*, 2008, **112**, 8192-8195.
50. S. Stankovich, D. A. Dikin, G. H. B. Dommett, K. M. Kohlhaas, E. J. Zimney, E. A. Stach, R. D. Piner, S. T. Nguyen and R. S. Ruoff, *Nature*, 2006, **442**, 282-286.
51. V. B. Mohan, R. Brown, K. Jayaraman and D. Bhattacharyya, *Materials Science and Engineering: B*, 2015, **193**, 49-60.
52. J. Shen, Y. Hu, C. Li, C. Qin and M. Ye, *Small*, 2009, **5**, 82-85.
53. J. Shen, Y. Hu, C. Li, C. Qin, M. Shi and M. Ye, *Langmuir*, 2009, **25**, 6122-6128.

54. L. Kavan, J. H. Yum and M. Grätzel, *Acs Nano*, 2010, **5**, 165-172.
55. A. Nieto, D. Lahiri and A. Agarwal, *Carbon*, 2012, **50**, 4068-4077.
56. I.-Y. Jeon, H.-J. Choi, M. J. Ju, I. T. Choi, K. Lim, J. Ko, H. K. Kim, J. C. Kim, J.-J. Lee and D. Shin, *Scientific reports*, 2013, **3**, 2260.
57. I.-Y. Jeon, S.-H. Shin, H.-J. Choi, S.-Y. Yu, S.-M. Jung and J.-B. Baek, *Carbon*, 2017, **116**, 77-83.
58. E. Ruiz-Hitzky, M. M. C. Sobral, A. Gómez-Avilés, C. Nunes, C. Ruiz-García, P. Ferreira and P. Aranda, *Advanced Functional Materials*, 2016, **26**, 7539-7539.
59. M. J. Ju, I.-Y. Jeon, H. M. Kim, J. I. Choi, S.-M. Jung, J.-M. Seo, I. T. Choi, S. H. Kang, H. S. Kim and M. J. Noh, *Science advances*, 2016, **2**, e1501459.
60. E. Messina, N. Leone, A. Foti, G. Di Marco, C. Riccucci, G. Di Carlo, F. Di Maggio, A. Cassata, L. Gargano, C. D'Andrea, B. Fazio, O. M. Maragò, B. Robba, C. Vasi, G. M. Ingo and P. G. Gucciardi, *ACS Applied Materials & Interfaces*, 2016, **8**, 23244-23259.
61. R. D. Smith, M. S. Prévot, R. D. Fagan, Z. Zhang, P. A. Sedach, M. K. J. Siu, S. Trudel and C. P. Berlinguette, *Science*, 2013, **340**, 60-63.
62. H. Wang, H.-W. Lee, Y. Deng, Z. Lu, P.-C. Hsu, Y. Liu, D. Lin and Y. Cui, *Nature communications*, 2015, **6**.
63. C. Clavero, *Nature Photonics*, 2014, **8**, 95-103.
64. S. H. Joo and D. Zhao, *Journal of hazardous materials*, 2017, **322**, 29-47.
65. X. Liu, J. Iocozzia, Y. Wang, X. Cui, Y. Chen, S. Zhao, Z. Li and Z. Lin, *Energy & Environmental Science*, 2017.
66. J. Gao, H. Gu and B. Xu, *Accounts of chemical research*, 2009, **42**, 1097-1107.
67. J. Jiang, Y. Li, J. Liu, X. Huang, C. Yuan and X. W. D. Lou, *Advanced Materials*, 2012, **24**, 5166-5180.
68. C. Su, *Journal of hazardous materials*, 2017, **322**, 48-84.
69. Z.-S. Wu, G. Zhou, L.-C. Yin, W. Ren, F. Li and H.-M. Cheng, *Nano Energy*, 2012, **1**, 107-131.
70. R. Raccichini, A. Varzi, S. Passerini and B. Scrosati, *Nature materials*, 2015, **14**, 271-279.
71. H. Sun, L. Mei, J. Liang, Z. Zhao, C. Lee, H. Fei, M. Ding, J. Lau, M. Li and C. Wang, *Science*, 2017, **356**, 599-604.
72. W. Ma, S. Chen, S. Yang, W. Chen, W. Weng, Y. Cheng and M. Zhu, *Carbon*, 2017, **113**, 151-158.
73. C. Liu, H. Sun, J. Qian, Z. Chen, F. Chen, S. Liu, Y. Lv, X. Lu and A. Chen, *Journal of Alloys and Compounds*, 2017.
74. M. Sreejesh, S. Shenoy, K. Sridharan, D. Kufian, A. Arof and H. Nagaraja, *Applied Surface Science*, 2017, **410**, 336-343.
75. P. A. Russo, N. Donato, S. G. Leonardi, S. Baek, D. E. Conte, G. Neri and N. Pinna, *Angewandte Chemie International Edition*, 2012, **51**, 11053-11057.
76. Q. Huang, D. Zeng, H. Li and C. Xie, *Nanoscale*, 2012, **4**, 5651-5658.
77. H. Zhang, L. Yu, Q. Li, Y. Du and S. Ruan, *Sensors and Actuators B: Chemical*, 2017, **241**, 109-115.
78. Y.-L. Ren, H.-Y. Wu, M.-M. Lu, Y.-J. Chen, C.-L. Zhu, P. Gao, M.-S. Cao, C.-Y. Li and Q.-Y. Ouyang, *ACS Applied Materials & Interfaces*, 2012, **4**, 6436-6442.
79. P.-B. Liu, Y. Huang and X. Sun, *ACS Applied Materials & Interfaces*, 2013, **5**, 12355-12360.

80. C. Song, X. Yin, M. Han, X. Li, Z. Hou, L. Zhang and L. Cheng, *Carbon*, 2017, **116**, 50-58.
81. S. V. A. Muthukrishnaraj, V. P. Kamalakannan & N. Balasubramanian, *Materials Research Innovations*, 2014, **19**, 258-264.
82. L. Ai, C. Zhang and Z. Chen, *Journal of hazardous materials*, 2011, **192**, 1515-1524.
83. X. Bai, C. Sun, D. Liu, X. Luo, D. Li, J. Wang, N. Wang, X. Chang, R. Zong and Y. Zhu, *Applied Catalysis B: Environmental*, 2017, **204**, 11-20.
84. V. Chandra, J. Park, Y. Chun, J. W. Lee, I.-C. Hwang and K. S. Kim, *Acs Nano*, 2010, **4**, 3979-3986.
85. M. A. Farghali, T. A. S. El-Din, A. M. Al-Enizi and R. M. El Bahnasawy, *Int. J. Electrochem. Sci*, 2015, **10**, 529-537.
86. L. Fu, T. Xia, Y. Zheng, J. Yang, A. Wang and Z. Wang, *Ceramics International*, 2015, **41**, 5903-5908.
87. D. K. P. Gajendra Kumar Pradhan, and K. M. Parida, *ACS Applied Materials & Interfaces*, 2013 **5**, 9101-9110.
88. G. Zhao, J. Li, X. Ren, C. Chen and X. Wang, *Environmental Science & Technology*, 2011, **45**, 10454-10462.
89. R. K. Upadhyay, N. Soin and S. S. Roy, *RSC Advances*, 2014, **4**, 3823-3851.
90. A. Xu, B. Li, B. Zhan, S. Xue, R. Guo and W. Zhong, *Int. J. Electrochem. Sci*, 2017, **12**, 448-454.
91. W. Zhu, F. Sun, R. Goei and Y. Zhou, *Applied Catalysis B: Environmental*, 2017, **207**, 93-102.
92. J. Li, G. Wang, H. Zhu, M. Zhang, X. Zheng, Z. Di, X. Liu and X. Wang, *Scientific Reports*, 2014, **4**, 4359.
93. M. D. Rojas-Andrade, G. Chata, D. Rouholiman, J. Liu, C. Saltikov and S. Chen, *Nanoscale*, 2017.
94. S. Szunerits and R. Boukherroub, *Journal of Materials Chemistry B*, 2016, **4**, 6892-6912.
95. Y.-W. Wang, A. Cao, Y. Jiang, X. Zhang, J.-H. Liu, Y. Liu and H. Wang, *ACS Applied Materials & Interfaces*, 2014, **6**, 2791-2798.
96. X. Zou, L. Zhang, Z. Wang and Y. Luo, *J Am Chem Soc*, 2016, **138**, 2064-2077.
97. C. Santhosh, P. Kollu, S. Doshi, M. Sharma, D. Bahadur, M. T. Vanchinathan, P. Saravanan, B.-S. Kim and A. N. Grace, *RSC Advances*, 2014, **4**, 28300-28308.
98. I. Ocsoy, M. Temiz, C. Celik, B. Altinsoy, V. Yilmaz and F. Duman, *Journal of Molecular Liquids*, 2017, **227**, 147-152.
99. A. Fujishima and K. Honda, *Nature*, 1972, **238**, 37-38.
100. A. L. Linsebigler, G. Lu and J. T. Yates, *Chemical reviews*, 1995, **95**, 735-758.
101. K. V. Kumar, K. Porkodi and F. Rocha, *Catalysis Communications*, 2008, **9**, 82-84.
102. D. Monllor-Satoca, R. Gómez, M. González-Hidalgo and P. Salvador, *Catalysis Today*, 2007, **129**, 247-255.
103. A. V. Emeline, V. Ryabchuk and N. Serpone, *Journal of Photochemistry and Photobiology A: Chemistry*, 2000, **133**, 89-97.
104. D. J. Hentges, *Human intestinal microflora in health and disease*, Academic Press, 2012.
105. G. P. Bodey, R. Bolivar, V. Fainstein and L. Jadeja, *Review of Infectious Diseases*, 1983, **5**, 279-313.
106. M. A. Fox and M. T. Dulay, *Chemical reviews*, 1993, **93**, 341-357.

107. J. Su, M. Cao, L. Ren and C. Hu, *The Journal of Physical Chemistry C*, 2011, **115**, 14469-14477.
108. V. R. Posa, V. Annavaram, J. R. Koduru, V. R. Ammireddy and A. R. Somala, *Korean Journal of Chemical Engineering*, 2016, **33**, 456-464.
109. L. Yang, L. Wang, M. Xing, J. Lei and J. Zhang, *Applied Catalysis B: Environmental*, 2016, **180**, 106-112.
110. S. Chowdhury and R. Balasubramanian, *Applied Catalysis B: Environmental*, 2014, **160**, 307-324.
111. J. Gómez-Pastora, S. Dominguez, E. Bringas, M. J. Rivero, I. Ortiz and D. D. Dionysiou, *Chemical Engineering Journal*, 2017, **310**, 407-427.
112. D. Zhang, X. Pu, G. Ding, X. Shao, Y. Gao, J. Liu, M. Gao and Y. Li, *Journal of Alloys and Compounds*, 2013, **572**, 199-204.
113. F. Soofivand and M. Salavati-Niasari, *Journal of Photochemistry and Photobiology A: Chemistry*, 2017, **337**, 44-53.
114. N. R. Khalid, E. Ahmed, Z. Hong, L. Sana and M. Ahmed, *Current Applied Physics*, 2013, **13**, 659-663.
115. J. Zhang, Z. Xiong and X. S. Zhao, *Journal of Materials Chemistry*, 2011, **21**, 3634-3640.
116. G. S. Anjusree, A. S. Nair, S. V. Nair and S. Vadukumpully, *RSC Advances*, 2013, **3**, 12933-12938.
117. M. Zhou, J. Yan and P. Cui, *Materials Letters*, 2012, **89**, 258-261.
118. S. Sarkar and D. Basak, *Chemical Physics Letters*, 2013, **561**, 125-130.
119. G. Jiang, Z. Lin, C. Chen, L. Zhu, Q. Chang, N. Wang, W. Wei and H. Tang, *Carbon*, 2011, **49**, 2693-2701.
120. N. A. Zubir, C. Yacou, J. Motuzas, X. Zhang and J. C. D. da Costa, *Scientific reports*, 2014, **4**, 4594.
121. T. Peik-See, A. Pandikumar, L. H. Ngee, H. N. Ming and C. C. Hua, *Catalysis Science & Technology*, 2014, **4**, 4396-4405.
122. P. Wang, L. Wang, Q. Sun, S. Qiu, Y. Liu, X. Zhang, X. Liu and L. Zheng, *Materials Letters*, 2016, **183**, 61-64.
123. S. Guo, G. Zhang, Y. Guo and C. Y. Jimmy, *Carbon*, 2013, **60**, 437-444.
124. L. Zhang, Z. Bao, X. Yu, P. Dai, J. Zhu, M. Wu, G. Li, X. Liu, Z. Sun and C. Chen, *ACS Applied Materials & Interfaces*, 2016, **8**, 6431-6438.
125. R. Verma and S. K. Samdarshi, *The Journal of Physical Chemistry C*, 2016, **120**, 22281-22290.
126. S. Chandra, P. Das, S. Bag, R. Bhar and P. Pramanik, *Materials Science and Engineering: B*, 2012, **177**, 855-861.
127. Y. Liu, Y. Hu, M. Zhou, H. Qian and X. Hu, *Applied Catalysis B: Environmental*, 2012, **125**, 425-431.
128. J. P. Kehrer, *Toxicology*, 2000, **149**, 43-50.
129. M. Heidarizad and S. S. Şengör, *Journal of Molecular Liquids*, 2016, **224**, 607-617.
130. A. N. Soon and B. Hameed, *Desalination*, 2011, **269**, 1-16.
131. F. Duarte, F. Maldonado-Hódar, A. Pérez-Cadenas and L. M. Madeira, *Applied Catalysis B: Environmental*, 2009, **85**, 139-147.
132. O. C. Compton and S. T. Nguyen, *Small*, 2010, **6**, 711-723.
133. N. A. Zubir, C. Yacou, J. Motuzas, X. Zhang, X. S. Zhao and J. C. D. da Costa, *Chemical Communications*, 2015, **51**, 9291-9293.

134. N. A. Zubir, C. Yacou, X. Zhang and J. C. D. da Costa, *Journal of Environmental Chemical Engineering*, 2014, **2**, 1881-1888.
135. M. Rai, A. Yadav and A. Gade, *Biotechnology advances*, 2009, **27**, 76-83.
136. D. MubarakAli, N. Thajuddin, K. Jeganathan and M. Gunasekaran, *Colloids and Surfaces B: Biointerfaces*, 2011, **85**, 360-365.
137. E. Hoseinzadeh, P. Makhdoumi, P. Taha, H. Hossini, J. Stelling and M. Amjad Kamal, *Current drug metabolism*, 2017, **18**, 120-128.
138. X. Li, S. M. Robinson, A. Gupta, K. Saha, Z. Jiang, D. F. Moyano, A. Sahar, M. A. Riley and V. M. Rotello, *Acs Nano*, 2014, **8**, 10682-10686.
139. N. Padmavathy and R. Vijayaraghavan, *Science and technology of advanced materials*, 2008, **9**, 035004.
140. R. Kumar, A. Umar, G. Kumar and H. S. Nalwa, *Ceramics International*, 2016.
141. A. Sirelkhatim, S. Mahmud, A. Seeni, N. H. M. Kaus, L. C. Ann, S. K. M. Bakhori, H. Hasan and D. Mohamad, *Nano-Micro Lett*, 2015, **7**, 219-242.
142. N. Liu, Y. Chang, Y. Feng, Y. Cheng, X. Sun, H. Jian, Y. Feng, X. Li and H. Zhang, *ACS Applied Materials & Interfaces*, 2017, **9**, 5907-5915.
143. T. Li, N. Wang, S. Chen, R. Lu, H. Li and Z. Zhang, *International journal of nanomedicine*, 2017, **12**, 2995.
144. X. Li, J. Xie, L. Liao, X. Jiang and H. Fu, *International Journal of Polymeric Materials and Polymeric Biomaterials*, 2017.
145. G. Fu, P. S. Vary and C.-T. Lin, *The Journal of Physical Chemistry B*, 2005, **109**, 8889-8898.
146. P. Dibrov, J. Dzioba, K. K. Gosink and C. C. Häse, *Antimicrobial agents and chemotherapy*, 2002, **46**, 2668-2670.
147. W.-R. Li, X.-B. Xie, Q.-S. Shi, H.-Y. Zeng, Y.-S. Ou-Yang and Y.-B. Chen, *Applied microbiology and biotechnology*, 2010, **85**, 1115-1122.
148. L. Zhang, Y. Jiang, Y. Ding, N. Daskalakis, L. Jeuken, M. Povey, A. J. O'Neill and D. W. York, *Journal of Nanoparticle Research*, 2010, **12**, 1625-1636.
149. H. Yang, C. Liu, D. Yang, H. Zhang and Z. Xi, *Journal of applied Toxicology*, 2009, **29**, 69-78.
150. T. Xia, M. Kovochich, M. Liong, L. Mädler, B. Gilbert, H. Shi, J. I. Yeh, J. I. Zink and A. E. Nel, *Acs Nano*, 2008, **2**, 2121-2134.
151. K. R. Raghupathi, R. T. Koodali and A. C. Manna, *Langmuir*, 2011, **27**, 4020-4028.
152. R. Brayner, R. Ferrari-Iliou, N. Brivois, S. Djediat, M. F. Benedetti and F. Fiévet, *Nano letters*, 2006, **6**, 866-870.
153. S. Liu, T. H. Zeng, M. Hofmann, E. Burcombe, J. Wei, R. Jiang, J. Kong and Y. Chen, *Acs Nano*, 2011, **5**, 6971-6980.
154. R. K. Upadhyay, A. Dubey, P. R. Waghmare, R. Priyadarshini and S. S. Roy, *RSC Advances*, 2016, **6**, 62760-62767.
155. Q. Bao, D. Zhang and P. Qi, *Journal of colloid and interface science*, 2011, **360**, 463-470.
156. L. Dellieu, E. Lawarée, N. Reckinger, C. Didembourg, J.-J. Letesson, M. Sarrazin, O. Deparis, J.-Y. Matroule and J.-F. Colomer, *Carbon*, 2015, **84**, 310-316.
157. O. N. Ruiz, K. S. Fernando, B. Wang, N. A. Brown, P. G. Luo, N. D. McNamara, M. Vangsness, Y.-P. Sun and C. E. Bunker, *Acs Nano*, 2011, **5**, 8100-8107.
158. V. T. Pham, V. K. Truong, M. D. Quinn, S. M. Notley, Y. Guo, V. A. Baulin, M. Al Kobaisi, R. J. Crawford and E. P. Ivanova, *Acs Nano*, 2015, **9**, 8458-8467.

159. F. Zou, H. Zhou, D. Y. Jeong, J. Kwon, S. U. Eom, T. J. Park, S. W. Hong and J. Lee, *ACS Applied Materials & Interfaces*, 2017, **9**, 1343-1351.
160. H.-q. Chen, D. Gao, B. Wang, R.-f. Zhao, M. Guan, L.-n. Zheng, X.-y. Zhou, Z.-f. Chai and W.-y. Feng, *Nanotechnology*, 2014, **25**, 165101.
161. B. Song, C. Zhang, G. Zeng, J. Gong, Y. Chang and Y. Jiang, *Archives of biochemistry and biophysics*, 2016, **604**, 167-176.
162. S. Liu, M. Hu, T. H. Zeng, R. Wu, R. Jiang, J. Wei, L. Wang, J. Kong and Y. Chen, *Langmuir*, 2012, **28**, 12364-12372.
163. J. Cui and Y. Liu, *RSC Advances*, 2015, **5**, 85748-85755.
164. S. Bykkam, S. Narsingam, M. Ahmadipour, T. Dayakar, K. V. Rao, C. S. Chakra and S. Kalakotla, *Superlattices and Microstructures*, 2015, **83**, 776-784.
165. K. Ravichandran, N. Chidhambaram and S. Gobalakrishnan, *Journal of Physics and Chemistry of Solids*, 2016, **93**, 82-90.
166. B.-S. Wu, H. N. Abdelhamid and H.-F. Wu, *RSC Advances*, 2014, **4**, 3722-3731.
167. O. Akhavan and E. Ghaderi, *The Journal of Physical Chemistry C*, 2009, **113**, 20214-20220.
168. Y.-N. Chang, X.-M. Ou, G.-M. Zeng, J.-L. Gong, C.-H. Deng, Y. Jiang, J. Liang, G.-Q. Yuan, H.-Y. Liu and X. He, *Applied Surface Science*, 2015, **343**, 1-10.
169. A. Nourmohammadi, R. Rahighi, O. Akhavan and A. Moshfegh, *Journal of Alloys and Compounds*, 2014, **612**, 380-385.
170. S. Zhan, D. Zhu, S. Ma, W. Yu, Y. Jia, Y. Li, H. Yu and Z. Shen, *ACS Applied Materials & Interfaces*, 2015, **7**, 4290-4298.
171. C.-H. Deng, J.-L. Gong, G.-M. Zeng, C.-G. Niu, Q.-Y. Niu, W. Zhang and H.-Y. Liu, *Journal of hazardous materials*, 2014, **276**, 66-76.
172. P. Valentina, L. Maria Carmela, C. Gabriele, C. Claudio, S. Marco De and P. Massimiliano, *Nanotechnology*, 2017, **28**, 152001.
173. I. Barbolina, C. Woods, N. Lozano, K. Kostarelos, K. Novoselov and I. Roberts, *2D Materials*, 2016, **3**, 025025.
174. O. Akhavan, E. Ghaderi and A. Esfandiar, *The Journal of Physical Chemistry B*, 2011, **115**, 6279-6288.
175. F. Perreault, A. F. De Faria, S. Nejati and M. Elimelech, *Acs Nano*, 2015, **9**, 7226-7236.
176. Y. Tu, M. Lv, P. Xiu, T. Huynh, M. Zhang, M. Castelli, Z. Liu, Q. Huang, C. Fan and H. Fang, *Nature nanotechnology*, 2013, **8**, 594-601.
177. R. Combarros, S. Collado and M. Diaz, *Journal of hazardous materials*, 2016, **310**, 246-252.
178. D. Eley and D. Spivey, *Transactions of the faraday society*, 1960, **56**, 1432-1442.
179. N. Kurantowicz, E. Sawosz, S. Jaworski, M. Kutwin, B. Strojny, M. Wierzbicki, J. Szeliga, A. Hotowy, L. Lipińska and R. Koziński, *Nanoscale research letters*, 2015, **10**, 23.
180. K. Krishnamoorthy, M. Veerapandian, L.-H. Zhang, K. Yun and S. J. Kim, *The Journal of Physical Chemistry C*, 2012, **116**, 17280-17287.
181. K. Krishnamoorthy, G. Manivannan, S. J. Kim, K. Jeyasubramanian and M. Premanathan, *Journal of Nanoparticle Research*, 2012, **14**, 1-10.
182. J. Suresh, R. G. R. Gandhi, S. Selvam and M. Sundrarajan, 2013.
183. I. A. Ibrahim, A. Zikry and M. A. Sharaf, *J. Am. Sci*, 2010, **6**, 985-989.
184. J. A. Lopez, F. González, F. A. Bonilla, G. Zambrano and M. E. Gómez, *Revista Latinoamericana de Metalurgia y Materiales*, 2010, 60-66.

185. Y. Mahaleh, S. Sadrnezhaad and D. Hosseini, *Journal of Nanomaterials*, 2008, **2008**, 78.
186. B. Zhao, J. Song, P. Liu, W. Xu, T. Fang, Z. Jiao, H. Zhang and Y. Jiang, *Journal of Materials Chemistry*, 2011, **21**, 18792-18798.
187. C. V. Raman and K. S. Krishnan, *Nature*, 1928, **121**, 501-502.
188. G. Landsberg, *Naturwissenschaften*, 1928, **16**, 558.
189. J. R. Ferraro, *Introductory raman spectroscopy*, Academic press, 2003.
190. L. Malard, M. Pimenta, G. Dresselhaus and M. Dresselhaus, *Physics Reports*, 2009, **473**, 51-87.
191. M. Lazzeri, C. Attaccalite, L. Wirtz and F. Mauri, *Physical Review B*, 2008, **78**, 081406.
192. A. C. Ferrari, J. Meyer, V. Scardaci, C. Casiraghi, M. Lazzeri, F. Mauri, S. Piscanec, D. Jiang, K. Novoselov and S. Roth, *Physical Review Letters*, 2006, **97**, 187401.
193. M. S. Dresselhaus, G. Dresselhaus, R. Saito and A. Jorio, *Physics Reports*, 2005, **409**, 47-99.
194. J. Solé, L. Bausa and D. Jaque, *An introduction to the optical spectroscopy of inorganic solids*, John Wiley & Sons, 2005.
195. W. Friedrich, P. Knipping and M. Laue, *Annalen der Physik*, 1913, **346**, 971-988.
196. M. von Laue, *Nobel lecture*, 1915, 13.
197. Y. Leng, *Materials characterization: introduction to microscopic and spectroscopic methods*, John Wiley & Sons, 2009.
198. W. D. Callister and D. G. Rethwisch, *Materials science and engineering*, John Wiley & Sons NY, 2011.
199. U. Holzwarth and N. Gibson, *Nat Nano*, 2011, **6**, 534-534.
200. P. Scherrer, in *Kolloidchemie Ein Lehrbuch*, Springer, 1912, pp. 387-409.
201. M. von Ardenne, *Z. Phys*, 1938, **109**, 553-572.
202. P. W. Hawkes, *Advances in imaging and electron physics*, Academic press, 2001.
203. J. Goldstein, D. E. Newbury, P. Echlin, D. C. Joy, A. D. Romig Jr, C. E. Lyman, C. Fiori and E. Lifshin, *Scanning electron microscopy and X-ray microanalysis: a text for biologists, materials scientists, and geologists*, Springer Science & Business Media, 2012.
204. S. Foner, *Review of Scientific Instruments*, 1956, **27**, 548-548.
205. M. S. Lubell and A. S. Venturino, *Review of Scientific Instruments*, 1960, **31**, 207-208.
206. F. Fiorillo, *Measurement and characterization of magnetic materials*, North-Holland, 2004.
207. A. Beer, *Ann. Physik*, 1852, **162**, 78-88.
208. J. A. Räty, K.-E. Peiponen and T. Asakura, *UV-visible reflection spectroscopy of liquids*, Springer Science & Business Media, 2004.
209. A. Sarkar, E. Gracia-Espino, T. Wågberg, A. Shchukarev, M. Mohl, A.-R. Rautio, O. Pitkänen, T. Sharifi, K. Kordas and J.-P. Mikkola, *Nano Research*, 2016, **9**, 1956-1968.
210. L. Pan, S. Wang, J. Xie, L. Wang, X. Zhang and J.-J. Zou, *Nano Energy*, 2016, **28**, 296-303.
211. S. Bai, L. Wang, X. Chen, J. Du and Y. Xiong, *Nano Research*, 2015, **8**, 175-183.
212. W. J. Ong, L. L. Tan, S. P. Chai, S. T. Yong and A. R. Mohamed, *ChemSusChem*, 2014, **7**, 690-719.
213. S. Bai, M. Xie, Q. Kong, W. Jiang, R. Qiao, Z. Li, J. Jiang and Y. Xiong, *Particle & Particle Systems Characterization*, 2016, **33**, 506-511.
214. D. Spagnoli, J. P. Allen and S. C. Parker, *Langmuir*, 2011, **27**, 1821-1829.
215. D. Roessler and W. Walker, *Physical Review*, 1967, **159**, 733.

216. C. Y. Tai, C.-T. Tai, M.-H. Chang and H.-S. Liu, *Industrial & Engineering Chemistry Research*, 2007, **46**, 5536-5541.
217. X. S. Fang, C. H. Ye, L. D. Zhang, J. X. Zhang, J. W. Zhao and P. Yan, *Small*, 2005, **1**, 422-428.
218. Y. Yin, G. Zhang and Y. Xia, *Advanced Functional Materials*, 2002, **12**, 293-298.
219. Y. Li, Y. Bando, D. Golberg and Z. Liu, *Applied physics letters*, 2003, **83**, 999-1001.
220. Z.-X. Tang and B.-F. Lv, *Brazilian Journal of Chemical Engineering*, 2014, **31**, 591-601.
221. F. Al-Hazmi, F. Alnowaiser, A. Al-Ghamdi, A. A. Al-Ghamdi, M. Aly, R. M. Al-Tuwirqi and F. El-Tantawy, *Superlattices and Microstructures*, 2012, **52**, 200-209.
222. B. Vatsha, P. Tetyana, P. M. Shumbula, J. C. Ngila, L. M. Sikhwivhilu and R. M. Moutloali, *Journal of Biomaterials and Nanobiotechnology*, 2013, **4**, 365.
223. J. Lee, T. Jeong, S. Yu, S. Jin, J. Heo, W. Yi and J. Kim, *Journal of Vacuum Science & Technology B: Microelectronics and Nanometer Structures Processing, Measurement, and Phenomena*, 2001, **19**, 1366-1369.
224. B. Wei, R. Vajtai, Z. Zhang, G. Ramanath and P. Ajayan, *Journal of Nanoscience and Nanotechnology*, 2001, **1**, 35-38.
225. L. Sohrabi, F. Taleshi and R. Sohrabi, *Journal of Materials Science: Materials in Electronics*, 2014, **25**, 4110-4114.
226. T. Venkatesha, R. Viswanatha, Y. A. Nayaka and B. Chethana, *Chemical Engineering Journal*, 2012, **198**, 1-10.
227. G. Moussavi and M. Mahmoudi, *Journal of hazardous materials*, 2009, **168**, 806-812.
228. Y. H. Leung, A. Ng, X. Xu, Z. Shen, L. A. Gethings, M. T. Wong, C. Chan, M. Y. Guo, Y. H. Ng and A. B. Djurišić, *Small*, 2014, **10**, 1171-1183.
229. J. R. Lee, J. Y. Bae, W. Jang, J.-H. Lee, W. San Choi and H. Y. Koo, *RSC Advances*, 2015, **5**, 83668-83673.
230. F.-p. Du, W. Yang, F. Zhang, C.-Y. Tang, S.-p. Liu, L. Yin and W.-C. Law, *ACS Applied Materials & Interfaces*, 2015, **7**, 14397-14403.
231. H. W. Kim, S. H. Shim, J. W. Lee and C. Lee, *JOURNAL-KOREAN PHYSICAL SOCIETY*, 2007, **51**, 204.
232. H. R. Moon, J. J. Urban and D. J. Milliron, *Angewandte Chemie International Edition*, 2009, **48**, 6278-6281.
233. A. Gupta, G. Chen, P. Joshi, S. Tadigadapa and P. Eklund, *Nano letters*, 2006, **6**, 2667-2673.
234. M. S. A. Sher Shah, A. R. Park, K. Zhang, J. H. Park and P. J. Yoo, *ACS Applied Materials & Interfaces*, 2012, **4**, 3893-3901.
235. M. Y. Guo, A. M. C. Ng, F. Liu, A. B. Djurišić and W. K. Chan, *Applied Catalysis B: Environmental*, 2011, **107**, 150-157.
236. Y. Badr and M. Mahmoud, *Journal of Physics and Chemistry of Solids*, 2007, **68**, 413-419.
237. F. Soofivand and M. Salavati-Niasari, *RSC Advances*, 2015, **5**, 64346-64353.
238. R. Comparelli, E. Fanizza, M. Curri, P. Cozzoli, G. Mascolo, R. Passino and A. Agostiano, *Applied Catalysis B: Environmental*, 2005, **55**, 81-91.
239. R. Comparelli, E. Fanizza, M. Curri, P. Cozzoli, G. Mascolo and A. Agostiano, *Applied Catalysis B: Environmental*, 2005, **60**, 1-11.
240. S. Gayathri, P. Jayabal, M. Kottaisamy and V. Ramakrishnan, *Journal of Applied Physics*, 2014, **115**, 173504.

241. X. An, C. Y. Jimmy, Y. Wang, Y. Hu, X. Yu and G. Zhang, *Journal of Materials Chemistry*, 2012, **22**, 8525-8531.
242. K. Mageshwari, S. S. Mali, R. Sathyamoorthy and P. S. Patil, *Powder technology*, 2013, **249**, 456-462.
243. O. Akhavan and E. Ghaderi, *Acs Nano*, 2010, **4**, 5731-5736.
244. A. M. Jastrzębska, P. Kurtycz and A. R. Olszyna, *Journal of Nanoparticle Research*, 2012, **14**, 1320.
245. C. D. Vecitis, K. R. Zodrow, S. Kang and M. Elimelech, *Acs Nano*, 2010, **4**, 5471-5479.
246. S. Kang, M. Herzberg, D. F. Rodrigues and M. Elimelech, *Langmuir*, 2008, **24**, 6409-6413.
247. S. Liu, L. Wei, L. Hao, N. Fang, M. W. Chang, R. Xu, Y. Yang and Y. Chen, *Acs Nano*, 2009, **3**, 3891-3902.
248. D. Y. Lyon and P. J. Alvarez, *Environmental Science & Technology*, 2008, **42**, 8127-8132.
249. B. Czech and W. Buda, *Environmental research*, 2015, **137**, 176-184.
250. H. R. Jafry, M. V. Liga, Q. Li and A. R. Barron, *Environmental Science & Technology*, 2010, **45**, 1563-1568.
251. T. Kavitha, A. I. Gopalan, K.-P. Lee and S.-Y. Park, *Carbon*, 2012, **50**, 2994-3000.
252. Y. Li, W. Zhang, J. Niu and Y. Chen, *Acs Nano*, 2012, **6**, 5164-5173.
253. A. Popat, S. B. Hartono, F. Stahr, J. Liu, S. Z. Qiao and G. Q. M. Lu, *Nanoscale*, 2011, **3**, 2801-2818.
254. X. Yang, Z. Shen, B. Zhang, J. Yang, W.-X. Hong, Z. Zhuang and J. Liu, *Chemosphere*, 2013, **90**, 653-656.
255. R. D. C. Soltani, A. Khataee, M. Safari and S. Joo, *International Biodeterioration & Biodegradation*, 2013, **85**, 383-391.
256. X. Li, J. Zhang and H. Gu, *Langmuir*, 2011, **27**, 6099-6106.
257. B. Bharti, J. Meissner and G. H. Findenegg, *Langmuir*, 2011, **27**, 9823-9833.
258. Y. Badr, M. A. El-Wahed and M. Mahmoud, *Journal of hazardous materials*, 2008, **154**, 245-253.
259. L. F. a. de Oliveira, K. Bouchmella, K. d. A. Gonçalves, J. Bettini, J. r. Kobarg and M. B. Cardoso, *Langmuir*, 2016, **32**, 3217-3225.
260. X. Li, S. Yang, J. Sun, P. He, X. Xu and G. Ding, *Carbon*, 2014, **78**, 38-48.
261. G. Jiang, Z. Lin, C. Chen, L. Zhu, Q. Chang, N. Wang, W. Wei and H. Tang, *Carbon*, 2011, **49**, 2693-2701.
262. A. Arshad, J. Iqbal, M. Siddiq, Q. Mansoor, M. Ismail, F. Mehmood, M. Ajmal and Z. Abid, *Journal of Applied Physics*, 2017, **121**, 024901.
263. X. Liang, S. Liu, X. Song, Y. Zhu and S. Jiang, *Analyst*, 2012, **137**, 5237-5244.
264. S. Tajik, B. Nasernejad and A. Rashidi, *Journal of Molecular Liquids*, 2016, **222**, 788-795.
265. Z.-M. Wang, W. Wang, N. Coombs, N. Soheilnia and G. A. Ozin, *Acs Nano*, 2010, **4**, 7437-7450.
266. S. Watcharotone, D. A. Dikin, S. Stankovich, R. Piner, I. Jung, G. H. Dommett, G. Evmenenko, S.-E. Wu, S.-F. Chen and C.-P. Liu, *Nano letters*, 2007, **7**, 1888-1892.
267. L. Kou and C. Gao, *Nanoscale*, 2011, **3**, 519-528.
268. D. Yin, B. Liu, L. Zhang and M. Wu, *Journal of biomedical nanotechnology*, 2012, **8**, 458-464.
269. N. D. Singho and M. R. Johan, *Int. J. Electrochem. Sci*, 2012, **7**, 5604-5615.
270. T. Tsukamoto, K. Yamazaki, H. Komurasaki and T. Ogino, *The Journal of Physical Chemistry C*, 2012, **116**, 4732-4737.

271. M. Jafarzadeh, I. Rahman and C. Sipaut, *Ceramics International*, 2010, **36**, 333-338.
272. I. Rahman, P. Vejayakumaran, C. Sipaut, J. Ismail and C. Chee, *Materials Chemistry and Physics*, 2009, **114**, 328-332.
273. K. V. Kumar, K. Porkodi and F. Rocha, *Catalysis Communications*, 2008, **9**, 82-84.
274. W. Hu, C. Peng, W. Luo, M. Lv, X. Li, D. Li, Q. Huang and C. Fan, *Acs Nano*, 2010, **4**, 4317-4323.
275. E. Nakamura and H. Isobe, *Accounts of chemical research*, 2003, **36**, 807-815.
276. L. Lacerda, A. Bianco, M. Prato and K. Kostarelos, *Advanced drug delivery reviews*, 2006, **58**, 1460-1470.
277. Z. Liu, S. Tabakman, K. Welsher and H. Dai, *Nano Research*, 2009, **2**, 85-120.
278. H. W. Harris, M. Y. El-Naggar, O. Bretschger, M. J. Ward, M. F. Romine, A. Obraztsova and K. H. Nealson, *Proceedings of the National Academy of Sciences*, 2010, **107**, 326-331.
279. Y. Zhao, L. P. Wang, M. T. Sougrati, Z. Feng, Y. Leconte, A. Fisher, M. Srinivasan and Z. Xu, *Advanced Energy Materials*, 2016.
280. H. Huang, Z. Yue, G. Li, X. Wang, J. Huang, Y. Du and P. Yang, *Journal of Materials Chemistry A*, 2013, **1**, 15110-15116.
281. A. Arshad, J. Iqbal, Q. Mansoor and I. Ahmed, *Journal of Applied Physics*, 2017, **121**, 244901.
282. A. Arshad, J. Iqbal, M. Siddiq, M. U. Ali, A. Ali, H. Shabbir, U. B. Nazeer and M. S. Saleem, *Ceramics International*, 2017.
283. X. Zhou, H. Yang, C. Wang, X. Mao, Y. Wang, Y. Yang and G. Liu, *The Journal of Physical Chemistry C*, 2010, **114**, 17051-17061.
284. M. Pereira, L. Oliveira and E. Murad, *Clay Minerals*, 2012, **47**, 285-302.
285. G. Liu, N. Wang, J. Zhou, A. Wang, J. Wang, R. Jin and H. Lv, *RSC Advances*, 2015, **5**, 95857-95865.
286. H. Sun, L. Cao and L. Lu, *Nano Research*, 2011, **4**, 550-562.
287. C. Wang, C. Feng, Y. Gao, X. Ma, Q. Wu and Z. Wang, *Chemical Engineering Journal*, 2011, **173**, 92-97.
288. Y. Yao, S. Miao, S. Liu, L. P. Ma, H. Sun and S. Wang, *Chemical Engineering Journal*, 2012, **184**, 326-332.
289. Z. Hua, W. Ma, X. Bai, R. Feng, L. Yu, X. Zhang and Z. Dai, *Environmental Science and Pollution Research*, 2014, **21**, 7737-7745.
290. X. Yang, W. Chen, J. Huang, Y. Zhou, Y. Zhu and C. Li, *Scientific reports*, 2015, **5**.
291. Y. Yin, M. Zeng, J. Liu, W. Tang, H. Dong, R. Xia and R. Yu, *Scientific reports*, 2016, **6**.
292. W. Zhang, C. Wang, Z. Li, Z. Lu, Y. Li, J.-J. Yin, Y.-T. Zhou, X. Gao, Y. Fang, G. Nie and Y. Zhao, *Advanced Materials*, 2012, **24**, 5391-5397.
293. R. Comparelli, E. Fanizza, M. L. Curri, P. D. Cozzoli, G. Mascolo, R. Passino and A. Agostiano, *Applied Catalysis B: Environmental*, 2005, **55**, 81-91.
294. R. Comparelli, E. Fanizza, M. L. Curri, P. D. Cozzoli, G. Mascolo and A. Agostiano, *Applied Catalysis B: Environmental*, 2005, **60**, 1-11.
295. H.-Y. Xu, T.-N. Shi, H. Zhao, L.-G. Jin, F.-C. Wang, C.-Y. Wang and S.-Y. Qi, *Frontiers of Materials Science*, 2016, **10**, 45-55.
296. J.-H. Deng, X.-R. Zhang, G.-M. Zeng, J.-L. Gong, Q.-Y. Niu and J. Liang, *Chemical Engineering Journal*, 2013, **226**, 189-200.
297. K. Prasad, G. Lekshmi, K. Ostrikov, V. Lussini, J. Blinco, M. Mohandas, K. Vasilev, S. Bottle, K. Bazaka and K. Ostrikov, *Scientific Reports*, 2017, **7**.

298. F. Perreault, A. Fonseca de Faria and M. Elimelech, *Chemical Society Reviews*, 2015, **44**, 5861-5896.
299. T. J. Silhavy, D. Kahne and S. Walker, *Cold Spring Harbor perspectives in biology*, 2010, **2**, a000414.
300. S. H. S. Chan, T. Yeong Wu, J. C. Juan and C. Y. Teh, *Journal of Chemical Technology and Biotechnology*, 2011, **86**, 1130-1158.
301. B. Varghese, M. Reddy, Z. Yanwu, C. S. Lit, T. C. Hoong, G. Subba Rao, B. Chowdari, A. T. S. Wee, C. T. Lim and C.-H. Sow, *Chemistry of Materials*, 2008, **20**, 3360-3367.
302. S. Ni, X. Lv, J. Ma, X. Yang and L. Zhang, *Journal of Power Sources*, 2014, **270**, 564-568.
303. S. Ni, T. Li, X. Lv, X. Yang and L. Zhang, *Electrochimica Acta*, 2013, **91**, 267-274.
304. M. Gong, W. Zhou, M.-C. Tsai, J. Zhou, M. Guan, M.-C. Lin, B. Zhang, Y. Hu, D.-Y. Wang and J. Yang, *Nature communications*, 2014, **5**.
305. M. Shen, A. Han, X. Wang, Y. G. Ro, A. Kargar, Y. Lin, H. Guo, P. Du, J. Jiang and J. Zhang, *Scientific reports*, 2015, **5**.
306. J. Xiao, B. Chen, X. Liang, R. Zhang and Y. Li, *Catalysis Science & Technology*, 2011, **1**, 999-1005.
307. B. Zhao, X.-K. Ke, J.-H. Bao, C.-L. Wang, L. Dong, Y.-W. Chen and H.-L. Chen, *The Journal of Physical Chemistry C*, 2009, **113**, 14440-14447.
308. I. Abdul Rahman, M. Ayob and S. Radiman, *Journal of Nanotechnology*, 2014, **2014**.
309. N. Ajoudanian and A. Nezamzadeh-Ejhieh, *Materials Science in Semiconductor Processing*, 2015, **36**, 162-169.
310. X. Wan, M. Yuan, S.-l. Tie and S. Lan, *Applied Surface Science*, 2013, **277**, 40-46.
311. F. Zhang, Y. Liu, Q. Liu, Q. Li, H. Li, X. Cai and Y. Wang, *Materials Technology*, 2013, **28**, 310-315.
312. A. Naskar, S. Bera, R. Bhattacharya, P. Saha, S. S. Roy, T. Sen and S. Jana, *RSC Advances*, 2016, **6**, 88751-88761.
313. E. Rokhsat and O. Akhavan, *Applied Surface Science*, 2016, **371**, 590-595.
314. L.-L. Tan, W.-J. Ong, S.-P. Chai and A. R. Mohamed, *Chemical Engineering Journal*, 2017, **308**, 248-255.
315. Y.-C. Pu, H.-Y. Chou, W.-S. Kuo, K.-H. Wei and Y.-J. Hsu, *Applied Catalysis B: Environmental*, 2017, **204**, 21-32.
316. Y. Liu, W. Li, J. Li, Y. Yang and Q. Chen, *RSC Advances*, 2014, **4**, 3219-3225.
317. X. Li, J. Yu, S. Wageh, A. A. Al-Ghamdi and J. Xie, *Small*, 2016.
318. M. A. Buccheri, D. D’Angelo, S. Scalese, S. F. Spanò, S. Filice, E. Fazio, G. Compagnini, M. Zimbone, M. V. Brundo and R. Pecoraro, *Nanotechnology*, 2016, **27**, 245704.
319. K.-T. Chung, S. E. Stevens and C. E. Cerniglia, *Critical reviews in microbiology*, 1992, **18**, 175-190.
320. K.-T. Chung, *Mutation Research/Reviews in Genetic Toxicology*, 1983, **114**, 269-281.
321. W. Li, Y. Bu, H. Jin, J. Wang, W. Zhang, S. Wang and J. Wang, *Energy & Fuels*, 2013, **27**, 6304-6310.
322. Z. Zhou, H. Ni and L.-Z. Fan, *Journal of Nanoscience and Nanotechnology*, 2014, **14**, 4976-4981.
323. Y.-G. Zhu, G.-S. Cao, C.-Y. Sun, J. Xie, S.-Y. Liu, T.-J. Zhu, X. Zhao and H. Y. Yang, *RSC Advances*, 2013, **3**, 19409-19415.
324. W. Chen, D. Gui and J. Liu, *Electrochimica Acta*, 2016, **222**, 1424-1429.

325. Y. Zou and Y. Wang, *Nanoscale*, 2011, **3**, 2615-2620.
326. A. V. Titov, P. Král and R. Pearson, *Acs Nano*, 2009, **4**, 229-234.
327. J. Han, B. K. Woo, W. Chen, M. Sang, X. Lu and W. Zhang, *The Journal of Physical Chemistry C*, 2008, **112**, 17512-17516.
328. C.-W. Lee, K. C. Roh and K.-B. Kim, *Nanoscale*, 2013, **5**, 9604-9608.
329. P. Cheng, Z. Yang, H. Wang, W. Cheng, M. Chen, W. Shangguan and G. Ding, *International Journal of Hydrogen Energy*, 2012, **37**, 2224-2230.